Direct numerical simulation of laminar-turbulent transition in boundary layer subject to free-stream turbulence

Diploma Thesis
Winter Term 2000 / 2001

Philipp Schlatter

Department of Mechanics
KTH Stockholm

written with MiKTEX1.20, a LaTeX implementation on Windows PC.

Abstract

A Direct Numerical Simulation (DNS) of a flat plate boundary layer subject to freestream turbulence was performed. The freestream turbulence was modeled by a superposition of a number of eigenmodes of the Orr-Sommerfeld and Squire equation to meet a certain inlet energy spectrum. Together with an efficient spectral solver for the incompressible Navier-Stokes equations, a robust algorithm to perform simulations of transitional boundary layers was devised.

For the main computation, a freestream turbulence intensity of 4.7% was studied. The development of laminar streaks within the boundary layer could be observed. The breakdown of the streaks to form turbulent spots and eventually fully developed turbulence was also clearly captured by the simulation.

The averaged results of the simulation, like the skin friction coefficient or the evolution of the kinetic energy within the boundary layer, show good qualitative and quantitative agreement to both experimental and numerical studies.

A clear sign of a regularly oscillating secondary instability of the laminar streaks prior to their breakdown could be observed, although no conclusive classification of these instabilities can be given at the present time.

Contents

Figures

Tables

Symbols

The symbols are presented in the order of their appearance in the text. Not mentioned are symbols that are only used once in a certain context.

Greek symbols:

α	streamwise wavenumber
β	spanwise wavenumber
γ	normal wavenumber
ω	temporal frequency
θ	momentum thickness
$\delta_{99\%}$	99% boundary layer thickness
δ^*	displacement thickness
ν	kinematic viscosity
ρ	density
δ_{ij}	Kronecker (delta) symbol
κ	wave vector
ϕ	spectral tensor
Ω	surface element
Φ, ψ, k^*	scaling factor for eigenmodes
ϵ_{ijk}	permutation symbol
ω	vorticity vector
λ	fringe function
$\lambda_{\max}$	maximal fringe function
ε	turbulent dissipation
ψ	stream function
η	Blasius similarity variable
τ_w	local shear force
Δ_{rise}	rise distance in fringe function
Δ_{fall}	fall distance in fringe function

Roman symbols:

u, v, w	streamwise, normal, spanwise fluid velocity components
u_1, u_2, u_3	streamwise, normal, spanwise fluid velocity components
u_x, u_y, u_z	streamwise, normal, spanwise fluid velocity components
t	time
p	pressure
x, y, z	streamwise, normal, spanwise spatial coordinates
U, U_∞	base flow
Re	Reynolds number
Re_x	Reynolds number based on downstream location
Re_θ	Reynolds number based on momentum thickness
Re_{δ^*}	Reynolds number based on displacement thickness
η	normal vorticity ($\eta = \frac{\partial u}{\partial z} - \frac{\partial w}{\partial x}$)
Tu	turbulence intensity
i	complex unit $i = \sqrt{-1}$
k	turbulent kinetic energy
R_{ij}, R_{ij}^r	spatial two-point correlation
$E(\kappa)$	energy spectrum
u_I	integral velocity scale
L_I	integral length scale
L_{11}	integral length scale from two-point correlation
x_0	distance from the leading edge
F_i	body force
$\mathcal{U}$	base flow in the simulation
$\mathcal{U}^{\mathrm{act}}$	base flow in the simulation with imposed freestream turbulence
u_i^{dist}	freestream turbulence formed by continuous modes
x_L, y_L, z_L	dimensions of the computational domain
CFL	Courant-Friedrichs-Lewy number
$S(x)$	smooth step function
y_{blend}	start of blending in y
x_{start}, x_{end}	fringe extent
E	energy
N_x, N_y, N_z	number of grid points
c_f	friction coefficient
H	shape factor
$f(\eta)$	Blasius boundary layer similarity solution
u_τ	friction velocity

Superscripts and subscripts:

$(\cdot)'$	derivation with respect to the normal direction
$\widetilde{(\cdot)}$	dimensional quantity
$(\cdot)_{\mathrm{ref}}$	reference quantity
$\underset{\sim}{(\cdot)}$	wave amplitude
$(\cdot)_{\mathrm{OS}}$	Orr-Sommerfeld mode
$(\cdot)_{\mathrm{SQ}}$	Squire mode
$\overline{(\cdot)}$	averaged quantity
$\underline{(\cdot)}$	vector quantity
$\overline{(\cdot)}'$	fluctuating quantity
$(\cdot)_{\mathrm{rms}}$	rms value
$(\cdot)^+$	wall scaling

Special symbols:

∇	Nabla operator
$\mathcal{O}$	Landau symbol (order of)
$\mathcal{D}$	differential operator with respect to the normal direction
$\Re(\cdot)$	real part of a complex number
$\Im(\cdot)$	imaginary part of a complex number

Chapter 1

Introduction

The behavior and properties of flowing fluids in different technical applications is an important issue of the industrial world today. The most important characteristic of a flowing fluid is the flow state in which it is moving; laminar, turbulent or the transitional state in between. A laminar flow is a well structured, layered flow (latin *lamina*: layer, sheet, leaf), which exercises a less frictional resistance to a solid wall in comparison to the chaotic fluid state of a turbulent flow. Thereby, laminar flow is an important factor in aircraft design due to the fact that the reduction of the skin friction is one of the major challenges in this area. The turbulent flow has on the other hand a very good mixing ability due to the stochastic movements of the fluid elements, which laminar flow cannot provide. Therefore, turbulent flow is for instance required in chemical reactors and combustion chambers, where the mixing of the flow is the main issue of the design.

1.1 Transition

The evolution of an initially laminar flow into a fully developed turbulent flow is called laminar-turbulent transition or simply transition. This process and especially the triggering mechanisms of transition are even today not fully understood. The history of transition research begins with the classical experiments made by Reynolds at the turn of the 19^{th} century. He discovered that for the flow in a tube the shift from laminar to turbulent flow is basically dependent upon the non-dimensional Reynolds number $\mathrm{Re} = \frac{Ur}{\nu}$, but it is also sensitive to disturbances in the fluid before entering the tube. Here, U denotes the fluid velocity, r the tube radius and ν the kinematic viscosity.

Today, the transitional process is commonly divided into three stages: receptivity phase, disturbance growth and turbulent breakdown.

The receptivity phase describes the different ways, how disturbances can originate in a given flow. In the case of boundary layers, physical factors as freestream turbulence or surface roughness can generate small perturbations in the boundary layer which could eventually lead to a turbulent breakdown. The occurrence and the form of these disturbances are statistical. The prediction of boundary layer receptivity is still a topic of research.

1.1.1 Disturbance Growth

As soon as disturbances are present in the flow, they can either grow or decay. If they are growing enough, they can finally reach a such high level, that the initially laminar flow breaks down into turbulence.

In the case, where the disturbances are originated by freestream turbulence, two different scenario can be distinguished. If the outer disturbance level is relatively small, the transition process can be considered as governed by the classical linear stability theory. That means that the basic flow equations (Navier-Stokes equations) can be linearized around the mean velocity yielding the important Orr-Sommerfeld stability equations (for further explanation refer to chapter 2)

$$\left[\left(\frac{\partial}{\partial t}+U\frac{\partial}{\partial x}\right)\nabla^2-u''\frac{\partial}{\partial x}-\frac{1}{\mathrm{Re}}\nabla^4\right]v=0. \tag{1.1}$$

These equations describe the evolution of (two-dimensional) disturbances in time and space. From the individual form of the least-stable (least-damped) solution to the Orr-Sommerfeld equation it can be decided whether the flow is stable or instable in the sense of linear stability. Exponentially growing solutions of (1.1) are named Tollmien-Schlichting (TS) waves in honor of their discoverers, although their theoretical prediction of the TS waves in 1929 was not experimentally verified until twenty years later. Transition due to the exponential growth of TS waves is commonly referred to as natural transition.

If on the other hand the outer disturbance level is rather high ($\mathrm{Tu}\gtrsim 1\%$), transition is caused by a different process than the exponential growth of TS waves. In contrast to the natural transition governed by the linear stability theory, the so called transient growth of disturbances can lead to turbulence at much lower Reynolds numbers. Therefore, it is sometimes called bypass transition to express the fact, that natural transition via TS waves is bypassed. Basically, rather than an exponential growth as in natural transition an algebraic (linear) growth mechanism is acting on the streamwise velocity component.

To understand the mathematical concept behind the bypass transition process (see also section 5.4.1), it is important to consider the three-dimensionality of the initial disturbances. Therefore, an equation similar to the Orr-Sommerfeld equation can be derived for the normal vorticity $\eta=\frac{\partial u}{\partial z}-\frac{\partial w}{\partial x}$

$$\left[\frac{\partial}{\partial t}+U\frac{\partial}{\partial x}-\frac{1}{\mathrm{Re}}\nabla^2\right]\eta=-U'\frac{\partial v}{\partial z}, \tag{1.2}$$

which is called the Squire equation. The forcing term $-U'\frac{\partial v}{\partial z}$ in the Squire equation can be considered as vortex tilting [28], i.e. the spanwise vorticity associated with the mean shear layer is tilted in the wall-normal direction under the influence of streamwise vorticity from disturbances present in the boundary layer. Together with the theory of shear sheltering [16], whereupon low-frequency disturbances of the freestream turbulence can penetrate the boundary layer, a theory of generating normal vorticity within the boundary layer can be derived. This effect is normally referred to as *lift-up* effect.

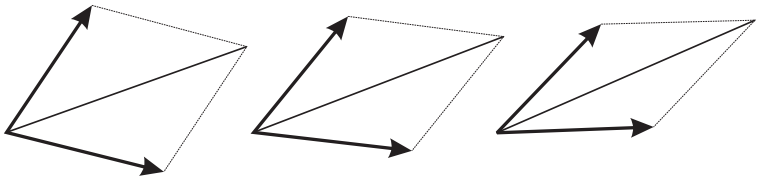

FIGURE 1.1: Simple illustration of transient growth using two non-orthogonal vectors: Although both vectors decrease from left to right, their common sum is growing.

A physical explanation of the transient growth process was first described by Landahl 1975 [17]. The basic idea is, that a wall normal displacement of a fluid element in a shear layer will cause a perturbation in the streamwise velocity component, since the fluid element will initially retain its horizontal momentum. The lift-up mechanism in three-dimensional flows will lead to algebraic growth of the normal vorticity η generating streaky structures which are elongated in the streamwise direction; so called streaks [21]. In this context, the freestream turbulence is important both in the initial formation of the streaks as well as during later growth phases since a constant forcing of the streaks is exercised [7]. As pointed out in [16] and [28], these laminar streaks play an important role in the bypass transition process.

It is important to note that streaks are still a phenomena of laminar flow; the skin friction coefficient c_f for example is only increased by a few percent compared to the Blasius flow. Moreover, the above presented mechanism is basically inviscid. The same mechanism will also be important with viscosity acting, although viscous effects will eventually damp the disturbances, if they are not forced in any way. Consequently, the disturbances can exhibit a transient growth, before viscous damping makes the unforced disturbances decay. The maximum growth rate of so-called optimal disturbances is derived in [3], showing that the spanwise width of such disturbances falls in a tight range. However, in the case of a boundary layer subject to freestream turbulence, it was proposed that the disturbances within the boundary layer are continuously forced by the outer turbulence [6], [7]. Therefore, a direct comparison of the disturbances to the optimal disturbances proves to be difficult. Even so, the spanwise wavelength derived for the optimal disturbances can be considered an estimate of the average spacing of laminar streaks [15]. Recent investigations of the nonlinear effects involved in the streak formation can be found in [7] and [6].

Mathematically, the solutions to the coupled system (1.1) and (1.2) consist of non-orthogonal eigenfunction [14]. As earlier noted, traditional stability analysis only considers the least stable mode, from which it is determined whether a flow is stable or not. However, even if all eigenmodes are stable and the amplitude of each individual mode is decreasing, the sum of them can transiently exhibit energy growth due to the non-orthogonality of the eigenmodes [21] (see figure 1.1). Therefore, the energy of general disturbances (e.g. freestream turbulence) considered as a sum of eigenfunctions can increase linearly in time/space although all modes individually are stable.

1.1.2 Streak Breakdown

The streaks can reach a considerable strength of up to fifteen percent of the freestream velocity without breaking down to turbulence [1]. In contrast, natural transition due to exponential growth of TS waves occurs with amplitudes nearly an order of magnitude smaller. The breakdown of laminar streaks according to [16] is largely due to interactions of low-speed streaks in the upper part of the boundary layer with large-scale eddies in the freestream. The question of whether or not the streaks undergo a distinct secondary instability before their breakdown is not yet clarified. Although theories of secondary instabilities exist (for example [4]) and experimental observations seem to prove their presence ([19], [1]), the numerical calculation of [16] did not show any distinct secondary instability.

With or without distinct secondary instability, a streak breakdown forms localized turbulent spots moving downstream with about half the freestream velocity. The spots merge with other spots to form a fully developed turbulent boundary layer. As mentioned earlier, the breakdown into turbulence in the bypass transition scenario occurs at much lower Reynolds numbers ($\mathrm{Re}_\theta = \mathcal{O}(100)$ based on the local momentum thickness θ) than in natural transition ($\mathrm{Re}_\theta = 5000$). It has to be mentioned, that – up to now – no complete theory of turbulent breakdown of laminar streaks exists, e.g. the transitional location cannot be generally predicted, although some experiments e.g. [28], [1] show good agreement to the proposal given by [2] that the transitional Reynolds number $\mathrm{Re}_{x,tr}$ scales with the squared inverse turbulence intensity Tu^{-2}.

1.2 Experiments and Numerical Simulations

Extensive experimental data of transient growth of disturbances in boundary layers is given in [28]. In this report, relatively low turbulence intensities of Tu = 1.5% were examined giving important results considering the scales of streaks and breakdown locations. Moreover, a proper specification of the inflow spectrum has been described.

Larger turbulence intensities of 3% resp. 6% in the freestream for boundary layer transition have been studied experimentally in the ERCOFTAC test cases T3A and T3B [10]. Comparisons to these cases will be made throughout this report. Numerical data is available from ERCOFTAC [20] directly referring to the test cases T3A and T3B (see also section 5.1.1).

A recent experimental description of boundary layer flow subjected to free-stream turbulence in the range from 1-6% is presented in [19] and [1] together with a characterization of the freestream turbulence in terms of spectra. Furthermore, qualifications of the streak growth and their spanwise scales are given.

An extensive numerical study of transition in boundary layers subjected to free-stream turbulence is given in [16] and [15]. In that report, the freestream turbulence is assumed as a superposition of continuous modes to the Orr-Sommerfeld equation (see chapter 2). Good agreement of the simulations to the test cases T3A and T3B [10] as well as to [28] is shown.

1.3 Aims and Overview

The aim of the present thesis is to perform a numerical simulation of transition in a boundary layer subject to free-stream turbulence. As pointed out earlier, the understanding and prediction of transition is even today not yet understood and relies mainly on experimental data or numerical simulations. The postprocessing of such data allows a deeper insight into the vast field of transition and transition scenarios and – eventually – to find theoretical ways to predict the behaviour of a flow.

This report consists of six chapters. In chapter 2 the basic mathematical and physical formulations are developed and the modeling of the freestream turbulence is derived. Chapter 3 gives details about the numerical code used in the simulations and the implementation of the freestream turbulence is described. The validation of the numerical code with the superimposed Orr-Sommerfeld / Squire eigenmodes is shown in chapter 4. Chapter 5 presents the results, which were found during this study together with theoretical indications. Concluding remarks are given in chapter 6. The appendix shortly describes the derivation of the boundary layer equations and the Blasius solution.

Chapter 2

Theoretical Formulation

The governing equations for general incompressible flow problems are the equation of continuity and the Navier-Stokes equations. In nondimensional form they read

$$u_{i,i} = 0 \tag{2.1}$$

$$\frac{\partial u_i}{\partial t} + u_j u_{i,j} = -p_{,i} + \frac{1}{\mathrm{Re}} u_{i,jj} \tag{2.2}$$

where u_i represents the i-th component of the velocity vector, p the pressure, t the time and Re the Reynolds number. For indices, the Einstein summation convention applies and an index after a comma means differentiation with respect to that direction. Throughout this text, the subscripts 1, 2 and 3 correspond to the streamwise (x), wall-normal (y) and spanwise (z) directions, respectively. By common convention, the velocities in the respective directions will also be denoted by $u = u_x$, $v = u_y$ and $w = u_z$.

Dimensional and non-dimensional variables are related by

$$\begin{aligned} \tilde{u}_i &= \tilde{U}_{\mathrm{ref}} \cdot u_i \\ \tilde{x}_i &= \tilde{L}_{\mathrm{ref}} \cdot x_i \\ \tilde{p} &= \tilde{\rho} \tilde{U}_{\mathrm{ref}}^2 \cdot p \\ \tilde{t} &= \frac{\tilde{L}_{\mathrm{ref}}}{\tilde{U}_{\mathrm{ref}}} \cdot t, \end{aligned}$$

where the tilde $\tilde{(\cdot)}$ denotes a dimensional quantity. $\tilde{U}_{\mathrm{ref}}$, $\tilde{L}_{\mathrm{ref}}$, $\tilde{\rho}$ and $\tilde{\nu}$ represent a characteristic velocity, length, density and kinematic viscosity, respectively.

The definition of the Reynolds-Number is given by

$$\mathrm{Re} = \frac{\tilde{U}_{\mathrm{ref}} \tilde{L}_{\mathrm{ref}}}{\tilde{\nu}}. \tag{2.3}$$

In general, the Reynolds number describes the ratio between the inertial and viscous forces in a flow. Therefore, it is an important measure of the characteristics of a flow.

2.1 Orr-Sommerfeld / Squire Equation

In all real flows, known and unknown disturbances are present. These disturbances can grow and finally lead to the breakdown of the initially laminar flow. The growth (or alternatively decay) of small disturbances in a viscous boundary layer flow can be described using the linear stability theory. The Orr-Sommerfeld / Squire equations, which will be derived in this chapter, are a means to specify the downstream evolution of instabilities in a flow.

Together with an appropriate set of boundary and initial conditions, the Navier-Stokes equations (2.2) and the equation of continuity (2.1) form an elliptic/parabolic system to describe an incompressible flow. In order to derive evolution equations for small perturbations, consider a basic state (U_i, P) satisfying the Navier-Stokes equations. With this basic state, perturbations can be seen as the difference between the local quantities and the basic flow $(u_i - U_i, p - P) = (u_i', p')$. Applying this difference to the above equations and omitting the primes yields the nonlinear evolution equations

$$u_{i,i} = 0 \tag{2.4}$$

$$\frac{\partial u_i}{\partial t} + U_j u_{i,j} + u_j U_{i,j} + u_j u_{i,j} = -p_{,i} + \frac{1}{\mathrm{Re}} u_{i,jj}. \tag{2.5}$$

The boundary conditions to this set of equations have also to be written with respect to the disturbance formulation.

Consider a parallel flow in x-direction only dependent on the wall normal coordinate y as basic state

$$U_i = U_i(y)\delta_{1i}$$

with δ_{ij} as Kronecker symbol

$$\delta_{ij} = \begin{cases} 1 & i = j \\ 0 & i \neq j \end{cases} \tag{2.6}$$

Inserting this base flow into the evolution equations (2.5) and neglecting all nonlinear terms gives

$$\frac{\partial u_i}{\partial t} + U\frac{\partial u_i}{\partial x} + \delta_{1i} u_2 U' = -p_{,i} + \frac{1}{\mathrm{Re}} u_{i,jj} \tag{2.7}$$

together with continuity (2.4). Here, the prime denotes differentiation with respect to the wall normal direction $(\cdot)' = \frac{d(\cdot)}{dy}$.

These equations can be rewritten using a variable substitution for the normal velocity $v = u_2$ and for the normal vorticity $\eta = \frac{\partial u}{\partial z} - \frac{\partial w}{\partial x}$ yielding the velocity-vorticity formulation [14]

$$\left[\left(\frac{\partial}{\partial t} + U\frac{\partial}{\partial x}\right)\nabla^2 - u''\frac{\partial}{\partial x} - \frac{1}{\mathrm{Re}}\nabla^4\right] v = 0 \tag{2.8}$$

$$\left[\frac{\partial}{\partial t} + U\frac{\partial}{\partial x} - \frac{1}{\mathrm{Re}}\nabla^2\right]\eta = -U'\frac{\partial v}{\partial z}. \tag{2.9}$$

Again, boundary and initial conditions for v and η have to be supplied, e.g. for solid walls and the undisturbed far field, the boundary conditions read

$$v = v' = \eta = 0. \tag{2.10}$$

Following the notation of [14], the introduction of wavelike solutions of the form

$$v(x,y,z,t) = \tilde{v}(y)e^{i(\alpha x+\beta z-\omega t)} \tag{2.11}$$
$$\eta(x,y,z,t) = \tilde{\eta}(y)e^{i(\alpha x+\beta z-\omega t)} \tag{2.12}$$

finally results in a pair of equations for $\tilde{v}$ and $\tilde{\eta}$

$$\left[(-i\omega + i\alpha U)(\mathcal{D}^2-\kappa^2) - i\alpha U'' - \frac{1}{\mathrm{Re}}(\mathcal{D}^2-\kappa^2)^2\right]\tilde{v} = 0 \tag{2.13}$$
$$\left[(-i\omega + i\alpha U) - \frac{1}{\mathrm{Re}}(\mathcal{D}^2-\kappa^2)\right]\tilde{\eta} = -i\beta U'\tilde{v}. \tag{2.14}$$

Herein α and β represent the streamwise and spanwise wavenumber, $\kappa = \sqrt{\alpha^2+\beta^2}$ and ω denotes the (temporal) frequency, $\mathcal{D}$ stands for differentiation with respect to the normal direction. Consequently, the boundary conditions at solid walls and in the undisturbed free stream read

$$\tilde{v} = \mathcal{D}\tilde{v} = \tilde{\eta} = 0. \tag{2.15}$$

In order to invert the substitution of the velocity components u and w (respectively $\tilde{u}$ and $\tilde{w}$), they can be computed using the equation of continuity and the definition of $\tilde{\eta}$,

$$\tilde{u}i\alpha + \frac{\partial\tilde{v}}{\partial y} + \tilde{w}i\beta = 0 \tag{2.16}$$
$$\tilde{\eta} = \tilde{u}i\beta - \tilde{w}i\alpha, \tag{2.17}$$

yielding an expression for $\tilde{u}$ and $\tilde{w}$

$$\tilde{u} = \frac{i}{\kappa^2}(\alpha\mathcal{D}\tilde{v} - \beta\tilde{\eta}) \tag{2.18}$$
$$\tilde{w} = \frac{i}{\kappa^2}(\beta\mathcal{D}\tilde{v} + \alpha\tilde{\eta}). \tag{2.19}$$

Equation (2.13) for the normal velocity $\tilde{v}$ is called the Orr-Sommerfeld equation, whereas equation (2.14) for the normal vorticity $\tilde{\eta}$ is referred to as Squire equation.

The Orr-Sommerfeld and the Squire equation are coupled through the source term $-i\beta U'\tilde{v}$. They form together a complete eigenvalue problem for three-dimensional disturbances. In the general case (coupling term nonzero, $\beta \neq 0$), the solution consists of fluctuations in all three velocity components

$$\text{Full mode } (\beta \neq 0): \qquad \tilde{u}_{\mathrm{OS/SQ}}, \tilde{v}_{\mathrm{OS/SQ}}, \tilde{w}_{\mathrm{OS/SQ}}. \tag{2.20}$$

In the case of $\beta = 0$, the two equations lose their coupling term and can therefore be solved independently. The Orr-Sommerfeld equation for this case will lead to two-dimensional disturbances in $\tilde{u}$ and $\tilde{v}$, whereas the Squire equation will govern the behaviour of $\tilde{\eta}$ and $\tilde{w}$.

$$\begin{aligned} &\text{Full mode } (\beta = 0) \text{ – OS equation:} && \tilde{u}_{\mathrm{OS}}, \tilde{v}_{\mathrm{OS}}, 0 \\ &\text{Full mode } (\beta = 0) \text{ – SQ equation:} && 0, 0, \tilde{w}_{\mathrm{SQ}}. \end{aligned} \tag{2.21}$$

Neglecting the coupling term $-i\beta U'\tilde{v}$ in the general case ($\beta \neq 0$) – which means not considering the solution of the Orr-Sommerfeld equation for $\tilde{v}$ while solving the Squire equation – will lead to two sets of eigenfunctions; one for $\tilde{v}$ (from Orr-Sommerfeld equation) and one for $\tilde{\eta}$ (from Squire equation). Expanding these two different solutions individually using continuity (2.16) to all velocity components yields two different disturbances – Orr-Sommerfeld modes (pure OS modes) only considering the Orr-Sommerfeld equation and Squire modes (pure SQ modes) only using the Squire equation

$$\text{OS-mode:} \qquad \tilde{u}_{\mathrm{OS}}, \tilde{v}_{\mathrm{OS}}, \tilde{w}_{\mathrm{OS}} \tag{2.22}$$

$$\text{SQ-mode:} \qquad \tilde{u}_{\mathrm{SQ}}, 0, \tilde{w}_{\mathrm{SQ}}. \tag{2.23}$$

2.1.1 Eigenvalue Spectrum

The solution to the eigenvalue problem of the Orr-Sommerfeld / Squire equation can either be considered as temporal problem, where disturbances grow (or decay) in time. This view implies a real streamwise wave number α, but a complex wave velocity $c = \omega/\alpha$. On the other hand, a spatial eigenvalue problem is given by choosing a real frequency ω and a complex wave number α. A spatial viewpoint implies a growth (or decay) of the disturbances in space rather than in time – exponentially growing modes are thus given by $\Im(\alpha) < 0$. In this report, we solely concentrate on the spatial approach to the linear stability equations.

The Orr-Sommerfeld / Squire equations (2.13) and (2.14) pose a eigenproblem for – in the spatial approach – the complex streamwise wavenumber α (the eigenvalue) and the disturbances $\tilde{v}(y)$ and $\tilde{\eta}(y)$ (the eigenfunctions) with given parameters Re (Reynolds number), β (spanwise wavenumber) and ω (temporal frequency).

The eigensolutions to these equations in a semi-infinite domain are divided into two spectra: A set of discrete modes and an infinite continuum of modes. Figure 2.1 shows a typical distribution of eigenvalues for the Blasius boundary layer. The form of eigenfunctions of the discrete and the continuous spectrum are quite different: Modes of the discrete spectrum decay exponentially outside the boundary layer from an intensity maximum near to the wall, while the continuous modes seem to be inable to penetrate the boundary layer. This effect has been described as *shear-sheltering* [16]. Outside the boundary layer, continuous modes oscillate sinusoidally.

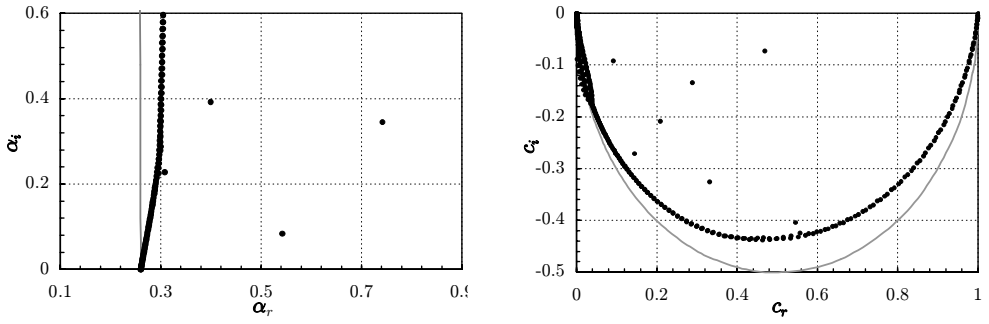

FIGURE 2.1: Typical spatial spectrum for Blasius boundary layer flow with $\omega = 0.26$, $\beta = 0$, Re=1000 (Parameters similar to figure in [14]). Dots computed with eigensolver (chapter 2.1.2), gray line computed with freestream approximation (chapter 2.1.3). *left:* Eigenvalues in complex α-plane. *right:* Eigenvalues in complex $c = \omega/\alpha$-plane.

Discrete Spectrum

Eigensolutions of the discrete spectrum are basically confined to the boundary layer and are much larger near the wall than further out in the freestream. Outside the boundary layer, they tend to decay exponentially. Therefore, the boundary conditions at the wall and in the freestream ($y \to \infty$) can be written as

$$\tilde{v} = \mathcal{D}\tilde{v} = \tilde{\eta} = 0. \tag{2.24}$$

For these boundary conditions, a (finite) set of eigenvalues and eigenfunctions to the equations (2.13) and (2.14) can be found. A suitable algorithm to compute the eigenfunctions of the discrete spectrum would, for example, be the companion matrix method [15] or standard eigensolver routines (see section 2.1.2).

Typically, the least stable discrete eigenmodes is referred to as Tollmien-Schlichting wave.

Continuous Spectrum

In contrast to eigenfunctions of the discrete spectrum, modes of the continuous spectrum will not decay to zero outside the boundary layer. Therefore, the boundary condition (2.24) cannot be used as it would prevent the desired oscillations in the freestream. The outer boundary condition has to be relaxed to

$$\tilde{v} = \mathcal{D}\tilde{v} = \tilde{\eta} \text{ bounded as } y \to \infty. \tag{2.25}$$

Solutions of the continuous spectrum can either be found as solution to a general eigenvalue problem (see section 2.1.2) with an appropriate boundary condition. A second algorithm is shown in section 2.1.3, where an approximation in the freestream is used.

2.1.2 Solution via Eigensolver

The Orr-Sommerfeld equation (2.13) and the Squire equation (2.14) have to be solved complying with the no-slip condition (2.24) at the wall and the boundedness in the freestream (2.25).

The most straightforward way to do that is solving these two equations without any simplification. They consist of a generalized eigenvalue problem – fourth order in the velocity $\tilde{v}$ and second order in the vorticity $\tilde{\eta}$. Following the analysis of [14], a transformation of the form

$$\begin{pmatrix} \tilde{v} \\ \tilde{\eta} \end{pmatrix} = \begin{pmatrix} \tilde{V} \\ \tilde{E} \end{pmatrix} \exp(-\alpha y) \tag{2.26}$$

will reduce the order of the nonlinear eigenvalue problem by two. The introduction of the vector quantity $(\alpha\tilde{V}, \tilde{V}, \tilde{E})^T$ leads to a system of first-order differential equations

$$\begin{bmatrix} -R_1 & -R_0 & 0 \\ I & 0 & 0 \\ 0 & -S & -T_0 \end{bmatrix} \begin{pmatrix} \alpha\tilde{V} \\ \tilde{V} \\ \tilde{E} \end{pmatrix} = \alpha \begin{bmatrix} R_2 & 0 & 0 \\ 0 & I & 0 \\ 0 & 0 & T_1 \end{bmatrix} \begin{pmatrix} \alpha\tilde{V} \\ \tilde{V} \\ \tilde{E} \end{pmatrix} \tag{2.27}$$

with

$$R_2 = \frac{4}{\mathrm{Re}}\mathcal{D}^2 + 2iU\mathcal{D} \tag{2.28}$$

$$R_1 = -2i\omega\mathcal{D} - \frac{4}{\mathrm{Re}}\mathcal{D}^3 + \frac{4}{\mathrm{Re}}\beta^2\mathcal{D} - iU\mathcal{D}^2 + iU\beta^2 + iU'' \tag{2.29}$$

$$R_0 = i\omega\mathcal{D}^2 - i\omega\beta^2 + \frac{1}{\mathrm{Re}}\mathcal{D}^4 - \frac{2}{\mathrm{Re}}\beta^2\mathcal{D}^2 + \frac{1}{\mathrm{Re}}\beta^4 \tag{2.30}$$

$$T_1 = \frac{2}{\mathrm{Re}}\mathcal{D} + iU \tag{2.31}$$

$$T_0 = -i\omega - \frac{1}{\mathrm{Re}}\mathcal{D}^2 + \frac{1}{\mathrm{Re}}\beta^2 \tag{2.32}$$

$$S = i\beta U'. \tag{2.33}$$

The boundary conditions are the no-slip condition at the wall (2.24) and the boundedness in the freestream (2.25). The latter condition was implemented using the following constraints

$$\mathcal{D}\tilde{v} = \mathcal{D}^2\tilde{v} = \mathcal{D}\tilde{\eta} = 0. \tag{2.34}$$

In the present study, this system is solved using a standard eigensolver (`cgeco` from netlib). The spatial discretization is done with Chebyshev polynomials at the Gauss-Lobatto points. Solutions computed via the eigensolver can be either member of the continuous or of the discrete spectrum. Figure 2.1 shows a set of eigenvalues in the complex plane computed using the above algorithm, whereas figure 2.2 shows a typical eigensolution for a mode of the continuous spectrum.

To illustrate the difference between discrete and continuous modes, figure 2.3 shows a typical example of an eigenmode of the discrete part of the spectrum. As mentioned above, modes of the discrete spectrum have their maximum amplitude inside the boundary layer, whereas continuous modes are comparably small near the wall and reach an oscillatory state in the freestream.

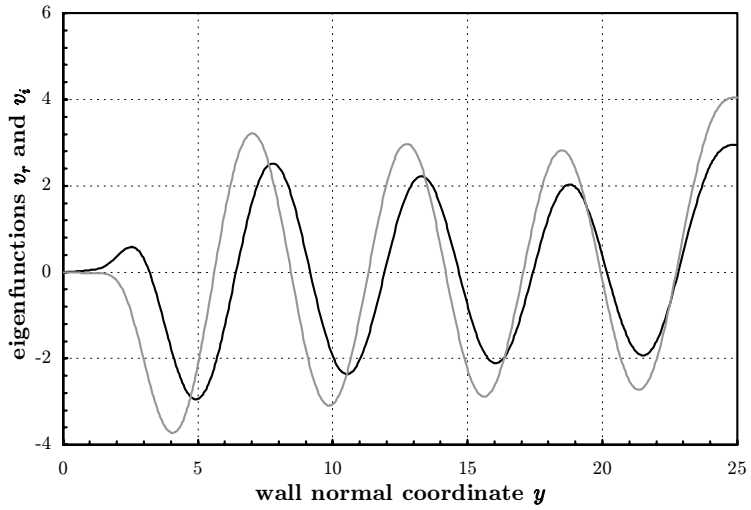

FIGURE 2.2: Typical example of a continuous eigenmode $\tilde{v}_r$ (black) and $\tilde{v}_i$ (gray). Parameters were $\omega = 0.2$, $\beta = 1$, Re=300, $\alpha = 0.20 + 0.0076i$, ($\gamma = 1.1116$). Numerical computation using standard eigensolver (see chapter 2.1.2).

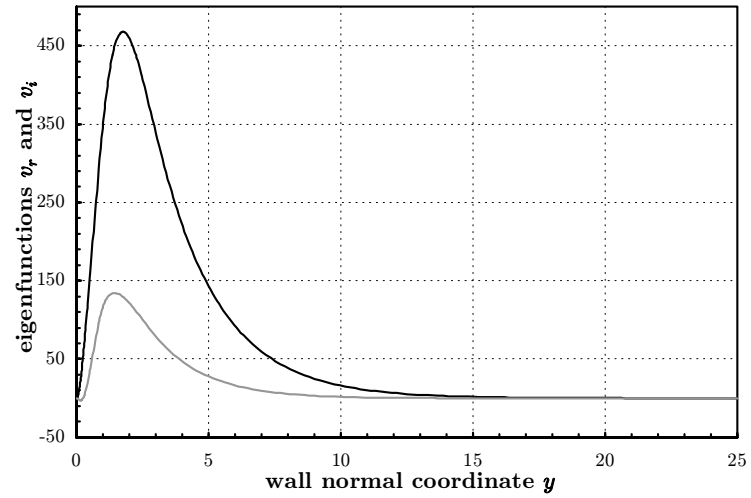

FIGURE 2.3: Typical example of a discrete eigenmode $\tilde{v}_r$ (black) and $\tilde{v}_i$ (gray). Parameters were $\omega = 0.2$, $\beta = 0$, Re=300, $\alpha = 0.44+0.017i$. Numerical computation using standard eigensolver (see chapter 2.1.2).

2.1.3 Solution for Continuous Spectrum

Similar to the preceding chapter, the Orr-Sommerfeld equation (2.13) and the Squire equation (2.14) have to be solved fulfilling the no-slip condition (2.24) at the wall and the boundedness in the freestream (2.25). In contrast to the last chapter, simplifications will be introduced to derive a solution.

The basic equations (2.13) and (2.14) can be simplified in the freestream, where the mean velocity U is constant and thereby the derivatives $U' = U''$ disappear,

to

$$\left[(-i\omega + i\alpha U)(\mathcal{D}^2 - \kappa^2) - \frac{1}{\mathrm{Re}}(\mathcal{D}^2 - \kappa^2)^2\right]\tilde{v} = 0 \tag{2.35}$$

$$\left[(-i\omega + i\alpha U) - \frac{1}{\mathrm{Re}}(\mathcal{D}^2 - \kappa^2)\right]\tilde{\eta} = 0, \tag{2.36}$$

yielding two uncoupled ordinary differential equations with constant coefficients of forth and second order, respectively.

First, consider equation (2.35). Following the notation of [12], the four exponential solutions can be written as

$$\tilde{v}_i \propto e^{\lambda_i y} \tag{2.37}$$

$$\lambda_1 = -\sqrt{Q} \qquad \lambda_2 = +\sqrt{Q} \qquad \lambda_3 = -\alpha \qquad \lambda_4 = +\alpha \tag{2.38}$$

$$Q = \mathrm{Re}(-i\omega + i\alpha U) + \kappa^2 = -\gamma^2 \tag{2.39}$$

with γ introduced as wall-normal wavenumber of the perturbations and $\kappa^2 = \alpha^2 + \beta^2$. In the case of spatial evolution the real part $\alpha_r = \Re(\alpha)$ of the wavenumber α is positive. In order to satisfy the boundedness of the solution (2.38), root four λ_4 has to be discarded, since it is exponentially growing with y. The eigenfunction in the freestream is thus formed by

$$\tilde{v} = A\tilde{v}_1 + B\tilde{v}_2 + C\tilde{v}_3 \tag{2.40}$$

$$= Ae^{-i\gamma y} + Be^{i\gamma y} + Ce^{-\alpha y} \tag{2.41}$$

and the eigenvalue α is given as a function of γ by

$$\alpha = \frac{i}{2}\left[\sqrt{(U\mathrm{Re})^2 + 4(\beta^2 + \gamma^2 - i\mathrm{Re}\omega)} - U\mathrm{Re}\right] \tag{2.42}$$

$$\alpha_r = \Re(\alpha) = \sqrt{\frac{1}{2}\left[\sqrt{b^2 + \omega^2\mathrm{Re}^2} - b\right]} \tag{2.43}$$

$$\alpha_i = \Im(\alpha) = \frac{1}{2}\mathrm{Re}\left(\frac{\omega}{\alpha_r} - U\right) \tag{2.44}$$

$$b = \frac{1}{4}\mathrm{Re}^2(U^2 + \gamma^2 + \beta^2) \tag{2.45}$$

Equations (2.43) and (2.44) can be used to plot a parametric curve of the freestream approximation of the continuous spectrum as shown in figure 2.1.

Considering the Squire equation (2.36) simplified for freestream conditions (2.36), similar results can be found

$$\tilde{\eta} = D\tilde{\eta}_1 + E\tilde{\eta}_2 \tag{2.46}$$

$$= De^{-i\gamma y} + Ee^{i\gamma y} \tag{2.47}$$

with the same expressions for α and γ as above.

It is important to note, that using this solution procedure, only pure OS modes and SQ modes are to be computed. The inclusion of the coupling term $-i\beta U'\tilde{v}$ in the Squire equation could lead to unwanted resonance, although the coupling term is zero in the freestream. The calculation of coupled eigenmodes needs to be done using the eigensolver (see chapter 2.1.2).

Numerical Solution

The numerical approach to solve the Orr-Sommerfeld equation for the eigenfunctions of the continuous spectrum used in [12] and partly in [16] was a 4^{th}-order Runge-Kutta scheme to integrate the Orr-Sommerfeld equation (2.13) from the uppermost grid point to $y = 0$. The theoretical shape of the oscillations in the freestream is known from the freestream solution (previous chapter 2.1.3), therefore providing boundary conditions. This method proved to be successful for sufficiently small ω, but failed due to roundoff error and the inherent stiffness of the Orr-Sommerfeld equation for general ω [15].

In this report, another method was used to compute the continuous modes. Rather than linearly combine different solutions $\tilde{v}_i$ resp. $\tilde{\eta}_i$, a boundary value problem with the collocation method in Chebyshev space was formulated [14]. To solve this problem, four boundary conditions for $\tilde{v}$ and two for $\tilde{\eta}$ have to be supplied. At the wall ($y = 0$), the boundary conditions read

$$\tilde{v}\big|_{y=0} = \tilde{v}'\big|_{y=0} = \tilde{\eta}\big|_{y=0}. \tag{2.48}$$

As second condition for $\tilde{\eta}$ and third for $\tilde{v}$, an arbitrary normalization is implemented in the freestream ($y = y_{\max}$)

$$\tilde{v}\big|_{y=y_{\max}} = \tilde{\eta}\big|_{y=y_{\max}} = 1 + 0 \cdot i. \tag{2.49}$$

The last boundary condition for $\tilde{v}$ should take into account the boundedness of the eigenfunctions, boundary condition (2.25). Following [16], it can be seen from equation (2.41) that the expression

$$\tilde{v}'' + \gamma^2 \tilde{v} = C(\alpha^2 + \gamma^2) e^{-\alpha y} \tag{2.50}$$

holds in the freestream. Thus, evaluating this expression at two points (y_1, y_2) in the freestream yields a boundary condition, which upholds the periodicity

$$\frac{\tilde{v}'' + \gamma^2 \tilde{v}\big|_{y_1}}{\tilde{v}'' + \gamma^2 \tilde{v}\big|_{y_2}} = e^{\alpha(y_2 - y_1)}. \tag{2.51}$$

Figure 2.4 shows a typical example of an eigenfunction computed using the above algorithm. It can clearly be seen, that – beginning at a certain wall-normal distance – the eigenfunction approaches a pure sinusoidal oscillation according to equation (2.41).

The qualitative behaviour of the solution to the Squire equation $\tilde{\eta}$ is similar.

2.2 Turbulence

A turbulent flow is characterized by an apparently random velocity field – in particular the varying velocity components seem to follow no rules. This phenomena is apparent to all turbulent quantities like velocity, vorticity, pressure and stress tensor.

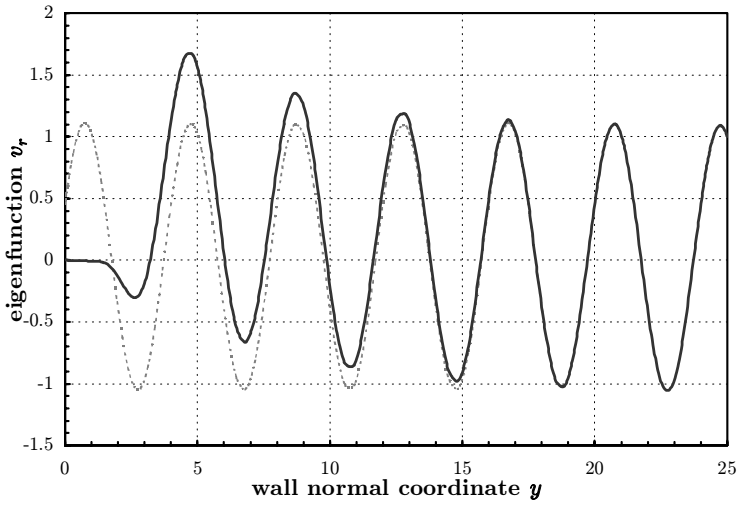

FIGURE 2.4: Typical example of a continuous eigenmode $\tilde{v}_r$ (black) approaching pure oscillation in the freestream (gray). Parameters were $\omega = 0.2$, $\beta = 0$, Re=300, $\gamma = \pi/2$, $(\alpha = 0.20 + 0.0084i)$. Numerical computation using the approximation algorithm of chapter 2.1.3.

2.2.1 Statistical Quantities

In order to allow an analysis of turbulent flows, the use of statistical methods is indicated. The Reynolds splitting of velocities is used to divide a velocity component into an averaged part $\overline{u}_i$ and a fluctuation part u_i'

$$u_i = \overline{u}_i + u_i' \quad \text{with} \quad \overline{u'}_i = 0. \tag{2.52}$$

The averaged part $\overline{u}_i(\underline{x})$ of the turbulent quantity $u_i(\underline{x}, t)$ can be calculated, dependent on the flow, either by averaging over time

$$\overline{u}_i(\underline{x}) = \lim_{T\to\infty} \frac{1}{T} \int_0^T u_i(\underline{x}, T_0 + t)dt \tag{2.53}$$

or by an ensemble average over a number n of independent realizations

$$\overline{u}_i(\underline{x}) = \lim_{n\to\infty} \frac{1}{n} \sum_{i=1}^{n} u_i(\underline{x}, t^i). \tag{2.54}$$

It is obvious that the temporal averaging is only appropriate for statistical stationary (e.g. temporally not decaying) flows. For stationary, but spatially decaying processes like spatial boundary layer simulations, a combined average in time and space can be applied. For that, the *Taylor Hypothesis* is used to convert a time signal into a spatial signal (and vice versa) with the substitution [27]

$$t = \frac{x}{U_\infty} \tag{2.55}$$

with t as time, x as spatial coordinate and U_∞ describing the mean velocity.

Besides the averaged values of a turbulent quantity, its fluctuation intensity is important. A way to express this is given by the root-mean-square (rms) value of a velocity component u_i defined as

$$u_{i,\mathrm{rms}} = \sqrt{\overline{(u_i')^2}} \quad \Rightarrow \quad u_{\mathrm{rms}} = \sqrt{\overline{(u')^2}} \quad v_{\mathrm{rms}} = \sqrt{\overline{(v')^2}} \quad w_{\mathrm{rms}} = \sqrt{\overline{(w')^2}} \tag{2.56}$$

It is important to note, that the term rms-velocity is sometimes used with a different meaning (see for example [27]). There, the definition is given as follows

$$U_{\mathrm{rms}} = \sqrt{\frac{\overline{u_l' u_l'}}{3}} = \sqrt{\frac{\overline{(u')^2} + \overline{(v')^2} + \overline{(w')^2}}{3}}, \tag{2.57}$$

providing an arithmetic average of the velocity fluctuations in all directions. To avoid confusion between the definitions (2.56) of $u_{1,\mathrm{rms}} = u_{\mathrm{rms}}$ and (2.57) of U_{rms}, the use of the latter definition is indicated by a capital U.

Closely linked to the rms-value of the velocity are the definitions of the turbulence intensity Tu and the turbulent kinetic energy k. The turbulence intensity is defined as

$$\mathrm{Tu} = \sqrt{\frac{\overline{u_l' u_l'}}{3\overline{u}_i \overline{u}_i}} = \frac{U_{\mathrm{rms}}}{\sqrt{\overline{u}_i \overline{u}_i}} \tag{2.58}$$

and allows a comparison of the magnitude of the local turbulent fluctuations u_i' to the averaged velocity $\overline{u}_i$.

The turbulent kinetic energy k of the turbulent fluctuations is defined as

$$k = \frac{\overline{u_l' u_l'}}{2} = \frac{3}{2}(U_{\mathrm{rms}})^2. \tag{2.59}$$

Both, k and Tu are measures for the intensity of the perturbations in a turbulent flow and are therefore a characteristic quantity for the strength of the turbulence. Especially in isotropic turbulence, Tu is widely used to express the disturbance level.

2.2.2 Homogeneous Isotropic Turbulence

Homogeneous isotropic turbulence means, that the statistical average of the turbulence quantities are dependent neither on the spatial location (homogeneous) nor the direction (isotropic) of the measurement. This assumption leads to several simplifications in the calculation of flow quantities like spectra and energies [23],[27]. Although homogeneous isotropic turbulence is not exactly observable in nature, turbulence e.g. caused by a grid is sufficiently close to isotropy to be considered isotropic.

It is obvious that for isotropic turbulence the proportion of the kinetic energy k and the rms-values is the same for every velocity component, because the influence

of the different spatial directions should vanish for averaged quantities, e.g.

$$k_1 = \frac{\overline{u_1' u_1'}}{2} \qquad k_2 = \frac{\overline{u_2' u_2'}}{2} \qquad k_3 = \frac{\overline{u_3' u_3'}}{2} \tag{2.60}$$

$$k \simeq 3k_1 \simeq 3k_2 \simeq 3k_3. \tag{2.61}$$

Important results can be obtained using Fourier decomposition of the velocity components. This transformation basically translates velocity fluctuations from the physical space (x, y, z or via Taylor hypothesis t, y, z) into the spectral (wavenumber) space (α, γ, β or ω, γ, β). Computing for example the kinetic energy in spectral space will give important information about what scales in the flow carry which part of the total kinetic energy.

Formally, the process of computing the spectral energy can be described using the spatial two-point correlation tensor R_{ij}^r of the velocity [27]

$$R_{ij}^r(\underline{x}, \underline{r}) = \overline{u_i'(\underline{x}) u_j'(\underline{x} + \underline{r})}. \tag{2.62}$$

Applying a spatial Fourier transform of R_{ij}^r over the volume V yields the spectral tensor $\phi_{ij}(\underline{\kappa})$

$$\phi_{ij}(\underline{\kappa}) = \frac{1}{(2\pi)^3} \int_V R_{ij}^r(\underline{x}, \underline{r}) \exp(-i\underline{\kappa r}) d\underline{r}, \tag{2.63}$$

where $\phi_{ij}(\underline{\kappa})$ is for a fixed location $\underline{x}$ only dependent on the wavevector $\underline{\kappa} = [\kappa_1, \kappa_2, \kappa_3]$. The diagonal elements $\phi_{ll}/2$ of the spectral tensor are directly related to the kinetic energy through

$$k = \frac{\overline{u_l' u_l'}}{2} = \frac{1}{2} R_{ll}^r(|\underline{r}| = 0) = \frac{1}{2} \int_{V(\underline{\kappa})} \phi_{ll}(\underline{\kappa}) d\underline{\kappa}. \tag{2.64}$$

The components of the tensor $\phi_{ll}(\underline{\kappa})/2$ represent the energy present in perturbations with the respective three-dimensional wavevector $\underline{\kappa}$. Therefore, information of the direction of disturbances is still available in $\phi_{ll}(\underline{\kappa})/2$.

Especially for isotropic turbulence where any influence of the different directions should be non-existent, the computation of an energy spectrum $E(\kappa)$ only dependent on a scalar wavenumber κ is indicated. Since information of all directions is captured in $E(\kappa)$ it is called three-dimensional spectrum [27].

Such a three-dimensional spectrum is usually derived using the above introduced three-dimensional spectral tensor $\phi_{ll}(\underline{\kappa})/2$. Integrating over sphere shells $|\underline{\kappa}| = \kappa$ gives

$$E(\kappa) = \frac{1}{2} \oint_{|\underline{\kappa}|=\kappa} \phi_{ll}(\underline{\kappa}) d\Omega \tag{2.65}$$

with $d\Omega$ denoting a surface element of the sphere shell. It can easily be seen, that the integral over $E(\kappa)$ is the total kinetic energy k

$$k = \int_0^\infty E(\kappa) d\kappa. \tag{2.66}$$

A possibility to calculate one-dimensional spectra uses only one-dimensional Fourier transforms. Computing the one-dimensional Fourier transform of the velocity components u_i in the x_i direction and averaging over the planes orthogonal to x_i will lead to the one-dimensional energy spectrum $E^{1D}(\kappa_i)$ of the i^{th} velocity component. By comparing the spectra of the different directions $i = 1, 2, 3$ and the three-dimensional spectrum, a measure for isotropy is given.

A three-dimensional energy spectrum $E(\kappa)$ and a one-dimensional spectrum $E^{1D}(\kappa_i)$ is known to have a specific shape for non-bounded homogeneous isotropic turbulence – dependent only on the total energy k and the wavenumber of the peak energy value. There are many analytical forms of the spectrum. In this work, the

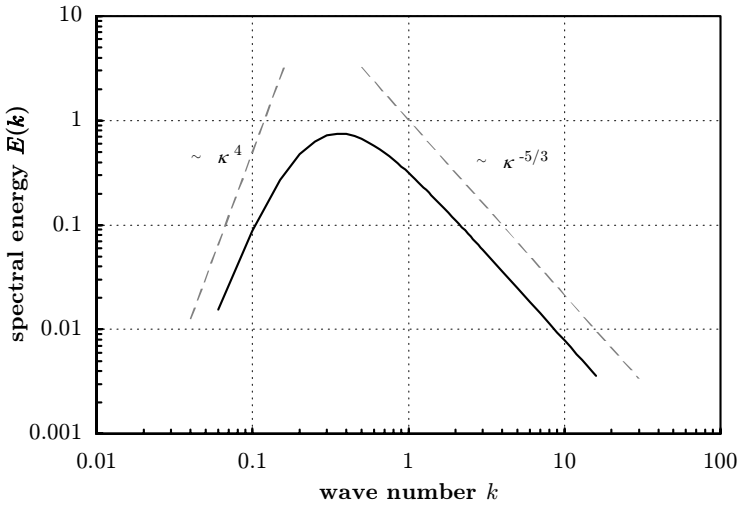

FIGURE 2.5: One-dimensional von Kármán energy spectrum according to equation (2.69). Computed for integral length scale $L_I = 5$ and total energy $k = 1$.

von Kármán spectrum is used with the following form [15]

$$E(\kappa) \propto \frac{\kappa^4}{(C + \kappa^2)^{17/6}}. \tag{2.67}$$

This spectrum is for large scales asymptotically proportional to κ^4, whereas it matches the Kolmogorv-(5/3)-law for small scales [27]. Figure 2.5 shows a von Kármán spectrum.

Following the construction of the three-dimensional spectrum in [27], an integral length scale L_I of the turbulence is introduced according to

$$L_I = \frac{1.8}{\kappa_{\max}} \qquad \text{with} \qquad E(\kappa = \kappa_{\max}) = \max. \tag{2.68}$$

Together with the constraint (2.66), the following formulation of the energy spectrum can be derived from equation (2.67)

$$E(\kappa) = \frac{2}{3} k L_I \frac{1.606(\kappa L_I)^4}{\left(1.350 + (\kappa L_I)^2\right)^{17/6}}. \tag{2.69}$$

The length scale L_{11} obtainable from the longitudinal two-point correlation is related to L_I according to

$$L_{11} = \int_0^\infty \frac{\overline{u'(x)u'(x+r)}}{\overline{(u')^2}} dr = \frac{3\pi}{2k} \int_0^\infty \frac{E(\kappa)}{\kappa} d\kappa \approx 1.286 L_I. \tag{2.70}$$

2.3 Modeling of Freestream Turbulence

To construct a realistic initial flow field for isotropic freestream turbulence, a similar approach as in [16] is used in this thesis. Section 2.1.1 describes how eigenmodes of the continuous spectrum reach a sinusoidal oscillatory state as the wall normal distance increases. Therefore, a three-dimensional wavenumber $\underline{\kappa} = (\alpha, \gamma, \beta)$ in the freestream can be associated with every continuous eigenmode using equation (2.39).

As pointed out in [12], the continuous eigenmodes provide a natural basis for freestream turbulence. Using these eigenmodes as basis, the expression for a general disturbance can be written as

$$u_i(x, y, z, t) = \sum_\alpha \sum_\beta \sum_\omega \Phi(\alpha, \beta, \omega) \tilde{u}_i(y, \alpha, \beta, \omega) e^{i(\alpha x + \beta z - \omega t)}. \tag{2.71}$$

Here $\tilde{u}_i$ describes the solutions of the Orr-Sommerfeld / Squire equations for the velocity components according to equations (2.11), (2.18) and (2.19), whereas Φ is introduced as scaling factor for every individual eigenmode.

By carefully choosing a finite set of wavenumbers α and β and through equation (2.39) γ, it is possible to construct an initial disturbance with a given spectrum, e.g. the von Kármán energy spectrum (2.69). For that, every eigenfunction has to be scaled by a factor which can be computed from the target spectrum. Furthermore, as the free stream turbulence has to be isotropic, the wavenumbers which are included in the summation should be chosen isotropically distributed as well.

2.3.1 Isotropically Distributed Wavenumbers

In order to attain isotropic turbulence, a certain finite number of wavenumbers has to be chosen out of the infinite domain $\alpha_{\min} < \Re(\alpha) < \alpha_{\max}$, $\beta_{\min} < \beta < \beta_{\max}$, $\gamma_{\min} < \gamma < \gamma_{\max}$, where the minimal and maximal wavenumbers are given by the desired resolution of the wavenumber space. The basic idea is to divide the wavenumber space into a set of concentrical spherical shells. On the surface of each shell a number of wavenumbers should be picked and included in the summation (2.71) with appropriate scaling. This procedure allows to reduce the task of choosing the wavenumbers to place a number of points isotropically (regularly) on the surface of a sphere.

Placing points regularly on a sphere is similar to the problem in classical geometry to construct a regular polyeder. A polyeder is a geometrical volume limited by plane polygon as faces. A special kind of polyeder are regular polyeder. There, as further condition all of the limiting polygons need to be congruent and regular

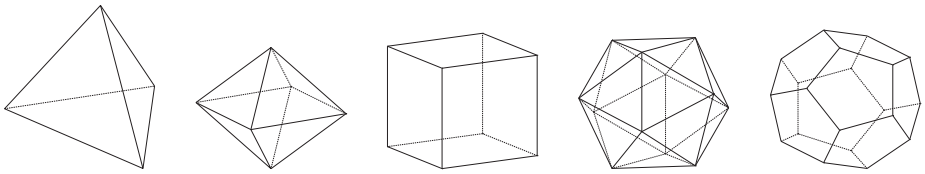

FIGURE 2.6: The five only possible regular polyeder: Tetraeder (4 corners), octaeder (6 corners), cube (8 corners), icosaeder (20 corners) and dodecaeder (20 corners).

on their own. It has been proved by Leonhard Euler in the 17$^{\text{th}}$ century, that only 5 different regular polyeder can exist [11] (see figure 2.6).

Regularly distributed points on a sphere can now be calculated using well known trigonometric relations for the corner coordinates of these polyeder. Additionally, a random spatial rotation of the points around the center (0/0/0) can be performed.

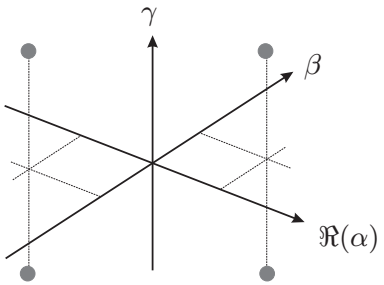

FIGURE 2.7: Wavenumbers simultaneously included when choosing one wavenumber: $(\Re(\alpha), \beta, \gamma)$, $(-\Re(\alpha), -\beta, -\gamma)$, $(\Re(\alpha), \beta, -\gamma)$, $(-\Re(\alpha), -\beta, \gamma)$.

Some specializations must be made concerning the distribution of wavenumbers for the construction of freestream turbulence. First, only half of the sphere must be considered due to the fact, that the complex Fourier transformation of a real quantity (velocity) only needs half of the whole wavenumber space [9]. Second, it can be seen from equation (2.41) that by choosing an eigenfunction with the wall-normal wavenumber $+\gamma$ automatically the negative wavenumber $-\gamma$ is included in the solution as well. Therefore, only half of the domain in γ has to be included in the summation (2.71) (see figure 2.7). Thirdly, zero values for α and γ make no physical sense (standing waves) and must therefore be averted. Through adequate 3-D rotation of the points, this can easily be achieved. The forth specialization is concerned with the discretization of the numerical domain. As it will be shown in chapter 3, the flow equations are solved in Fourier space in the spanwise direction z. Therefore, only β wavenumbers are allowed which are an integer multiple of the smallest scales in the z-direction.

In the present study, the geometrical form of the dodecaeder (figure 2.6) with 20 corner points was used with a random three dimensional spatial rotation. Hereby it is ensured, that both $\Re(\alpha) \neq 0$ and $\gamma \neq 0$.

A second dodecaeder was then superimposed with all points mirrored at the

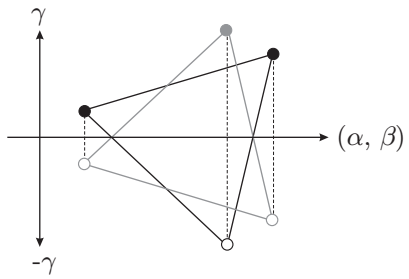

FIGURE 2.8: Simple example showing the importance of the inclusion of the mirrored geometrical form (see text). The inclusion of the black dots in the sum (2.41) implies the inclusion of the gray circles (mirrored). To maintain isotropy, the mirrored triangle (gray) is considered as well.

α/β-plane. This is done to get corresponding points with the negative γ-coordinates in the summation in order to always include $+\gamma$ and $-\gamma$ modes, see equation (2.41). From these 40 points, only the 10 points in the quadrant $\Re(\alpha) > 0$ and $\gamma > 0$ were taken and their eigenfunctions were included in the summation (2.71).

Figure 2.8 explains this procedure with the two-dimensional example of a triangle. Consider a triangle (black). By including the two points with $\gamma > 0$, the two gray corner points with $\gamma < 0$ are included as well by the means of equation (2.41). To ensure highly isotropic distribution of the points, the corners of the gray triangle with $\gamma > 0$ are included in the sum as well.

Finally, figure 2.9 shows a typical distribution of points obtained by the above procedure, seen in a α/γ-plane.

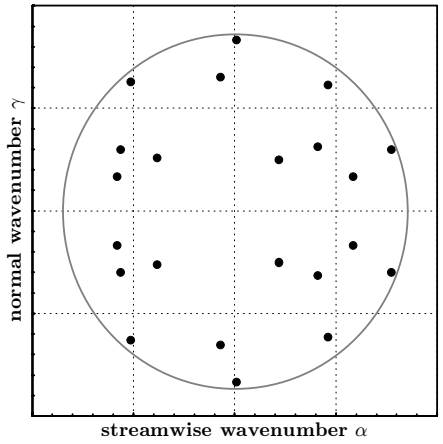

FIGURE 2.9: Regular distribution of points on a sphere according to the scheme described in the text. Points with $\beta \geq 0$ shown in a α/γ plane. Because for one of the points $\beta = 0$, 22 instead of 20 points are drawn.

2.3.2 Scaling of the Eigenmodes

Once the wavenumbers for the eigenmodes to include in the freestream turbulence have been identified, the respective eigensolutions to the Orr-Sommerfeld / Squire equations need to be calculated. In section 2.1.2 and 2.1.3 two solution procedures have been introduced: The computation via eigensolver and the calculation using the solution in the freestream. It has been found, that the eigensolver will – at least for some wavenumbers – not find oscillatory solutions in the freestream due to the boundary condition imposed at the upper boundary. Therefore, for the construction of the freestream turbulence, the calculation using freestream approximation (section 2.1.3) was used in the present thesis. Since this algorithm complys with continuity, the summation of eigenmodes provides a disturbance which satisfies continuity as well.

As pointed out in section 2.1.3, the algorithm only provides pure Orr-Sommerfeld and Squire modes with neglecting their coupling term. Therefore, for a given wavevector, both an Orr-Sommerfeld and a Squire mode was calculated

$$\text{OS-mode:} \qquad \tilde{u}_{\mathrm{OS}}, \tilde{v}_{\mathrm{OS}}, \tilde{w}_{\mathrm{OS}} \tag{2.72}$$

$$\text{SQ-mode:} \qquad \tilde{u}_{\mathrm{SQ}}, 0, \tilde{w}_{\mathrm{SQ}}. \tag{2.73}$$

On both solutions, an arbitrary phase shift was applied before adding them together with random weights to form the final disturbance at a given wavenumber

$$\tilde{u}(y,\alpha,\beta,\omega) = \cos(r_1)e^{i\cdot r_2}\tilde{u}_{\mathrm{OS}} + \sin(r_1)e^{i\cdot r_3}\tilde{u}_{\mathrm{SQ}} \tag{2.74}$$

$$\tilde{v}(y,\alpha,\beta,\omega) = \cos(r_1)e^{i\cdot r_2}\tilde{v}_{\mathrm{OS}} \tag{2.75}$$

$$\tilde{w}(y,\alpha,\beta,\omega) = \cos(r_1)e^{i\cdot r_2}\tilde{w}_{\mathrm{OS}} + \sin(r_1)e^{i\cdot r_3}\tilde{w}_{\mathrm{SQ}} \tag{2.76}$$

with r_1, r_2 and r_3 denoting random numbers in $[0, 2\pi)$ and i as the complex unit.

In order to construct an energy spectrum according to equation (2.69), each disturbance ($\tilde{u}$, $\tilde{v}$, $\tilde{w}$) needs to be scaled to the required energy. The most straightforward way to do that is numerically calculating the energy of such a disturbance and normalize it to unit energy. In this study, this is done by calculating the energy per unit volume in a test volume V

$$k^* = \frac{\overline{u_l' u_l'}}{2} = \frac{1}{2}\frac{1}{V}\int_V (\tilde{u}^2 + \tilde{v}^2 + \tilde{w}^2) dV \tag{2.77}$$

and scaling every eigenfunction by $\sqrt{1/k^*}$ to get unit energy. To meet the spectral energy given by (2.69), a further scaling with a factor $\sqrt{\psi}$ has to be performed according to

$$\psi(\kappa) = E(\kappa)\frac{\Delta\kappa}{n_i}. \tag{2.78}$$

Here, $E(\kappa)$ is the desired energy spectrum, $\kappa = \sqrt{\Re(\alpha)^2 + \beta^2 + \gamma^2}$ the wavenumber, $\Delta\kappa$ the difference in wavenumber between to subsequent sphere shells and n_i the respective number of modes on a shell. Hereby it is ensured that

$$\int_0^\infty E(\kappa) d\kappa \approx \sum_{\kappa_i} n_i \left[\frac{E(\kappa_i)\Delta\kappa}{n_i}\right] = \sum_{\kappa_i} n_i \psi(\kappa). \tag{2.79}$$

The overall scaling for each individual disturbance is thus given by

$$\tilde{u}(y,\alpha,\beta,\omega)^* = \sqrt{\frac{\psi}{k^*}}\tilde{u}(y,\alpha,\beta,\omega) \quad (2.80)$$

$$\tilde{v}(y,\alpha,\beta,\omega)^* = \sqrt{\frac{\psi}{k^*}}\tilde{v}(y,\alpha,\beta,\omega) \quad (2.81)$$

$$\tilde{w}(y,\alpha,\beta,\omega)^* = \sqrt{\frac{\psi}{k^*}}\tilde{w}(y,\alpha,\beta,\omega). \quad (2.82)$$

Combining all scaled individual disturbances into the summation (2.71) with $\Phi = \sqrt{\frac{\psi}{k^*}}$ will lead to a disturbance field $u_i(x,y,z,t)$ that meets the given energy spectrum $E(\kappa)$ (2.69). Figure 2.10 shows the computed spectrum of a disturbance constructed according to the above procedure. The discrepancy between the measured spectrum and the desired one for low wavenumbers can be explained by coarse resolution of the Fourier transform for small wavenumbers.

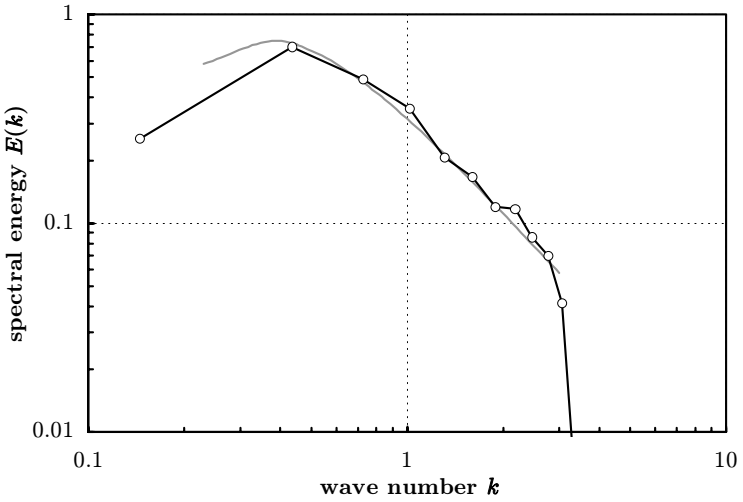

FIGURE 2.10: One-dimensional energy spectrum calculated for superposition of Orr-Sommerfeld and Squire modes. To compare, the desired von Kármán spectrum is shown (gray, see figure 2.5). Parameters: 20 shells with 10 points each (200 eigenmodes) , k=[0.23, 3], integral length scale $L_I = 5$, total energy $k = 1$.

Several tests have shown, that such a disturbance is very isotropic. The rms-fluctuations in the three coordinate directions u_{rms}, v_{rms} and w_{rms} are all within 3% of the mean value (Tu). Moreover, the comparison of different two-dimensional spectra showed good agreement. Further description of the freestream turbulence can be found in chapter 4.

Chapter 3

Numerical Method

The numerical solution of the Navier-Stokes equations especially for the simulation of transitional and turbulent flows requires high numerical accuracy for a large span of length scales. Since the direct numerical simulation (DNS) approach includes resolving all these scales without approximations or modeling, it is important that efficient numerical schemes are applied. Moreover, for fast calculation the computational domain should be as small as possible and the resolution coarse – but still as fine as necessary for the desired accuracy/application.

3.1 Computational Domain

The simulations presented in this report deal with the spatial evolution of a boundary layer subject to freestream turbulence. Usually, simulations tend to cover – like in experimental setups – the whole domain including the location, where the freestream turbulence is generated, which is usually upstream of the leading edge and the plate. A lot of valuable computing resources are used to simulate the – in fact not desired and irrelevant to the boundary layer growth – region upstream of the leading edge.

In this report, a technique similar to [16] is used. The disturbances which form the freestream turbulence are a superposition of eigensolutions to the Orr-Sommerfeld and Squire equations. As described in chapter 2, these eigenmodes provide a natural basis for freestream turbulence above a flat plate. Therefore, it is not required to introduce the disturbances upstream of the leading edge of the plate and let these disturbances evolve – on the contrary, the computational domain even starts at a certain distance x_0 downstream of the leading edge. This technique allows that the evolution of the initial freestream turbulence before the leading edge does not need to be calculated. It is therefore saving a lot of computational time and memory.

The computational domain basically consists of a three-dimensional cuboid bounded at the lower edge by the flat plate (see figure 3.1) with a no-slip boundary condition. The plate boundary layer will evolve in the computational domain starting with an initial boundary layer thickness δ_0 resp. δ_0^*. In the streamwise direction, the computational domain is bounded by the fringe region (see below),

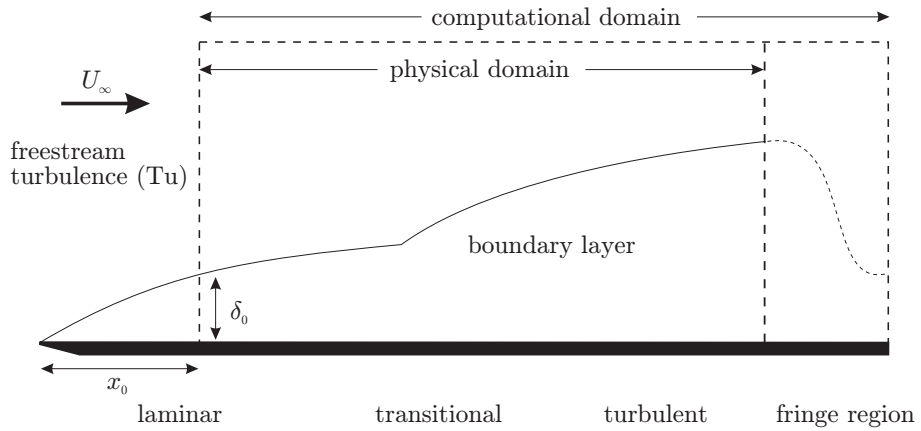

FIGURE 3.1: Location of the computational domain with respect to the plate, leading edge, boundary layer and fringe region (not to scale).

whereas the boundary conditions in the spanwise direction are periodic.

The relevant quantities of the flow can be scaled with the inlet boundary layer thickness δ_0, the freestream velocity U_∞ and the viscosity ν. The characteristic Reynolds number based on the displacement thickness at the inlet δ_0^* is given by

$$\mathrm{Re}_{\delta_0^*} = \frac{\delta_0^* U_\infty}{\nu}. \tag{3.1}$$

The distance from the leading edge, x_0, can be computed using

$$\frac{x_0}{\delta_0^*} = \mathrm{Re}_{\delta_0^*} \frac{1}{(1.7208)^2}. \tag{3.2}$$

Typical dimensions of the computational domain are in the present study a streamwise length of $1000\delta_0^*$, a spanwise width of $50\delta_0^*$ and a height of $60\delta_0^*$. The fringe length accounts for around 10% of the streamwise extent. All simulations were started from an inlet Reynolds number $\mathrm{Re}_{\delta_0^*} = 300$.

3.2 Numerical Scheme

As already pointed out, the use of efficient numerical algorithms is important due to the immense amount of data to be processed during a direct numerical simulation. Therefore, spectral methods are a common choice for DNS. In spectral methods the solution is approximated by an expansion of smooth (global) functions which provides a fast convergence rate to the approximation of the real solution. Moreover, higher accuracy per included spectral mode compared to the accuracy produced by finite-element or finite difference discretizations with corresponding number of grid points can be reached.

The use of spectral methods in fluid dynamics dates back in the early 1970s. It was then, when these methods were termed pseudo-spectral methods. The reason is, that not the whole computation is done in spectral space – the multiplications of

the nonlinear terms of the flow equations are calculated in physical space to avoid the evaluation of convolution sums. The transformation between physical and spectral space can be efficiently done by fast Fourier transform (FFT) algorithms [8].

The numerical code used for the calculations presented in this study is a variant of the boundary layer code `bla`, which has been developed and improved over the past years at KTH Stockholm. It has been successfully applied in a number of works, see for example [5], [25] etc. Extensive documentation to the code and the numerical scheme can be found in [18]. The following adapted description is partly taken from [18].

3.2.1 Velocity - Vorticity Formulation

The algorithm solves the full three-dimensional incompressible Navier-Stokes equations and continuity, see equations (2.1) and (2.2). In tensor notation, they read [18]

$$\frac{\partial u_i}{\partial t} = -\frac{\partial p}{\partial x_i} + \epsilon_{ijk} u_j \omega_k - \frac{\partial}{\partial x_i}(\frac{1}{2} u_j u_j) + \frac{1}{\mathrm{Re}} \nabla^2 u_i + F_i \tag{3.3}$$

$$\frac{\partial u_i}{\partial x_i} = 0 \tag{3.4}$$

with ω_i as vorticity component i. F_i denotes a body force, which is used for numerical purposes in the fringe region (see section 3.2.3). ϵ_{ijk} is the permutation symbol defined as

$$\epsilon_{ijk} = \begin{cases} 1 & \text{even permutation of } (i,j,k) \\ -1 & \text{odd permutation of } (i,j,k) \\ 0 & \text{else} \end{cases} \tag{3.5}$$

A Poisson equation for the pressure can be obtained by taking the divergence of the momentum equation (3.3)

$$\nabla^2 p = \frac{\partial H_i}{\partial x_i} - \nabla^2(\frac{1}{2} u_j u_j) \tag{3.6}$$

where $H_i = \epsilon_{ijk} u_j \omega_k + F_i$. Application of the Laplace operator to the momentum equation for the normal velocity v yields an equation for that component through the use of equations (3.6) and (3.4). One finds

$$\frac{\partial \nabla^2 v}{\partial t} = \left(\frac{\partial^2}{\partial x^2} + \frac{\partial^2}{\partial z^2} \right) H_2 - \frac{\partial}{\partial y}(\frac{H_1}{\partial x} + \frac{\partial H_3}{\partial z}) + \frac{1}{\mathrm{Re}} \nabla^4 v. \tag{3.7}$$

This equation can, for numerical purposes, be written as a system of two second order equations

$$\begin{aligned} \frac{\partial \phi}{\partial t} &= h_v + \frac{1}{\mathrm{Re}} \nabla^2 \phi \\ \nabla^2 v &= \phi, \end{aligned} \tag{3.8}$$

where

$$h_v = \left(\frac{\partial^2}{\partial x^2} + \frac{\partial^2}{\partial z^2}\right) H_2 - \frac{\partial}{\partial y}\left(\frac{\partial H_1}{\partial x} + \frac{\partial H_3}{\partial z}\right). \tag{3.9}$$

An equation for the normal vorticity η can be found by taking the curl of the momentum equation. The second component of that equation reads

$$\frac{\partial \eta}{\partial t} = h_\eta + \frac{1}{\mathrm{Re}}\nabla^2 \eta, \tag{3.10}$$

where

$$h_\eta = \frac{\partial H_1}{\partial z} - \frac{\partial H_3}{\partial x}. \tag{3.11}$$

Note that the equations for ϕ, v and η (3.8) and (3.10) have similar form, and can thus be solved using the same numerical routine. Once the the normal velocity v and the normal vorticity η have been calculated, the other velocity components can be found form the incompressibility constraint and the definition of the normal vorticity.

In the spanwise direction, the boundary conditions are periodic. At the plate ($y = 0$), the no-slip boundary condition reads

$$v\big|_{y=0} = 0 \qquad \frac{\partial v}{\partial y}\Big|_{y=0} = 0 \qquad w_2\big|_{y=0} = 0. \tag{3.12}$$

In the freestream, a von Neumann condition is implemented

$$\frac{\partial u_i}{\partial y}\Big|_{y=y_L} = \frac{\partial \mathcal{U}_i}{\partial y}\Big|_{y=y_L} \tag{3.13}$$

with $\mathcal{U}_i(y)$ as base flow (Blasius boundary layer, see appendix A.2). It should be noted, that the code allows the use of many other boundary conditions, but for the present study the above condition seemed to be reasonable.

The boundary conditions in the streamwise direction have to be treated using the fringe region (see section 3.2.3).

3.2.2 Discretization

The spatial discretization uses Fourier series expansion in the wall parallel (streamwise x and spanwise z) directions. The wall-normal direction (y) is discretized using Chebyshev series where the Chebyshev tau method (CTM) was applied to solve for the functions [18].

The time advancement used is a four-step low storage fourth-order Runge-Kutta method for the nonlinear terms and a second order Crank-Nicholson method for the linear terms. The non-linear terms are calculated in physical space rather than in spectral space (pseudo-spectral method). Aliasing errors due to the evaluation in the physical space are removed by the 3/2-rule when the horizontal FFTs are calculated.

i	$a_n/\Delta t^n$	$b_n/\Delta t^n$	$c_n/\Delta t^n$
1	8/17	0	0
2	17/60	-15/68	8/17
3	5/12	-17/60	8/15
4	3/4	-5/12	2/3

TABLE 3.1: Time-stepping coefficients for the 4-stage Runge-Kutta scheme (RK3)

The time advancement is carried out by a semi-implicit scheme. The following equation

$$\frac{\partial \psi}{\partial t} = G + L\psi, \tag{3.14}$$

is of the same form as equation (3.8) and (3.10). ψ represents ϕ or η, G contains the (nonlinear) advective and forcing terms and depends on all velocity and vorticity components, L is the (linear) diffusion operator. L is discretized implicitly using the second order accurate Crank-Nicholson (CN) scheme and G explicitly by a low storage four stage Runge-Kutta (RK3) scheme. The time discretization may be written in the following form (G and L are assumed to have no explicit dependence on time)

$$\psi^{n+1} = \psi^n + a_n G^n + b_n G^{n-1} + (a_n + b_n)\left(\frac{L\psi^{n+1} + L\psi^n}{2}\right), \tag{3.15}$$

where the constants a_n and b_n are shown in table 3.1. Note that the RK3 scheme implies that a full physical time step is only achieved every four iterations. The time used for the intermediate stages are given by $t = t + c_n$, where c_n is also given in table 3.1.

If the time advancement scheme (3.15) is applied to equations (3.8) and (3.10) we find (neglecting the boundary conditions),

$$\begin{aligned}(1 - \frac{a_n + b_n}{2\mathrm{Re}}\nabla^2)\phi^{n+1} &= (1 + \frac{a_n + b_n}{2\mathrm{Re}}\nabla^2)\phi^n + a_n h_v^n + b_n h_v^{n-1} \\ \nabla^2 v^{n+1} &= \phi^{n+1}\end{aligned} \tag{3.16}$$

and

$$(1 - \frac{a_n + b_n}{2\mathrm{Re}}\nabla^2)\eta^{n+1} = (1 + \frac{a_n + b_n}{2\mathrm{Re}}\nabla^2)\eta^n + a_n h_\eta^n + b_n h_\eta^{n-1}. \tag{3.17}$$

Although no rigorous stability criterion for the Navier-Stokes equations integrated by a Runge-Kutta scheme exists, some insight can be obtained by looking at model equations [18]. The spectral CFL number is then defined as

$$\mathrm{CFL} = \Delta t \pi \max_i \left(\frac{|u^i|}{\Delta x} + \frac{|v^i|}{\Delta y} + \frac{|w^i|}{\Delta z}\right) \tag{3.18}$$

with i describing all grid points. The stability analysis for the four stage Runge-Kutta method shows a stability limit of $\mathrm{CFL} = \sqrt{8}$. This is used in the adaptive time stepping to calculate the maximal stable time step Δt.

3.2.3 Fringe Region

Since the boundary layer is developing in the downstream direction, it is necessary to use non-periodic boundary conditions in the streamwise direction (inflow and outflow). This is possible while retaining the (periodic) Fourier discretization if a fringe region is added downstream of the physical domain (see figure 3.1). In the fringe region disturbances of the physical outflow are damped and the flow returned to the desired inflow condition. This is accomplished by the addition of a volume force. The fringe region only increases the execution time of the algorithm by a few percent [25].

The general form of the forcing is given by

$$F_i = \lambda(x)(\mathcal{U}_i^{\text{act}} - u_i) \tag{3.19}$$

where $\lambda(x)$ is a non-negative fringe function which is non-zero only within the fringe region. $\mathcal{U}_i^{\text{act}}$ is the base flow with the superimposed desired inflow disturbances and also contains the desired flow solution in the fringe. u_i denotes the local (computed) velocity.

The streamwise velocity component $\mathcal{U}_x$ of the undisturbed fringe base flow is calculated as

$$\mathcal{U}_x(x,y) = U(x,y) + [U(x+x_L,y) - U(x,y)]\, S\left(\frac{x - x_{\text{mix}}}{\Delta_{\text{mix}}}\right), \tag{3.20}$$

where $U(x,y)$ is a solution to the boundary layer equations (Blasius boundary layer appendix A.2). x_L denotes the extent of the computational domain and the step function S is given below. Note that x has to be a negative number describing the distance downstream of the beginning of the computational domain.

In equation (3.20), x_{mix} and Δ_{mix} are chosen so that the prescribed flow, within the fringe region, smoothly changes from the outflow velocity of the physical domain to the desired inflow velocity. The wall normal component $\mathcal{U}_y$ is then calculated from the equation of continuity, and the spanwise velocity $\mathcal{U}_z$ is set to zero, since the base flow $\mathcal{U}$ is only two-dimensional. This choice of $\mathcal{U}_i$ ensures that for the undisturbed laminar boundary layer the decrease in thickness is completely confined to the fringe region, thus minimizing the upstream influence.

Disturbances to the laminar flow can be given as inflow condition with superimposing them in $\mathcal{U}_i$ to form the actual forcing term $\mathcal{U}_i^{\text{act}}$. This technique is used to generate the freestream turbulence and will be further discussed in section 3.3.

A convenient form of the fringe function λ is as follows (see figure 3.2)

$$\lambda(x) = \lambda_{\max}[S(\frac{x - x_{\text{start}}}{\Delta_{\text{rise}}}) - S(\frac{x - x_{\text{end}}}{\Delta_{\text{fall}}} + 1)] \tag{3.21}$$

Here $\lambda_{\max}$ is the maximum strength of the damping, x_{start} to x_{end} the spatial extent of the region where the damping function is nonzero and Δ_{rise} and Δ_{fall} the rise and fall distance of the damping function. $S(x)$ is a smooth step function rising from zero for negative x to one for $x \geq 1$. The following form of S has the

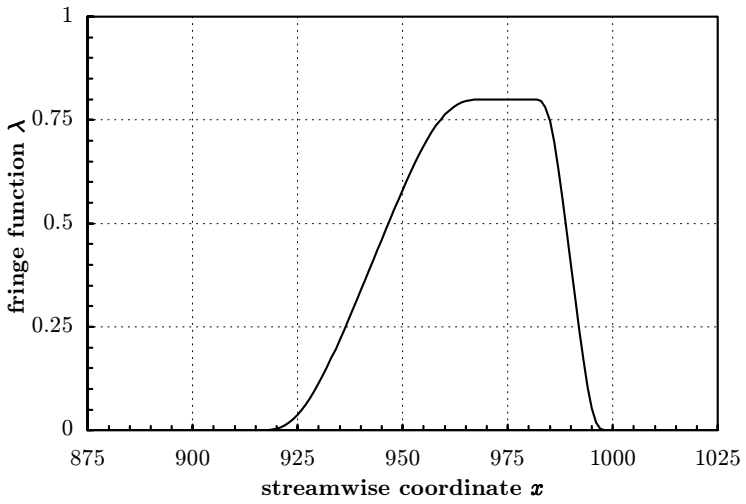

FIGURE 3.2: Fringe function used in the simulations according to equation (3.21). Parameters are $\lambda_{\max} = 0.8$, $x_{\text{start}} = 910$, $x_{\text{end}} = 1000$, $\Delta_{\text{rise}} = 65$ and $\Delta_{\text{fall}} = 20$

advantage of having continuous derivatives of all orders (see figure 3.3)

$$S(x) \quad = \quad \begin{cases} 0 & x \leq 0 \\ 1/[1 + \exp(\frac{1}{x-1} + \frac{1}{x})] & 0 < x < 1 \\ 1 & x \geq 1 \end{cases} \tag{3.22}$$

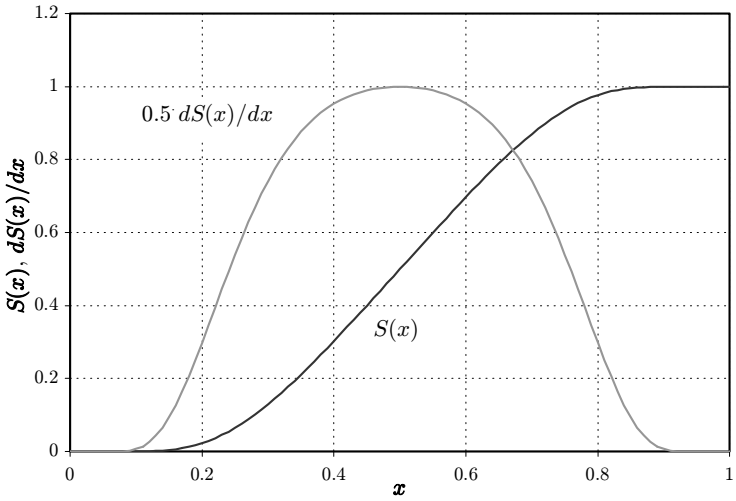

FIGURE 3.3: Smooth step function $S(x)$ (equation (3.22)) together with the derivative. $S(x)$ is used in the fringe function (3.21).

An investigation of how the fringe parameters should be chosen to damp out disturbances in the fringe can be found in [18]. The parameters used for the simulations in this study are given in the caption to figure 3.2.

3.3 Forcing of Continuous Modes

The disturbances, that need to be included at the inlet of the numerical domain, are derived in section 2.3. Formally, they can be written as a sum of different eigensolutions $\tilde{u}_i(y, \alpha, \beta, \omega)$ multiplied by an oscillatory exponential function (see equation 2.71, here rewritten with $u_i^{\text{dist}}(x, y, z, t)$)

$$u_i^{\text{dist}}(x, y, z, t) = \sum_{\alpha} \sum_{\beta} \sum_{\omega} \Phi(\alpha, \beta, \omega) \tilde{u}_i(y, \alpha, \beta, \omega) e^{i(\alpha x + \beta z - \omega t)}. \tag{3.23}$$

Φ denotes a scaling factor for each individual eigenfunction which is used to get a specific energy spectrum (see chapter 2.3.2).

With the numerical scheme used in this report, disturbances are introduced as an additional force in the fringe region (see section 3.2.3). Since the fringe region describes the change between the outflow and the inflow, the disturbances must be specified as they were before the zero x-location – that means that the evaluation of the above sum must be done using negative x values (compare equation (3.20)). The actual forcing (3.19) uses the disturbed base flow $\mathcal{U}_i^{\text{act}}$ which is composed of the base flow $\mathcal{U}_i$ and the disturbances u_i^{dist} from equation (2.71) resp. (3.23)

$$\mathcal{U}_i^{\text{act}}(x, y, z, t) = \mathcal{U}_i(x) + u_i^{\text{dist}}(x, y, z, t). \tag{3.24}$$

The inclusion of the freestream turbulence into the fringe function – especially the evaluation of the exponential in equation (3.23) – demands a considerable proportion of the total computer time per iteration step. For the simulations presented in this thesis, around 30% of the CPU time was needed to perform the calculations for the freestream turbulence (200 eigenmodes).

3.3.1 Corrections

During the development and testing of the inclusion of the continuous modes into the simulation code, a few restriction have been found.

Since the eigenvalue α is a complex number with $\Im(\alpha) > 0$ (stable), the negative x values used for evaluating the fringe forcing term imply an exponential growth of the disturbance upstream. Depending on the numerical value of $\Im(\alpha)$, this growth can be considerable over the fringe length. Since the maximal possible time step is chosen according to the CFL number (3.18), stronger gradients in the fringe region can lead to a decrease of the (adaptive) time step. Eventually, if $\Im(\alpha)$ is large enough for some eigenfunctions included in the sum (3.23), the numerical scheme could breakdown due to numerical exceptions during the execution of the code (too big number to be handled by the double float data type).

To avoid such problems, it was studied how important the inclusion of growing eigenfunction is in terms of the turbulence characteristics at the inlet. Figure 3.4 shows a diagram of the decay of the turbulence intensity Tu. In one case, the turbulence was created using equation (3.23) with exponentially growing eigenfunctions in x. The other case was computed using an adapted equation

$$u_i^{\text{dist}}(x, y, z, t) = \sum_{\alpha} \sum_{\beta} \sum_{\omega} \Phi(\alpha, \beta, \omega) \tilde{u}_i(y, \alpha, \beta, \omega) e^{i(\Re(\alpha) x + \beta z - \omega t)}, \tag{3.25}$$

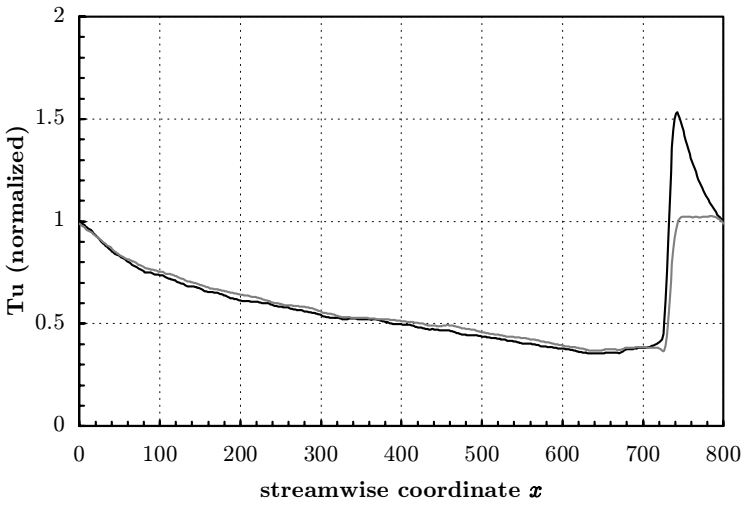

FIGURE 3.4: Normalized decay of the turbulence intensity Tu either with accounting for the exponential grow within the fringe region (black) or with limiting the eigenmode intensity in the fringe region (grey).

where only the oscillatory dependence on α was considered (neglecting of the exponential growth with $\Im(\alpha)$). The average time step in the latter case was around 30% higher than using equation (3.23). As there were no significant differences in the turbulence characteristics at the inlet $x = 0$, it was decided to use the adapted form (3.25) for the simulations.

The second problem is concerned with the boundary condition at the top of the computational domain. The inclusion of the freestream turbulence into the flow domain was found to cause numerical instabilities near the top boundary, manifesting themselves as very high normal velocity through the upper boundary. This could eventually lead to a crash of the iteration. These instabilities seem to be dependent on the turbulence level of the freestream intensity.

Without further enquiries in the cause of these instabilities, a technique to circumvent this problem was devised by damping out the freestream turbulence above a certain height y_{blend}. For every eigenmode included in the sum (3.23) resp. (3.25), $\tilde{v}$ and $\tilde{\eta}$ are blended with the smooth step function $S(x)$ (3.22) according to

$$\tilde{\eta}(y)_{\text{blend}} = \tilde{\eta}(y) \cdot S(y^*) \tag{3.26}$$

$$\tilde{v}(y)_{\text{blend}} = \tilde{v}(y) \cdot S(y^*) \tag{3.27}$$

$$\mathcal{D}\tilde{v}(y)_{\text{blend}} = \mathcal{D}\tilde{v}(y) \cdot S(y^*) + \tilde{v}(y) \cdot \mathcal{D}S(y^*) \tag{3.28}$$

$$\text{with} \qquad y^* = 1 - \frac{y - y_{\text{blend}}}{y_L - y_{\text{blend}}}. \tag{3.29}$$

The other velocity components $\tilde{u}$, $\tilde{w}$ are computed from $\tilde{v}_{\text{blend}}$ and $\tilde{\eta}_{\text{blend}}$ using equation (2.18) and (2.19) as explained in chapter 2. Usually, the start of the blending y_{blend} was chosen 2/3 of the total height y_L.

Chapter 4

Validation

4.1 Numerical Scheme

The numerical scheme and the implementation as presented in chapter 3 and in [18] has already been used in a number of studies, for example [5] and [25]. Therefore, no further validation of the numerical code has been conducted. A study concerning the efficiency of the code and the usage on different types of vector and parallel supercomputers is given in [25].

4.2 Continuous Modes

The superposition of the continuous modes in the fringe region described in section 3.2.3 was tested with a number of different Orr-Sommerfeld / Squire eigenmodes passing through the flow domain. All simulations were performed in a growing boundary layer starting with a Reynolds number based on the inlet displacement thickness $\mathrm{Re}_{\delta_0^*} = 300$. The spatial coordinates in the figures of this chapter are all scaled with δ_0^*. The spectral energy is averaged in the normal direction y and normalized to total energy one.

4.2.1 Full Mode

The first test case studies the convection of a full Orr-Sommerfeld / Squire mode according to (2.20) with the streamwise wavenumber $\beta \neq 0$. The results are given in figures 4.1 to 4.4. The parameters of the eigenmode are given in the caption to figure 4.1.

As it can be seen from equation (2.20), a full Orr-Sommerfeld / Squire mode is exciting all velocity components u, v and w with different strength. The streamwise decay of an eigenmode can be calculated using the linear stability theory introduced in chapter 2. There, the different eigenmodes are described with the wavelike formulation given in equation (2.11). Since the eigenvalue α is a complex number, $\Im(\alpha)$ describes an exponential variation of the eigenmode over x. $\Im(\alpha) > 0$ indicates a decay of the eigenmode with increasing x (stable mode).

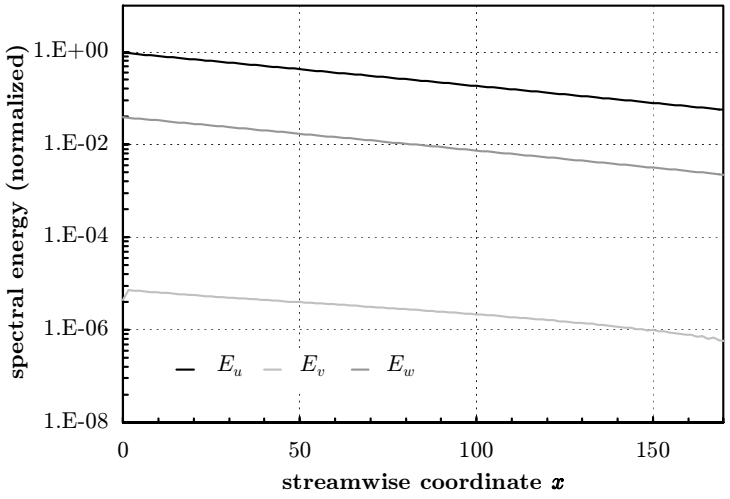

FIGURE 4.1: Convection of a full Orr-Sommerfeld / Squire eigenmode with $\alpha = 0.2 + 0.0080i$, $\beta = 1$, $\omega = 0.2$. Diagram shows the decay of the normalized spectral energy in all velocity components. Normalized to unit total energy at $x = 0$.

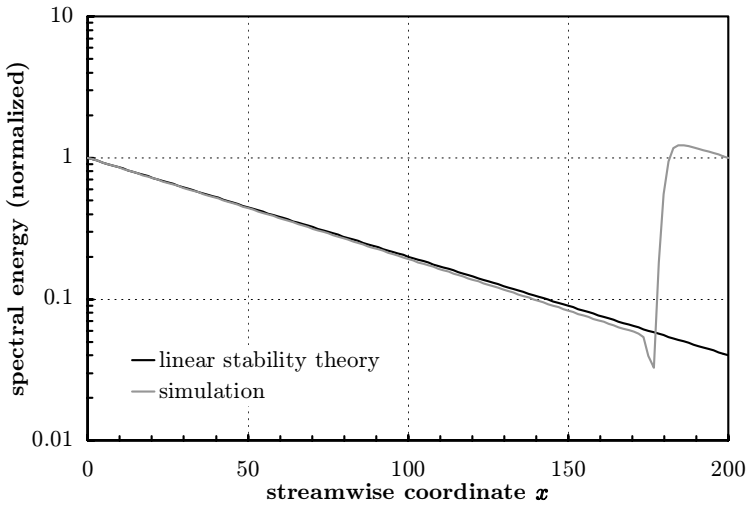

FIGURE 4.2: Decay of the total spectral energy of the full mode (see figure 4.1), shown with the fringe region (starting at $x = 170$). The dashed line represents the decay rate of the linear stability theory $e^{-2\Im(\alpha)x}$.

The energy of a mode is proportional to the square of the velocity. The spatial dependence of the energy is thus

$$E \propto e^{-2\Im(\alpha)x}. \tag{4.1}$$

Therefore, the decay rate of the total energy and the energy of every velocity component on its own should – according to linear stability – follow the decay law (4.1), if the introduced disturbance is an effective solution to the coupled Orr-Sommerfeld / Squire equation.

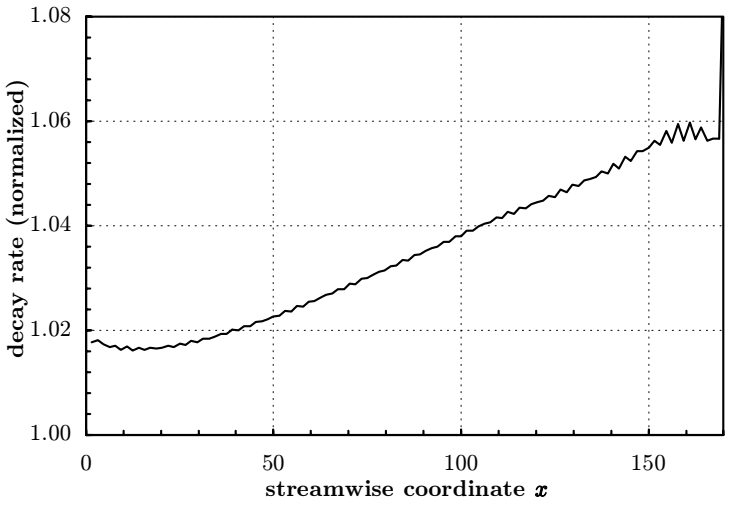

FIGURE 4.3: Ratio of the measured spectral decay rate of the full eigenmode (see figure 4.1) and the solution to the linear stability theory $\Im(\alpha)$.

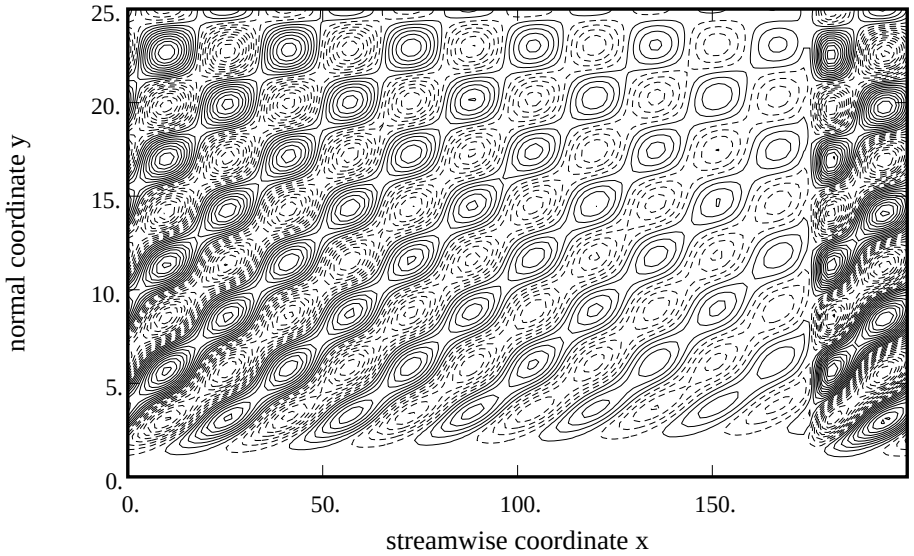

FIGURE 4.4: Contourplot of the velocity field with the full Orr-Sommerfeld / Squire eigenmode (parameters see figure 4.1, shown with the fringe region starting at $x = 170$). The spanwise velocity component w is plotted.

For the test case studying the convection of a full Orr-Sommerfeld / Squire eigenmode, the above conditions are satisfied. The results of the simulations show exactly the predicted decay, qualitatively and quantitatively for all velocity components (figure 4.1) and for the total spectral energy (figures 4.2 and 4.3). The discrepancy between the simulation and the predicted theoretical decay rate is mainly below 5%. The main reason for this discrepancy is the influence of the growing boundary layer near the wall, since the spectral energy is averaged in the

normal direction y.[1]

Figure 4.4 shows a visualization of the spanwise velocity component w in a x/y plane. It can easily be observed, that the disturbance is damped as the spatial coordinate x increases. As pointed out in section 2.1.1, the eigenfunction shows a sinusoidal oscillation in the freestream, whereas the disturbance is practically zero in the region near to the wall.

4.2.2 Orr-Sommerfeld Mode

An Orr-Sommerfeld mode is calculated as a solution to the Orr-Sommerfeld equation (2.13) with explicitly setting $\eta = 0$. Generally, it will consist of fluctuations in all velocity components u, v and w (2.22). But, in contrast to the coupled Orr-Sommerfeld / Squire equations described in (2.20), the Orr-Sommerfeld equation alone does not – in the general ($\beta \neq 0$) oblique case – provide a complete physical solution for the downstream evolution of a disturbance. That is, because there is vorticity η present in the flow but it is suppressed by the calculation of the initial disturbance. Therefore, unlike the results presented for the full mode in figure 4.1, it is expected that the shape of the introduced Orr-Sommerfeld mode will change in the streamwise direction because of interactions within the flow (influence of the Squire equation, production of η). Figure 4.5 shows exactly this behaviour; whereas the decay of v (not directly influenced by the Squire equation) is basically following the decay law (4.1), the behaviour of the w and especially u component differs from the exponential decay.

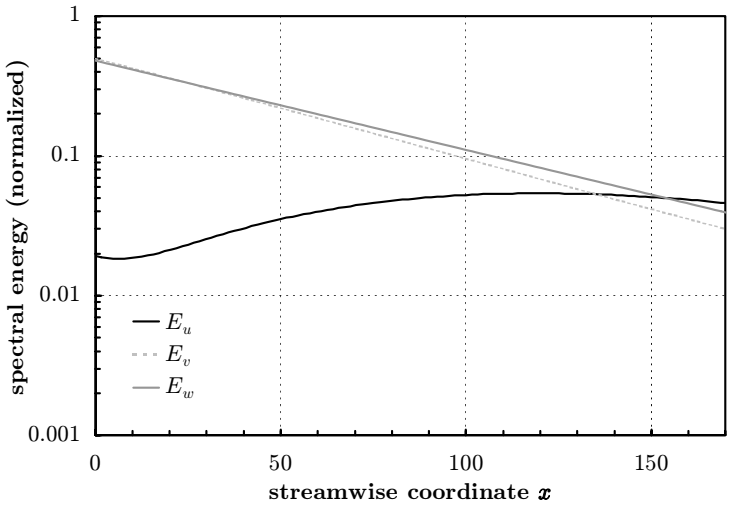

FIGURE 4.5: Convection of an Orr-Sommerfeld eigenmode with $\alpha = 0.2 + 0.0076i$, $\beta = 1$, $\omega = 0.2$ and η explicitly set to zero. Diagram shows the decay of the normalized spectral energy in all velocity components.

[1] Simulations comparing the decay rate to the linear stability theory performed in parallel boundary layers (temporal simulation) usually reach higher accuracy (difference below 0.1%)

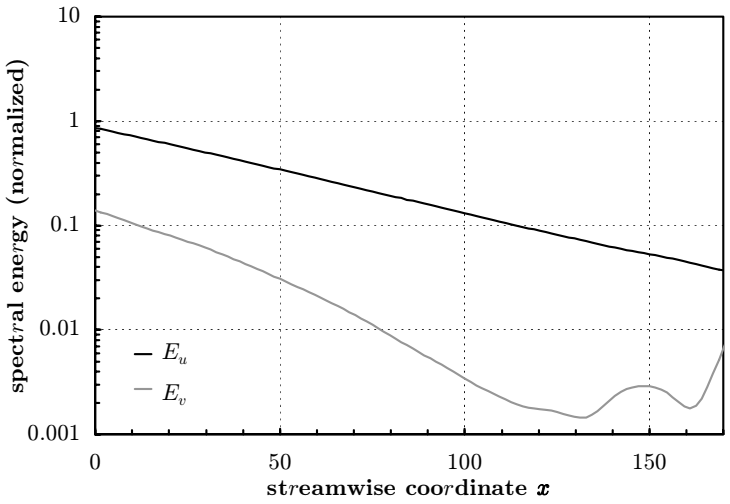

FIGURE 4.6: Convection of an Orr-Sommerfeld eigenmode with $\alpha = 0.2 + 0.0086i$, $\beta = 0$, $\omega = 0.2$. Diagram shows the decay of the normalized spectral energy in all velocity components.

Considering a two-dimensional Orr-Sommerfeld mode (that means $\beta = 0$), the Orr-Sommerfeld equation alone governs the fluctuations in u and v (see (2.21)). The influence of the (now uncoupled) Squire equation is restricted to w, which stays – if not forced – zero. Therefore, the energy decay of the different velocity components is expected to resemble figure 4.1 with $E_w = 0$. Qualitatively, the theoretical behaviour is confirmed in figure 4.6, showing nearly exponential decay for both the u and v velocity, whereas w stays zero. The disturbance is thus two-dimensional throughout the whole flow domain.

4.2.3 Squire Mode

The third test case is the convection of a Squire mode. As described above and in (2.23), the Squire equation will only govern the u and w velocity components. In a general three-dimensional case it will not be a physical solution the to downstream evolution of disturbances. However, in the case of a two-dimensional wave ($\beta = 0$), the Squire equation alone provides a complete solution for only the w component, whereas u and v should remain zero if not forced.

Figure 4.7 shows basically the theoretically indicated behaviour for the simulation: The energy in w is following the decay law (4.1). However, u and v is generated while the disturbance travels downstream; this is mainly due to nonlinear interactions which are not captured in the linear-stability equations.

4.2.4 Two Modes

The freestream turbulence introduced into the flow is composed of a number of different eigenmodes to the Orr-Sommerfeld and Squire equation (see section 2.3). Therefore it seemed interesting to examine the downstream convection of two

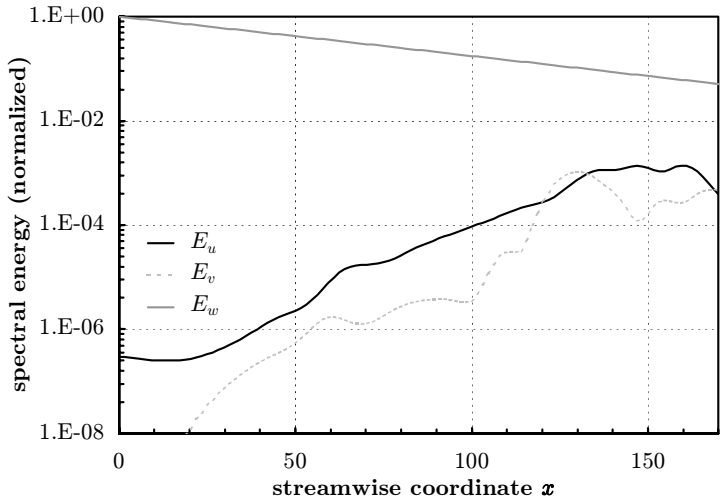

FIGURE 4.7: Convection of a Squire eigenmode with $\alpha = 0.2 + 0.0085i$, $\beta = 0$, $\omega = 0.2$. Diagram shows the decay of the normalized spectral energy in all velocity components.

superimposed eigenmodes. By choosing two full Orr-Sommerfeld / Squire modes, the decay of the total energy in both modes should follow the exponential decay (4.1) of the linear stability. It is shown in figure 4.8, that the theoretical decay is confirmed by the simulation.

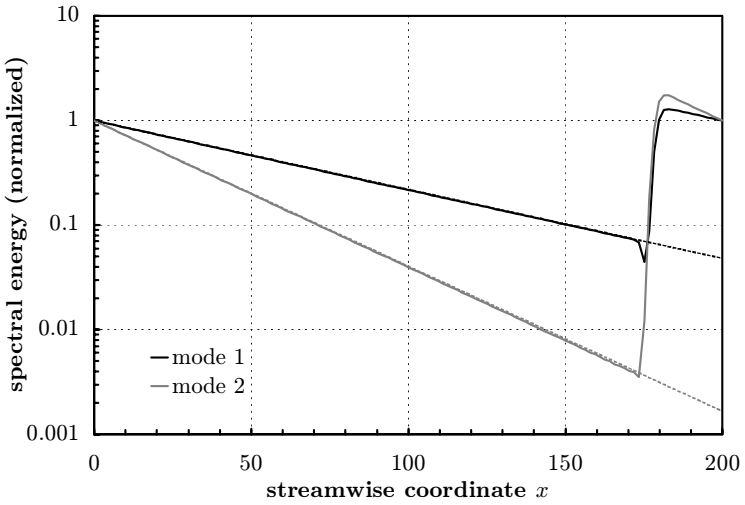

FIGURE 4.8: Convection of two eigenmodes through the computational domain, shown with the fringe region (starting at $x = 170$). First mode: $\alpha = 0.2 + 0.0076i$, $\beta = 1$, $\omega = 0.2$. Second mode: $\alpha = 0.4 + 0.0160i$, $\beta = 2$, $\omega = 0.4$. Dashed line represents decay rate of the linear stability theory $e^{-2\Im(\alpha)x}$.

Figure 4.9 finally shows a visualization of the w velocity component in a x/z plane.

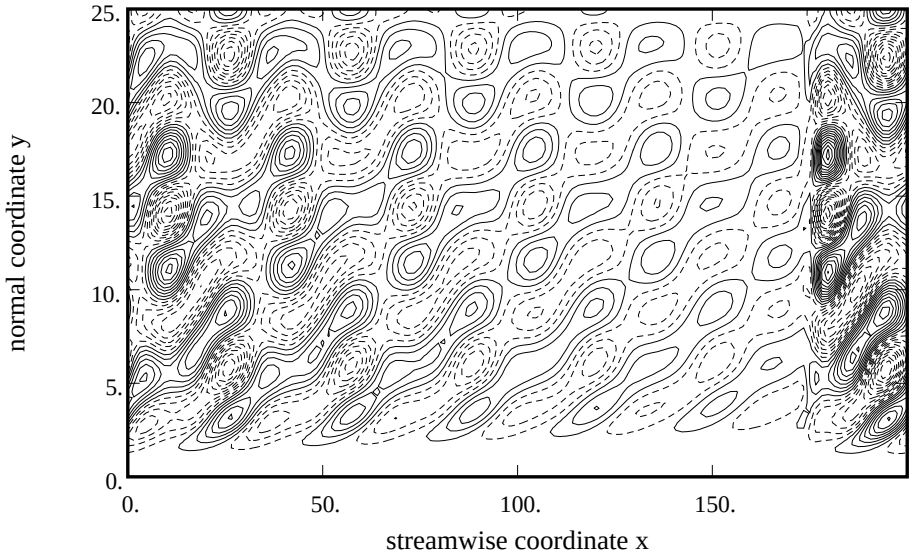

FIGURE 4.9: Contourplot of the velocity field with two propagating eigenmodes (parameters see figure 4.8, shown with the fringe region starting at $x = 170$). The spanwise velocity component w is plotted.

Chapter 5

Results

In this chapter, the results of the direct numerical simulation are presented. References to other simulation as well as experimental data will be given throughout the text.

5.1 Simulation Parameters

One major simulation which eventually reached transition was conducted for this thesis. The parameters for this case are presented in table 5.1. These parameters

turbulence intensity Tu at inlet	4.7%
$\mathrm{Re}_{\delta_0^*}$ at inlet ($x = 0$)	300
Re_{x_0} at inlet ($x = 0$)	32400
x_L (with fringe region)	1000
y_L (with blending region)	60
z_L	50
fringe start x_{start}	910
fringe end x_{end}	1000
fringe strength λ_{max}	0.8
Δ_{rise}	65
Δ_{fall}	20
start of blending y_{blend}	40
Number of modes in x N_x	1024
Number of modes in y N_y	121
Number of modes in z N_z	72

TABLE 5.1: Parameters for the main simulation

together with the higher turbulence intensity than in T3A and [16] proved to be sufficient to get turbulent spots and a portion of steady turbulence at the end of the computational domain. It is important to note that the spanwise width of the domain is crucial to trigger laminar streaks to break down into turbulent spots; a simulation with comparable parameters except for $z_l = 30$ instead of $z_L = 50$ showed growing laminar streaks, but lacked their breakdown. An explanation

for this phenomena could be, that due to the narrow domain the streaks are too constraint in their shape, resulting in preventing any instability and eventual breakdown.

Some results are presented depending on different downstream positions. Table 5.2 gives an overview of alternative formulations of these positions.

simulation stations				T3A stations			
x	Re_x	Re_{δ^*}	Re_θ	x	Re_x	Re_{δ^*}	Re_θ
0	32400	300	114	121	68728	445	177
100	62400	420	164	200	92400	532	225
200	92400	532	225	279	116189	610	272
240	104400	573	250	382	146950	686	323
300	122400	629	284	493	180349	737	385
400	153400	696	332	632	221951	769	456
450	167400	720	360	769	262966	818	539
500	182400	740	389	888	299000	918	628
600	212400	765	440				
700	242400	783	493				
800	272400	843	562				
900	302400	923	618				

TABLE 5.2: Various parameters of the different downstream locations used in the presentation of the results. x denotes the nondimensional streamwise coordinate used in the numerical code. Re_x, Re_{δ^*} and Re_θ are the Reynolds numbers based on (dimensional) x, the displacement thickness δ^* and the momentum thickness θ, respectively.

The computation was conducted on a Cray J932se computer using the code `bla` compiled for 12 processors (parallel vector processors with shared memory). The flow field was calculated up to a (nondimensional) time of 5000 with an averaged time step of 0.3. The user time needed for this simulation was roughly 400 hours (4800 CPU hours).

5.1.1 T3 Test Cases

In 1990, the European Research Community On Flow Turbulence And Combustion (ERCOFTAC) set up a database containing experimental and computational studies of several complex test cases. One of these test cases involved transition in boundary layers subject to freestream turbulence for levels above 1% such that bypass transition occurs. The respective case, T3, was experimentally performed 1992 by Coupland [10] and Roach & Brierley [22]. Two different turbulence intensities were studied: Test case T3A with Tu=3% and T3B with Tu=6%. The freestream turbulence was in both cases isotropic and homogeneous.

The data was recorded using both cross-wire probes for the spanwise and normal velocity and single-wire probes for the streamwise velocity. The references made in this thesis all refer to test case T3A, as for that case there are more experimental stations available.

5.2 Freestream Turbulence

As described in section 2.3, the inlet disturbance consists of homogeneous isotropic turbulence. This kind of turbulence can be characterized by the intensity of the velocity fluctuations Tu and an energy spectrum.

For the cases in this thesis, a von Kármán energy spectrum (2.69) with an integral length scale L_I was used (see chapter 2.2.2) as inlet disturbance for the simulations. L_I was chosen as $5\delta_0^*$ similar to the study [16].

5.2.1 Decay of the Energy

Turbulence is a highly dissipative process due to the strong gradients in the velocity components. Therefore, unforced turbulence will decay in time and space from the point where it was created. The decay rate of this loss in kinetic energy is dependent on many influences, examples may be the way the turbulence was created, boundaries in the flow domain etc. An important influence is the integral length scale of the turbulence, that is to say the dimensions of the largest eddies in the flow. It can be shown through simple inviscid estimations that the dissipation ε is proportional to [27]

$$\varepsilon \propto \frac{u_I^3}{L_I} \tag{5.1}$$

with u_I as integral velocity. Therefore, it can be concluded that the smaller the turbulence length scales are the faster it decays. Moreover, it can be shown that with increasing decay of the turbulence the length scale L_I is growing and hereby slowing down the decay process.

Isotropic grid turbulence is thus know to follow a decay law of the form

$$\mathrm{Tu} \propto (x + A)^B. \tag{5.2}$$

The decay rate B is, depending on the source, between 0.5 and 1 [28]. As a further validation of the flow simulation, a least squares fit on the decay of the turbulence intensity was performed (see figure 5.1) yielding a decay rate $B \approx 0.80$. Thus, the decay of the freestream turbulence is sufficiently similar to the grid turbulence decay rate.

A measure for the isotropy of the imposed freestream turbulence is given with comparing the decay rate of the different velocity fluctuations u', v' and w'. Figure 5.2 shows the evolution of the averaged fluctuation intensity u_{rms}, v_{rms} and w_{rms} over the flow domain. Within the main portion of the streamwise extent (up to about $\mathrm{Re}_x \approx 2 \cdot 10^5$), the maximal variance of the rms-values from the turbulence intensity is below 3%.

Another measure for isotropy can be obtained looking at one-dimensional spectra (see below) or by calculating different length scales [15]. The dissipation length scale based on the turbulent kinetic energy is defined as

$$L_k = \frac{k^{3/2}}{\varepsilon} \tag{5.3}$$

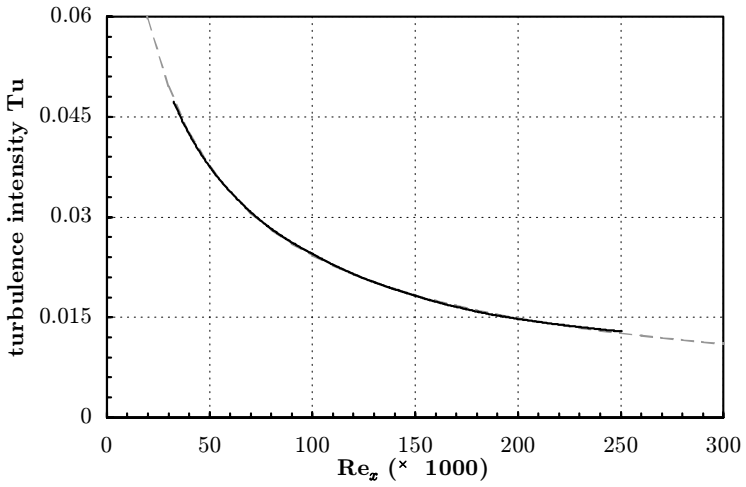

FIGURE 5.1: Decay of the turbulence intensity Tu at $y = 25\delta_0^*$ (solid) and least squares fit to equation (5.2) with $B \approx 0.80$.

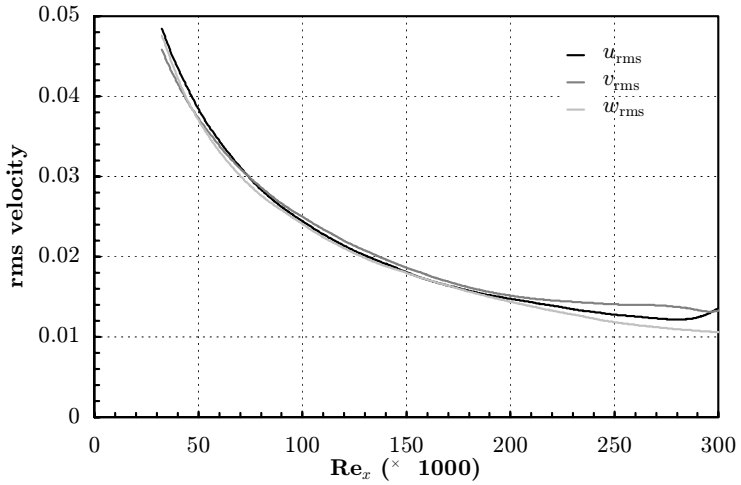

FIGURE 5.2: Comparison of the decay of u_{rms}, v_{rms} and w_{rms} at $y = 25\delta_0^*$.

with ε introduced as the turbulent dissipation. Due to the fact that many experiments only measure the streamwise velocity fluctuations, an alternative definition of the dissipation length scale based on the decay of the streamwise velocity component can be given

$$L_u = \frac{u_{\mathrm{rms}}^3}{\varepsilon_x} \tag{5.4}$$

with ε_x denoting the x-component of the dissipation. For isotropic flow, the ratio L_u/L_k reaches the value of $\sqrt{2/3}$. Figure 5.3 portrays the evolution of this ratio within the flow domain. After a certain inlet length, the ratio is very close to the

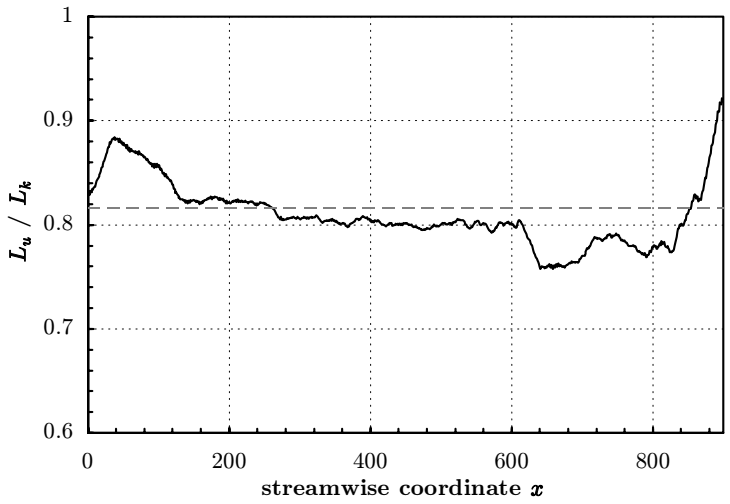

FIGURE 5.3: Ratio L_u/L_k of the dissipation length scale based on the streamwise velocity component L_u and based on the total kinetic energy L_k at $y = 25\delta_0^*$. The dashed line represents the isotropic value $\sqrt{2/3} \approx 0.8165$.

isotropic value, whereas for high streamwise coordinates an increased deviation can be discovered similar to the observation made above for the rms-velocities.

The homogeneity of the imposed disturbances can be checked looking at the energy decay at different y positions within the flow domain. As figure 5.4 shows, the maximal variance of the kinetic energy from the mean value is below 3% throughout the whole vertical extent of the domain (not considering the blending region, $y < y_{\text{blend}}$).

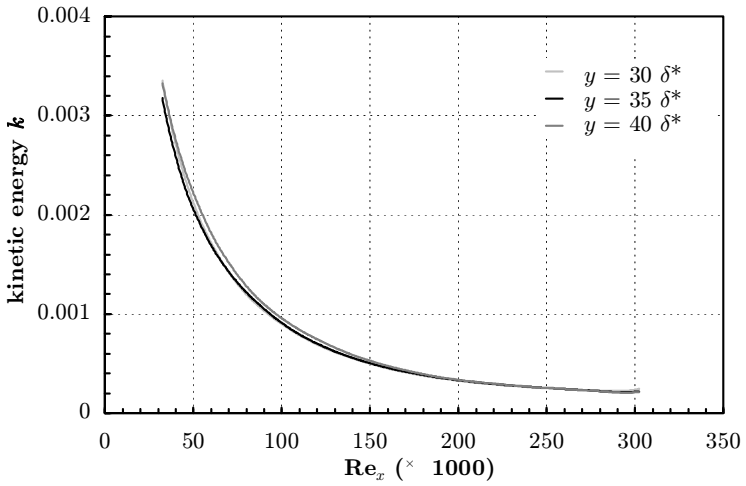

FIGURE 5.4: Decay of the kinetic energy at different y positions.

To summarize the above qualifications of the freestream turbulence, a visu-

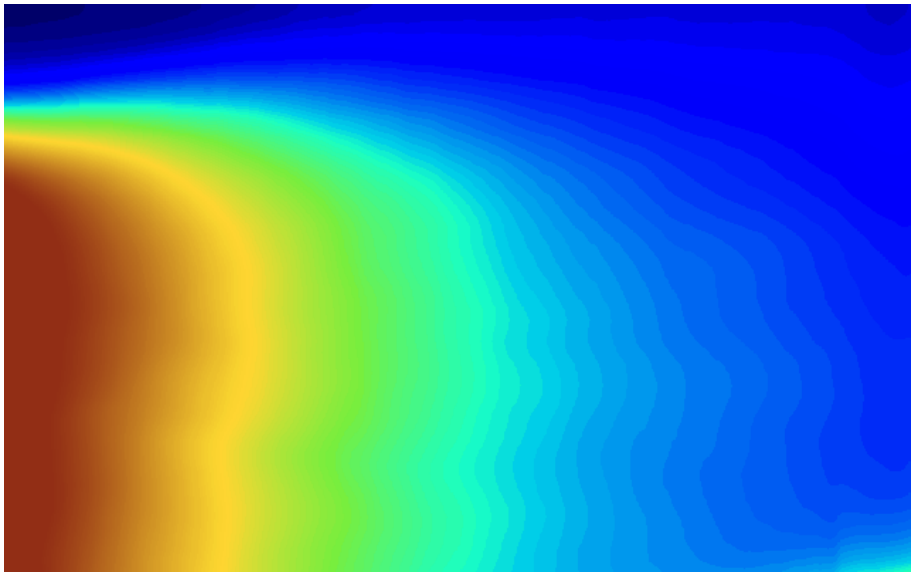

FIGURE 5.5: Visualization of the turbulent kinetic energy k in the upper part of the computational domain averaged in z (and time). Section shown $x = 0..900$ (without fringe region) and $y = 20..60$ (without boundary layer). The blending acting on the eigenfunctions above $y_{\text{blend}} = 40$ is clearly visible.

alization of the turbulent kinetic energy is show in figure 5.5. The decay of the energy in the streamwise direction is clearly visible as well as the effect of the blending above $y_{\text{blend}} = 40$.

5.2.2 Energy Spectra

According to section 2.2.2, one-dimensional and three-dimensional energy spectra are an important means to qualify homogeneous isotropic turbulence. Since the turbulence intensity is decaying in the streamwise direction, the Taylor Hypothesis has been applied to allow the calculation of streamwise spectra. Figure 5.6 shows the comparison of a three-dimensional energy spectrum and the three one-dimensional spectra in the freestream at a certain downstream position. Both, the one-dimensional and three-dimensional spectra resemble the forced spectrum (2.69). Moreover, the isotropy of the flow is affirmed by comparing the three one-dimensional spectra. The deviation of these spectra for high wavenumbers is explained by the fact, that the domain, where the spectrum was calculated on, is only periodic in the z-direction. Both the x and y directions are clipped allowing aliasing errors to disturb the energy content in high wavenumbers. The spectrum for the energy $E_z(k_z)$ shows exactly the experimentally and numerically confirmed shape.

Alternatively, figure 5.7 displays three-dimensional energy spectra at different downstream positions. The spectrum calculated at the inlet position $x = 0$ compares well with the desired spectrum (2.69) (see figure 2.10), whereas the spectra calculated at increased downstream coordinates show, on the one hand, the decay

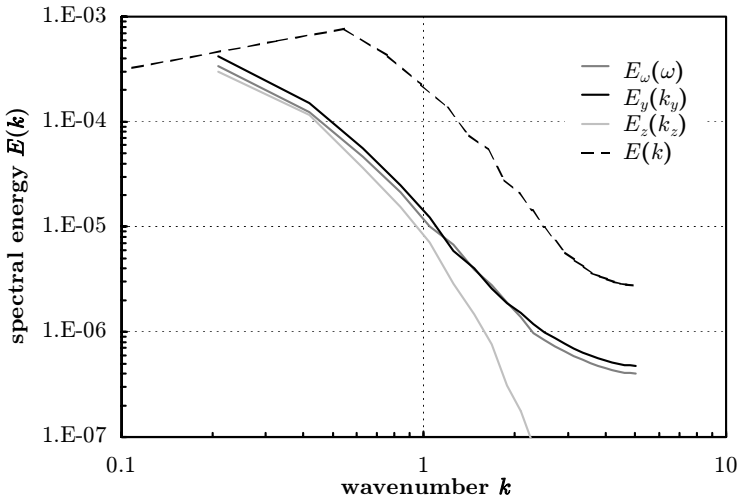

FIGURE 5.6: One-dimensional and three-dimensional energy spectra in the freestream at $x = 240$.

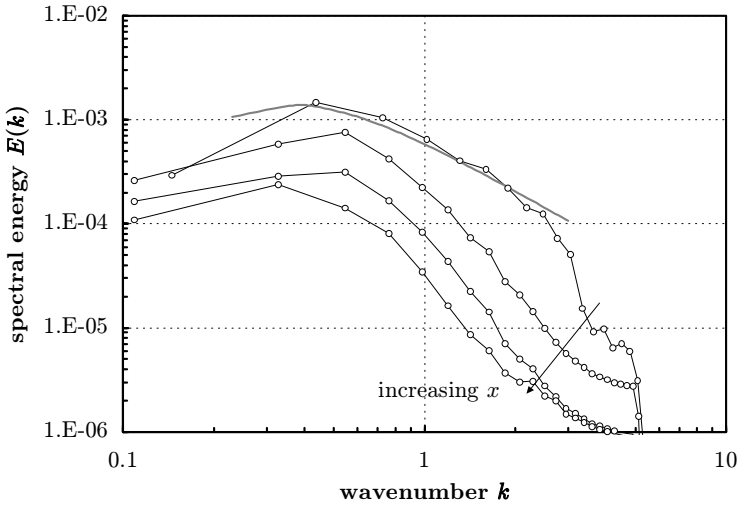

FIGURE 5.7: Downstream evolution of three-dimensional energy spectra at $x = 0$, $x = 240$, $x = 450$ and $x = 900$. The forced spectrum is shown in grey.

of the total kinetic energy (integral of $E(\kappa)$ over κ) and, on the other hand, the slight shift of the intensity maximum to lower wavenumbers. The shape of the spectrum is maintained in all downstream positions.

5.2.3 Comparison

It has been shown with the above mentioned least squares fit, that the simulated turbulence basically follows the decay law given in equation (5.2). But the overall speed of the decay is not stated by the constant B alone, it also depends on A and the proportionality factor. The physical quantity that influences these additional

factors is the integral length scale of the (isotropic and homogeneous) turbulence. Therefore, variations in L_I can lead to a different decay speed, although the decay rate (exponential B in equation (5.2)) is similar.

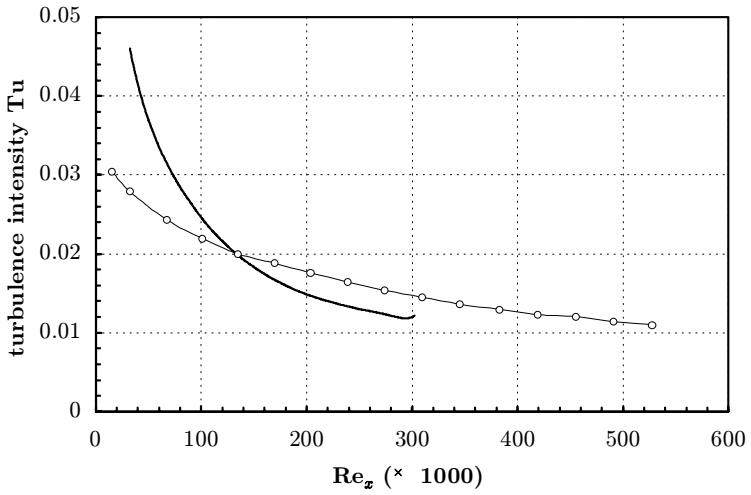

FIGURE 5.8: Comparison of the decay of the turbulence intensity Tu for the simulation and the experimental test case T3A.

The integral parameters chosen for the present simulation are smaller than those generated in the T3A test cases. This is clearly visible in figure 5.8, showing a faster decay of the turbulence for the DNS than for the experiments. On the other hand, the comparison of this simulation to the data given for the DNS in [16] yields similar value for the decay of the turbulence.

This difference in the strength of the turbulence can give rise to the assumption that due to the weaker forcing of the boundary layer transition would occur at a later stage. On the other hand, rapid distortion theory [15] claims that smaller scales are more effective at influencing boundary layers and would therefore lead to an earlier onset of the transitional process.

The results herein and in [16] show that good agreement with the experimental data can be achieved despite this difference in the initial conditions.

5.3 Averaged Results

In this section, some of the averaged results obtained by the numerical simulation are discussed and compared to the experimental case T3A and to the study [19]. All quantities are statistically averaged in time over a non-dimensional time span of 2500 units. Statistics were taken beginning with 2500 time units after the start of the simulation. It was checked whether the inclusion of more statistics would change the results.

The present simulation was computed with a freestream turbulence intensity of approximately 4.7 %. Since the experimental findings were taken with Tu=3-3.5%, a direct comparison of the data in dependence of the downstream and normal location is difficult. Therefore, an appropriate scaling has to be applied. Normally, downstream locations are indicated using the non-dimensional Reynolds number Re_x based on the downstream location x (in dimensional form). This scaling would not take into account the different initial conditions. Another way to characterize a downstream position is given by a Reynolds number based on boundary layer units, for example Re_θ based on the local momentum thickness or Re_{δ^*} based on the displacement thickness. The advantage of such a scaling is that the present shape of the boundary layer rather than the physical downstream location is used. Hereby, similar states of the boundary layer can be compared, even though the initial conditions of the respective case were quite different.

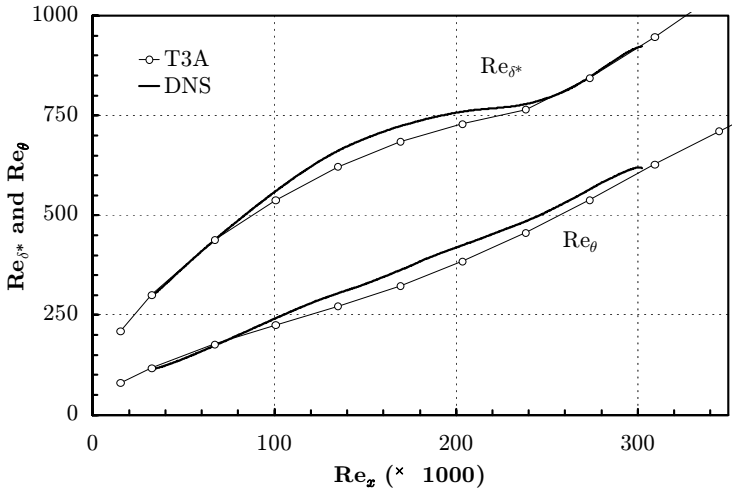

FIGURE 5.9: Reynolds number Re_{δ^*} based on the local displacement thickness, Re_θ based on the momentum thickness and Re_x based on the downstream location for the simulation and T3A.

Figure 5.9 shows the relation between the different Reynolds numbers for both the simulation and the T3A case. It can be seen that the relation between Re_x and the Reynolds number based on boundary layer units is non-linear. The difference between the simulation and the experiment is due to the different turbulence intensity. The simulation shows a higher boundary layer thickness at the same

downstream location than the experiment. This indicates an earlier onset of transition for the DNS, which is evident due to the higher turbulence intensity.

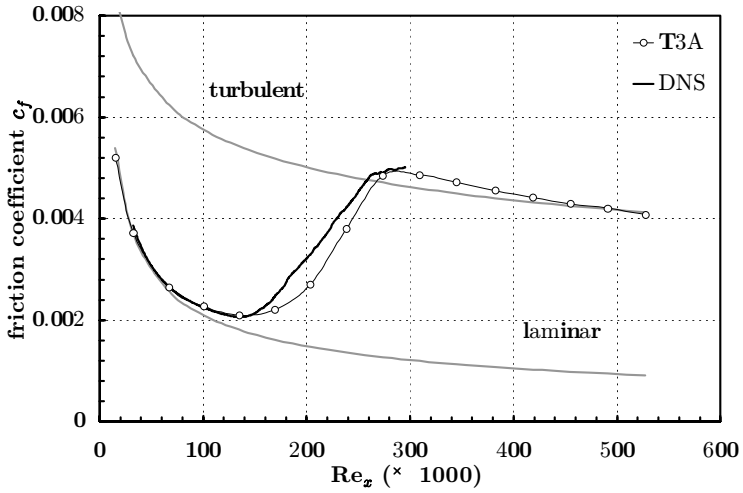

FIGURE 5.10: Friction coefficient c_f versus Re_x for simulation and T3A.

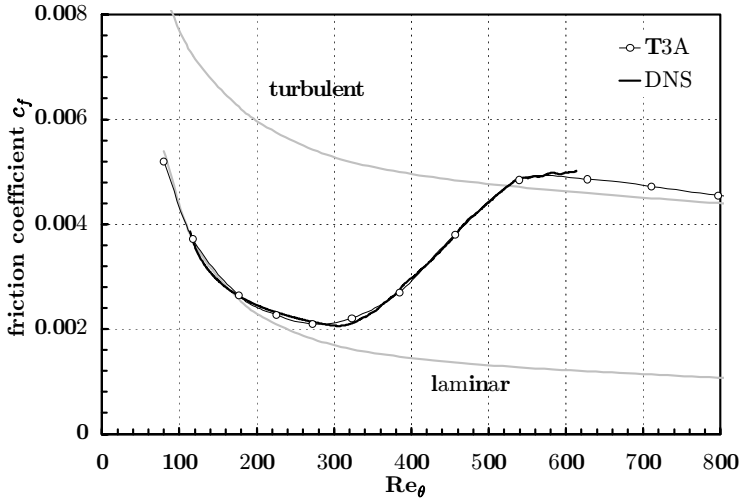

FIGURE 5.11: Friction coefficient c_f versus Re_θ for simulation and T3A.

The importance of an appropriate scaling of the variables is demonstrated in the figures 5.10 and 5.11, both showing the local skin friction coefficient c_f (see Appendix A.3). The skin friction correlation for laminar and turbulent flow is included for reference. The difference between the scaling with Re_x and Re_θ is obvious (see above). For the boundary layer scaling, the simulation collapses astonishingly well on the experimental data, whereas for the physical scaling the transition to turbulence occurs – as to be expected – earlier than in the experiments.

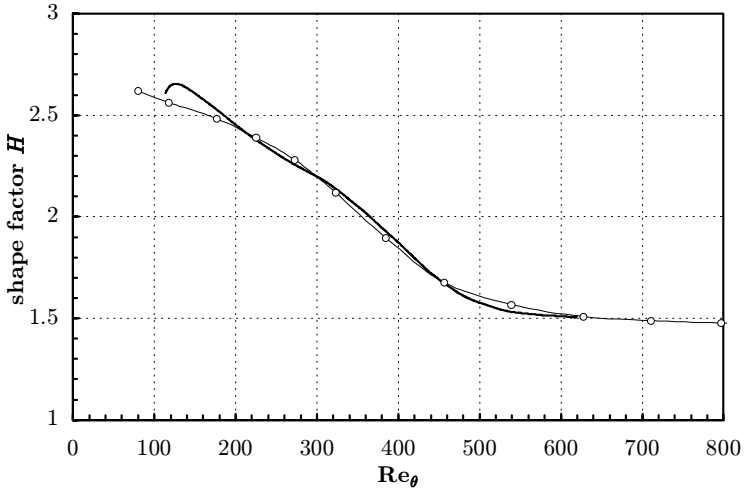

FIGURE 5.12: Shape factor H versus Re_θ for the simulation (thick line) and the experimental case T3A (symbols).

The shape factor $H = \delta^*/\theta$ (see appendix) provides distinct values for either laminar and turbulent flow. Therefore, it is a good measure for the onset of transition and the general structure of the boundary layer. The downstream variation of H is shown in figure 5.12. The difference between the computed and experimental data is – except for a region close to the inlet – minimal. Moreover, the same stationary value of H is approached in both the simulation and the experiment, giving good evidence that the structure of the boundary layer is well captured in the numerical simulation. The discrepancy at the inlet can be explained by the fact that the inflow of the simulation is assumed to be a Blasius profile with superposed freestream turbulence whereas in the experiments, already some rearrangements in the boundary layer structure have taken place. Again, a scaling based on the momentum thickness θ has been used to allow direct comparison with the experiments.

Figure 5.13 shows the mean streamwise velocity profile $u^+(y^+)$ in wall units for several downstream locations Re_θ. There are only minor differences between the experimental test case T3A and the simulation. Moreover, the velocity profile at the most downstream location Re_θ=539 shows a good approaching to the classical linear and logarithmic wall law approximated by Spalding's formula (A.21). Fully developed turbulence and with that better collapse on the wall law could be expected above $\mathrm{Re}_\theta \approx$1000.

An overview of the energy distribution within the boundary layer can be found in figure 5.14 (compare to figure 5.5 which shows the upper part of the computational domain). The boundary layer thickness $\delta_{99\%}$ coincides roughly with the edge region optically apparent in the figure. The figure qualitatively illustrates most of the inherent features of the laminar-turbulent transition. The decay of the freestream turbulence is clearly visible in the upper part of the image. In the boundary layer, the streak formation and growth is apparent as an increase of the

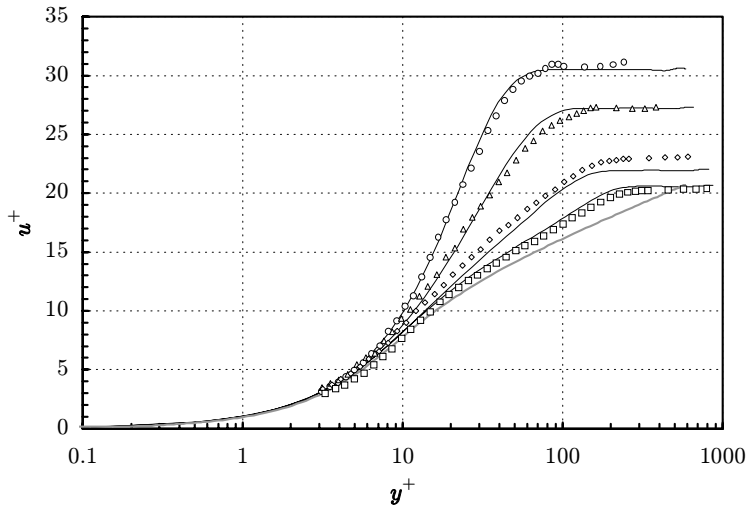

FIGURE 5.13: Mean streamwise velocity profile $u^+(y^+)$ in wall scaling for various downstream positions (∘ Re_θ=272; △ Re_θ=385; ◇ Re_θ=457; □ Re_θ=539) compared for simulation (black line), T3A (symbols) and Spalding's logarithmic law (grey, see appendix (A.21)).

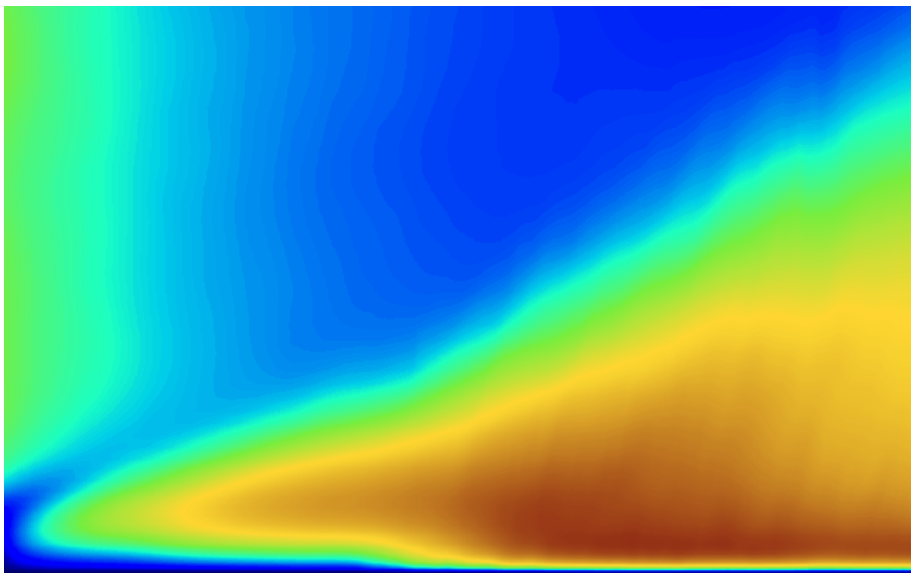

FIGURE 5.14: Visualization of the kinetic energy k in the boundary layer. Section shown $x = 0 - 900$, $y = 0 - 20$ (without fringe region, for upper part of the computational domain refer to figure 5.14). Energy intensity ranges from blue/white (weak, Tu=0%) to red/black (strong, Tu=14%).

kinetic energy peaking at half of the boundary layer thickness $\delta_{99\%}/2$. As soon as turbulent spots are present in the flow, the streamwise growth of the energy slows down and the intensity maximum shifts downwards closer to the wall. At the same time, the boundary layer begins to grow faster than in the laminar case.

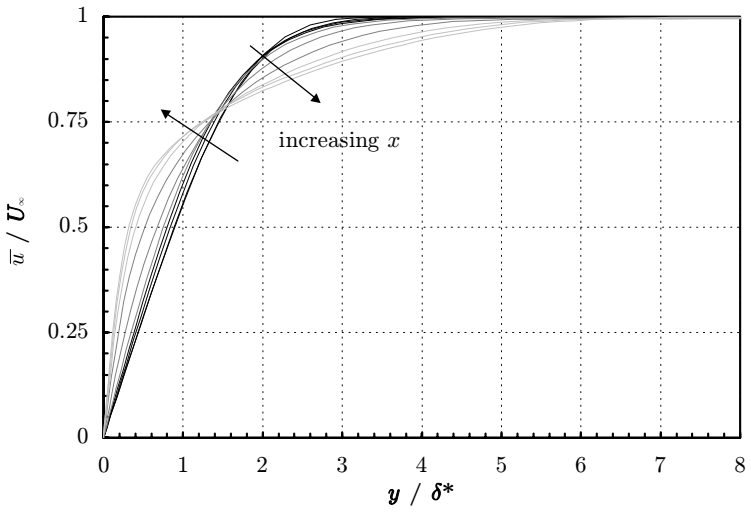

FIGURE 5.15: Evolution of the mean velocity profile $\overline{u}$ for various x locations. Black lines: $x = 100$, $x = 200$, $x = 300$; dark grey lines: $x = 400$, $x = 500$, $x = 600$; light grey lines: $x = 700$, $x = 800$, $x = 900$ (see table 5.2 for the respective Re_x and Re_θ).

The downstream variation of the mean velocity profile $\overline{u}$ is shown in figure 5.15. Starting at the inlet $x = 0$ with a Blasius profile (see appendix A.2), fluid with higher velocity is increasingly found closer to the wall according to the transition from laminar to turbulent. The higher velocity within the inner half of the boundary layer will lead to higher velocity gradients and thus increase the local skin friction. Qualitatively and quantitatively, this result is comparable to the experimental findings in the T3A test case [10] and in [19]. Furthermore, the numerical study [16] yielded similar results.

Figures 5.16 and 5.17 show the deviation of the mean velocity profile from the local Blasius boundary layer profile. Again, one observes an increased velocity in the inner half of the boundary layer and a decrease in the outer half expressing the onset of transition. In figure 5.16 the wall normal coordinate y is scaled with the inlet momentum thickness δ_0^*. With that scaling, the deviation peak in the inner half seems to collapse at a fixed (physical) distance from the wall. On the other hand, figure 5.17 scaled with the local momentum thickness δ^* indicates an accumulation of the peak in the outer half at around 2.4 times the local momentum thickness δ^*. In contrast to these findings, a similar plot is presented in [19] showing a good collapse for both peaks scaled with the local boundary layer units (nearly self-similar development).

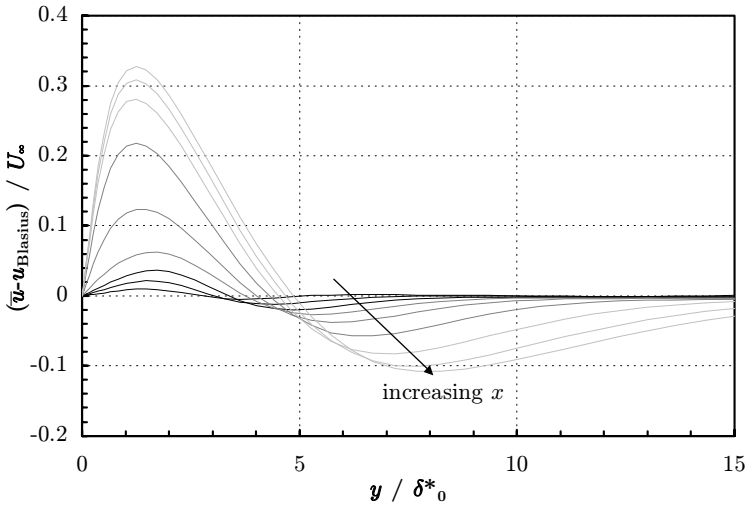

FIGURE 5.16: Deviation of the averaged streamwise velocity $\overline{u}$ and the local Blasius velocity profile for the respective x-position as a function of the inflow displacement thickness δ_0^*. Black lines: $x = 100$, $x = 200$, $x = 300$; dark grey lines: $x = 400$, $x = 500$, $x = 600$; light grey lines: $x = 700$, $x = 800$, $x = 900$.

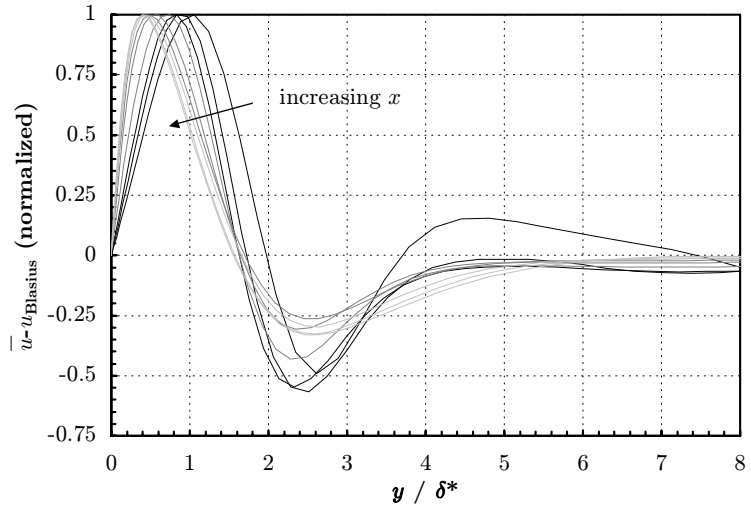

FIGURE 5.17: Normalized deviation of the averaged streamwise velocity $\overline{u}$ and the local Blasius velocity profile for the respective x-position as a function of the local displacement thickness δ^*. The x-locations are the same as in figure 5.16.

5.4 Streaks and Spots

Unlike the traditional approach to boundary layer stability with exponential growth of Tollmien-Schlichting waves, larger levels of freestream turbulence (Tu$\gtrsim$ 1%) provoke a different transition scenario. Rather than exponential an algebraic (linear) growth mechanism is acting on the streamwise velocity component. For detailed explanation refer to section 1.1.

The *lift-up effect* described by Landahl [17] explains how growing elongated structures in the streamwise velocity component become apparent within the boundary layer, so called streaks. The streak growth is mainly due to the formation of normal vorticity η, which is triggered by freestream disturbances penetrating the boundary layer (recent theoretical investigations see [7] and [6]).

Although the lift-up effect is basically inviscid, the same mechanism is acting on viscous flows as well [14]. Moreover, spanwise scales of the streaks can be approximated using the concept of optimal disturbances which is developed in [3].

Streaks are still a phenomena of laminar flow, nevertheless they play an important role in the laminar-turbulent breakdown [28], [16]. Before their breakdown, streaks can reach a high strength of up to fifteen percent of the freestream velocity. The exact way, how these streaky structures finally break down to turbulence is still not fully understood [2] – several theories and scenarios exist, which will be further discussed in section 5.4.2. An overview of the turbulent statistical quantities and qualifications of the streaks are given in the next section.

5.4.1 Streaks

The appearance of streaky structures in the boundary layer is observable in both the statistical analysis and the instantaneous visualization of the velocity fluctuations. As described in the preceding chapter, these streaks manifest themselves as elongated structures in the streamwise direction with alternating in the spanwise direction between high and low speed. Therefore, a distinctive influence can be observed in the fluctuation of the streamwise velocity u_{rms}. Instantaneous visualizations of streaks can be found for example in figure 5.27.

Figure 5.18 shows the variation of u_{rms} for different downstream positions. The presence of streaky structures increases the rms-value at the y coordinates where they are most distinct. During the first phase of the streak growth, the wall-normal position of the peak value for different x-positions scales nicely with the local displacement thickness yielding $y_{\max} \approx 1.4\delta^*$, whereas above a certain level a considerable change in the shape of u_{rms} occurs: The fluctuation maximum moves closer to the wall and even decreases (see also figure 5.21). This behaviour has been observed in most of the other studies including [16], [10] and [19]. A good qualitative and quantitative agreement between these cases and the present study was obtained.

The behaviour of the velocity fluctuations in the other directions is similar, although it is not as distinct as in the streamwise component (figures 5.19 and 5.20). For both v_{rms} and w_{rms}, the peak at roughly half of the local boundary layer thickness is increasing, and after a certain downstream position, moving

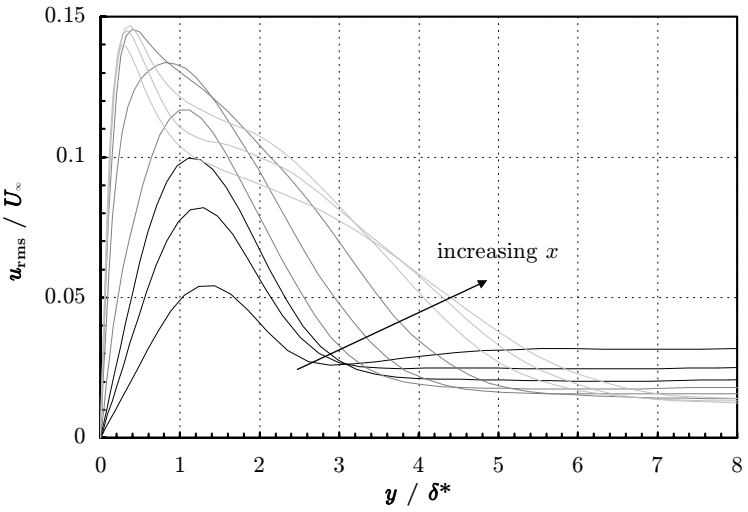

FIGURE 5.18: u_{rms} for various downstream locations. Black lines: $x = 100$, $x = 200$, $x = 300$; dark grey lines: $x = 400$, $x = 500$, $x = 600$; light grey lines: $x = 700$, $x = 800$, $x = 900$.

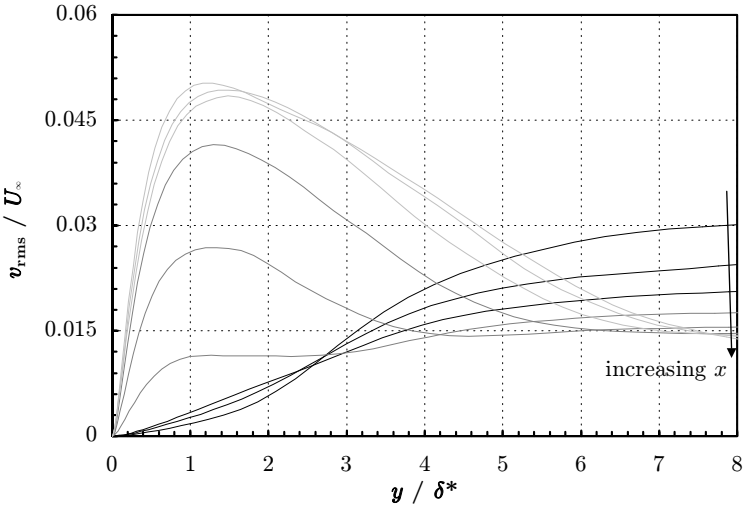

FIGURE 5.19: v_{rms} for the same downstream locations as in figure 5.18.

closer to the wall and eventually decreasing again. This is also similar to the other experimental and numerical results quoted above.

Closely related to figure 5.18 is figure 5.21 showing the streamwise evolution of the maximum streamwise fluctuation energy $u^2_{\mathrm{rms,max}}$ and the respective y coordinate. It shows clearly, that during the initial phase the growth in $u^2_{\mathrm{rms,max}}$ is linear with x indicating a linear energy growth. Thereafter it saturates and decreases again a little bit. The position of the maximal u-fluctuation is in the first phase between $1.4\delta^*$ and $1.1\delta^*$ and afterwards decreases considerably to around the expected value for fully turbulent boundary layers of $15y^+$. The results presented in

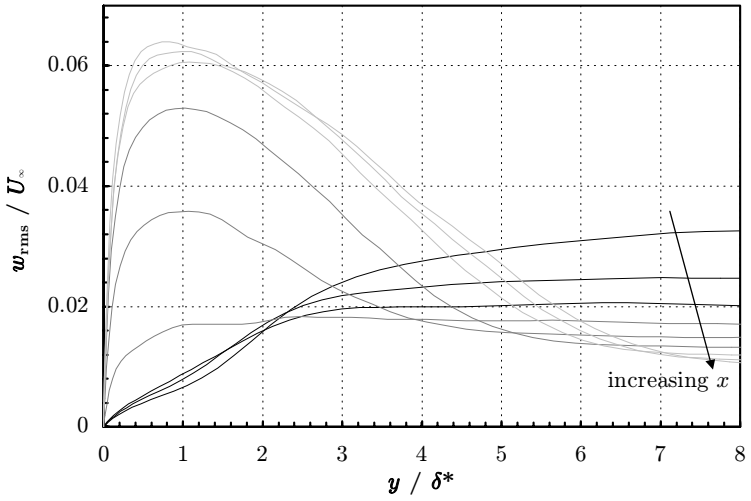

FIGURE 5.20: w_{rms} for the same downstream locations as in figure 5.18.

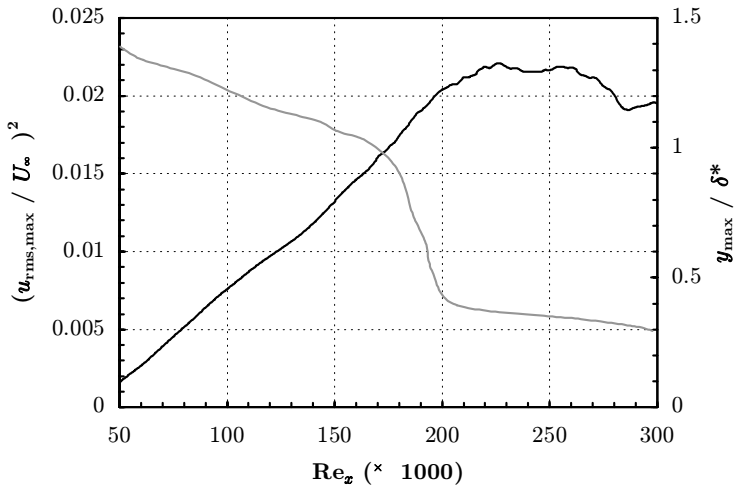

FIGURE 5.21: The normalized maximum streamwise velocity fluctuation $u^2_{\mathrm{rms,max}}$ and the respective position y_{max} within the boundary layer.

this plot are similar to those obtained by [19].

In figure 5.22 and 5.23, both the Reynolds-stress $\overline{uv}$ and the part of the energy production $-\overline{uv}\frac{\partial \overline{u}}{\partial y}$ are portrayed. Again, a close agreement between the numerical simulation [16] could be ascertained.

The comparison of different simulations and experiments with transition due to freestream turbulence shows that all of them measured a strong increase in the streamwise fluctuation u_{rms} before the turbulent breakdown [16]. However, even for cases with similar turbulence intensity, the growth rate and the peak value of u_{rms} for the onset of transition varies. This may indicate, that the freestream turbulence intensity alone is not sufficient to predict the features of transition

[28]. Since the freestream in the present simulation is highly isotropic, the only factor to influence the transition mechanism besides the turbulence intensity is given by the shape of the imposed spectrum $E(\kappa)$ and its integral length scale L_I. Especially the direct comparison of the decay of Tu between the test case T3A and the present simulation (and also the simulation [16] which showed a similar decay rate) given in figure 5.8 show a considerable discrepancy, mainly due to a different integral length scale of the turbulence. It may therefore be important to include an extensive characterization of the freestream spectrum in order to allow a direct comparison between different simulations and experiments.

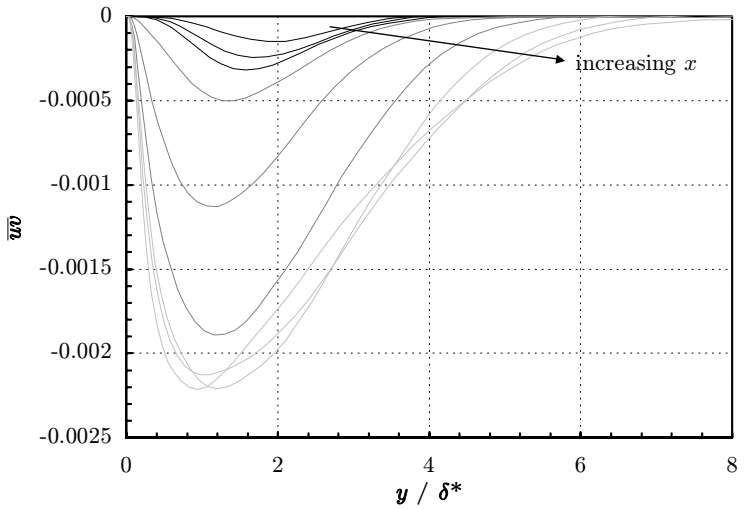

FIGURE 5.22: Reynolds-stress uv for the same downstream locations as in figure 5.18.

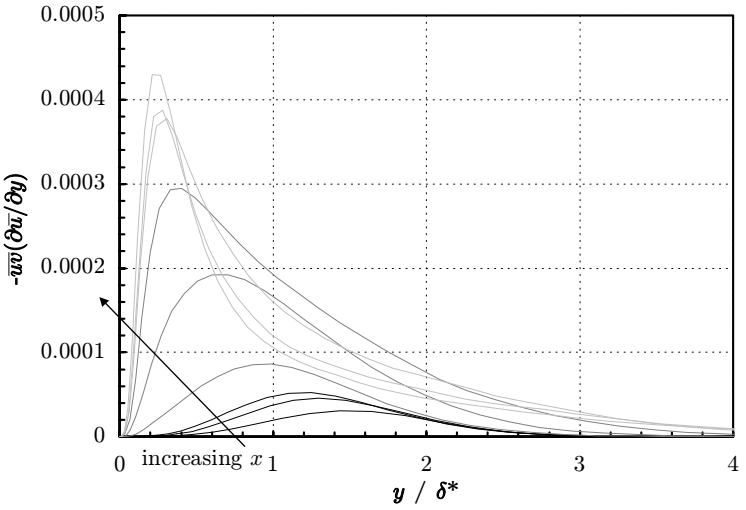

FIGURE 5.23: Energy production $-\overline{uv}\frac{\partial \overline{u}}{\partial y}$ for the same downstream locations as in figure 5.18.

Spanwise Scales

The spanwise spacing of the streaks can be computed using the spanwise correlation R_{uu} of the streamwise velocity component defined as

$$R_{uu}(\underline{x}, \underline{r}) = \frac{\overline{u(\underline{x})u(\underline{x}+\underline{r})}}{\sqrt{\overline{u^2(\underline{x})}\ \overline{u^2(\underline{x}+\underline{r})}}}. \tag{5.5}$$

with the displacement vector $\underline{r}$ aligned to the coordinate vector in z direction.

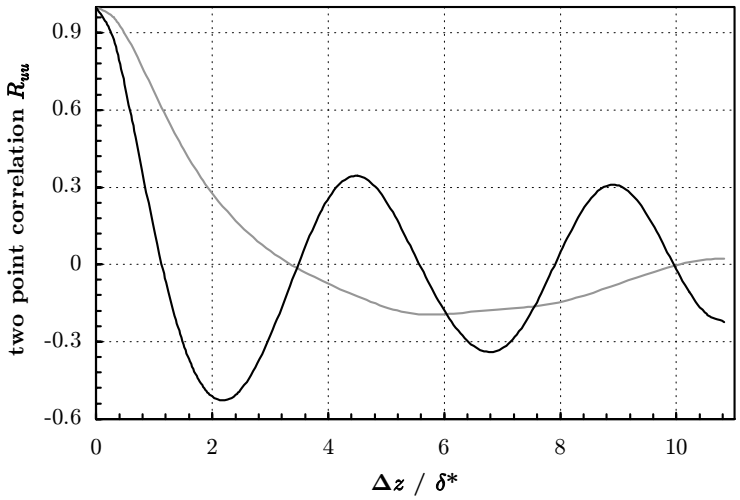

FIGURE 5.24: Spanwise two-point correlation R_{uu} of the streamwise velocity u at $x = 400$, Δz normalized by the local displacement thickness. Correlation in the boundary layer at $y = 1.4\delta^*$ (black) and in the freestream $y = 10\delta^*$ (grey).

The two-point correlation and an exemplary visualization of the velocity distribution in a y/z-plane are shown in figure 5.24 and 5.25, respectively. Plot 5.24 shows a large difference between R_{uu} in the freestream and in the boundary layer due to the appearance of the streaks. Qualitatively, a fair agreement for the streak spacing based on twice the maximum anti-correlation to other investigations has been found.

Figure 5.25 portrays another important issue of the boundary layer streaks. Due to the lift-up effect, low-speed streaks are expected to be located within the upper portion of the boundary layer, whereas high-speed streaks have their velocity maximum at a lower wall-normal distance [15]. Although figure 5.25 is only an instantaneous picture of the flow, the tendency can yet be seen.

5.4.2 Spots

As seen in figure 5.18, the streaks can reach a considerable strength of roughly 15% (averaged) of the freestream velocity before breakdown. However, with a certain strength the streaks become unstable and break down into a small localized area with chaotic fluid motion. This is called a turbulent spot within an otherwise

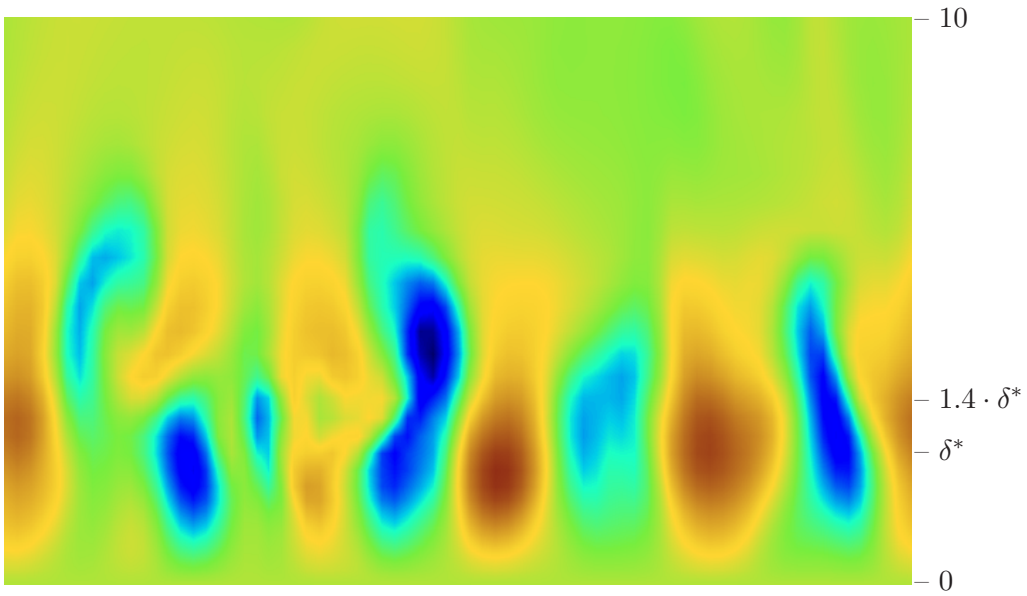

FIGURE 5.25: Visualization of the velocity distribution in a y/z-plane at $x = 400$, $z = -25..25$, $y = 0..10$. Dark (blue) areas indicate lower and light (red) areas higher speed than the mean flow in every y-position. The displacement thickness is $\delta^* = 2.31$.

laminar environment. Once a turbulent spot has originated, it will grow in all directions as it moves downstream. The spot merges with other spots to eventually form a persistent, fully developed turbulent boundary layer.

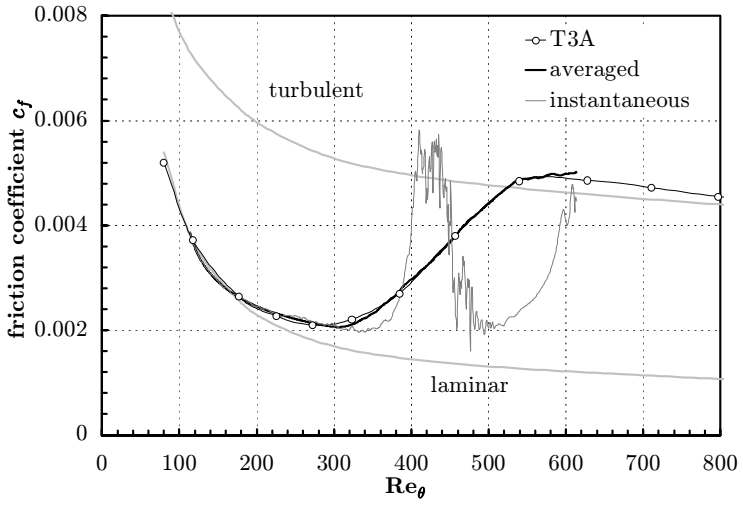

FIGURE 5.26: Instantaneous variation of the skin friction coefficient c_f through a turbulent region. For reference, the averaged results are shown as well (see figure 5.11).

The averaged results presented in section 5.3 show a smooth change from laminar to turbulent flow with increasing streamwise coordinate (see for example figure

5.11). However, the breakdown of a streak into a turbulent spot has locally great impact on the flow quantities. Figure 5.26 shows exemplary the variation of the skin friction c_f through a turbulent spot in an otherwise laminar environment (refer to visualization 5.27). In the region before and after the spot, where only streaks are present, the skin friction is only increased by a few percent above the laminar value. As soon as the turbulent spot is present, c_f instantaneously jumps to the turbulent level.

Figures 5.27-5.29 show each a time sequence of laminar streaks breaking down and forming a turbulent spot. Both figure 5.27 and 5.28 are visualizations of the flow field at a fixed y location. Therefore, near the inflow (left) there is still a portion of the freestream visible before the displayed plane penetrates the boundary layer. Within the boundary layer, the streaks are clearly visible in figure 5.27 as elongated structures with alternating dark and light color. Since streaks mainly influence the streamwise velocity component u, they are not visible in figure 5.28 displaying the normal velocity v. On the other hand, the spot formation and development is visible in both the u and v velocity (and also in the w component not shown) since turbulence is always a three-dimensional process.

Basically, three independent formations of spots are visible in this sequence, two spots right after each other in the middle the x/z-plane and a spot forming further upstream near the lower edge. They are indicated in figure 5.30 by the labels spot 1 to 3. But as these three spots reach the already turbulent region, they seem to have already merged with each other.

The growth process of the spots can be expressed by the velocity difference of the leading and trailing edge; measurements in velocity profiles similar to figure 5.28 yield a speed of 52% and 92% of the freestream velocity U_∞, respectively. Similarly, the spanwise widening speed is around 5% of the freestream velocity for the main portion of the spot.

Figure 5.29 presents the streamwise velocity distribution in a vertical x/y plane. The respective z coordinate is chosen to cut through spots 1 and 2 in figures 5.27 and 5.28.

5.4.3 Secondary Instability?

The exact way how streaks finally break down into turbulent spots and eventually into fully developed turbulence is still quite uncertain – of special interest is the question whether or not the streaks undergo a secondary oscillatory instability before their collapse. Whereas according to [16] no obvious secondary instability occurred, experimental studies (for example [19]) report the presence of a pre-breakdown instability (wiggle). A complete theory of streak instability by looking at ideal optimal streaks was developed by [3], showing that mainly two classes of instabilities are likely to occur: Sinuous instabilities forcing the streak to oscillate in a x/z-plane and the varicose instability with streaks oscillating in a x/y-plane. Although it was shown in [4] that for a single streak the sinuous instability is more likely to occur, no conclusive prediction can be made for the physical case with many streaks interacting with each other.

The data collected with the present direct numerical simulation have not yet

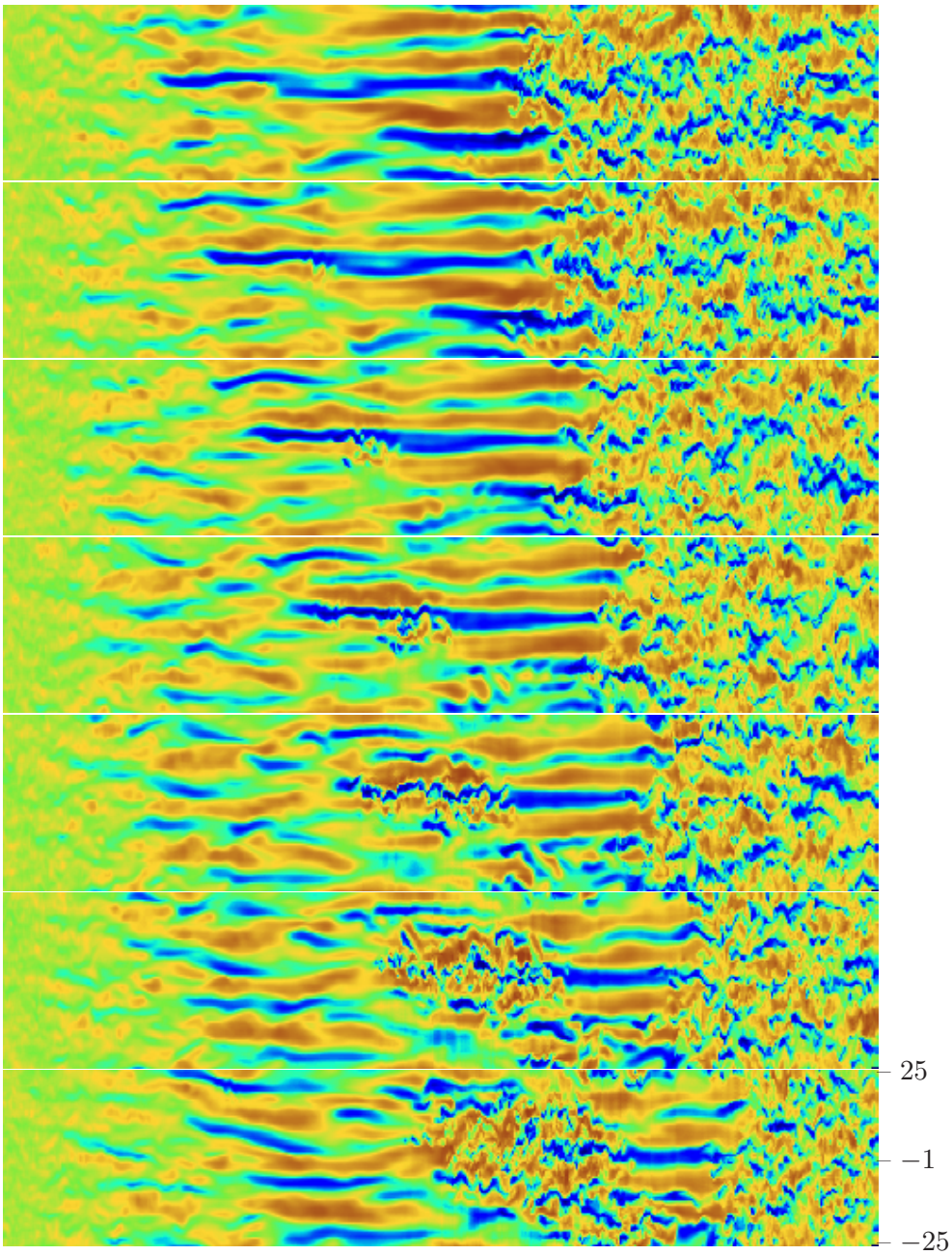

FIGURE 5.27: Visualization of streaks and a spot formation showing the amplitude of the streamwise velocity u. $x = 0..900$ (without fringe region), $z = -25..25$, $y = 2.5$. Dark (blue) areas indicate lower and light (red) areas higher speed. The velocity ranges from -30% to $+30\%$ of the global mean velocity. The difference between two frames is 75 time units starting at $t = 145$.

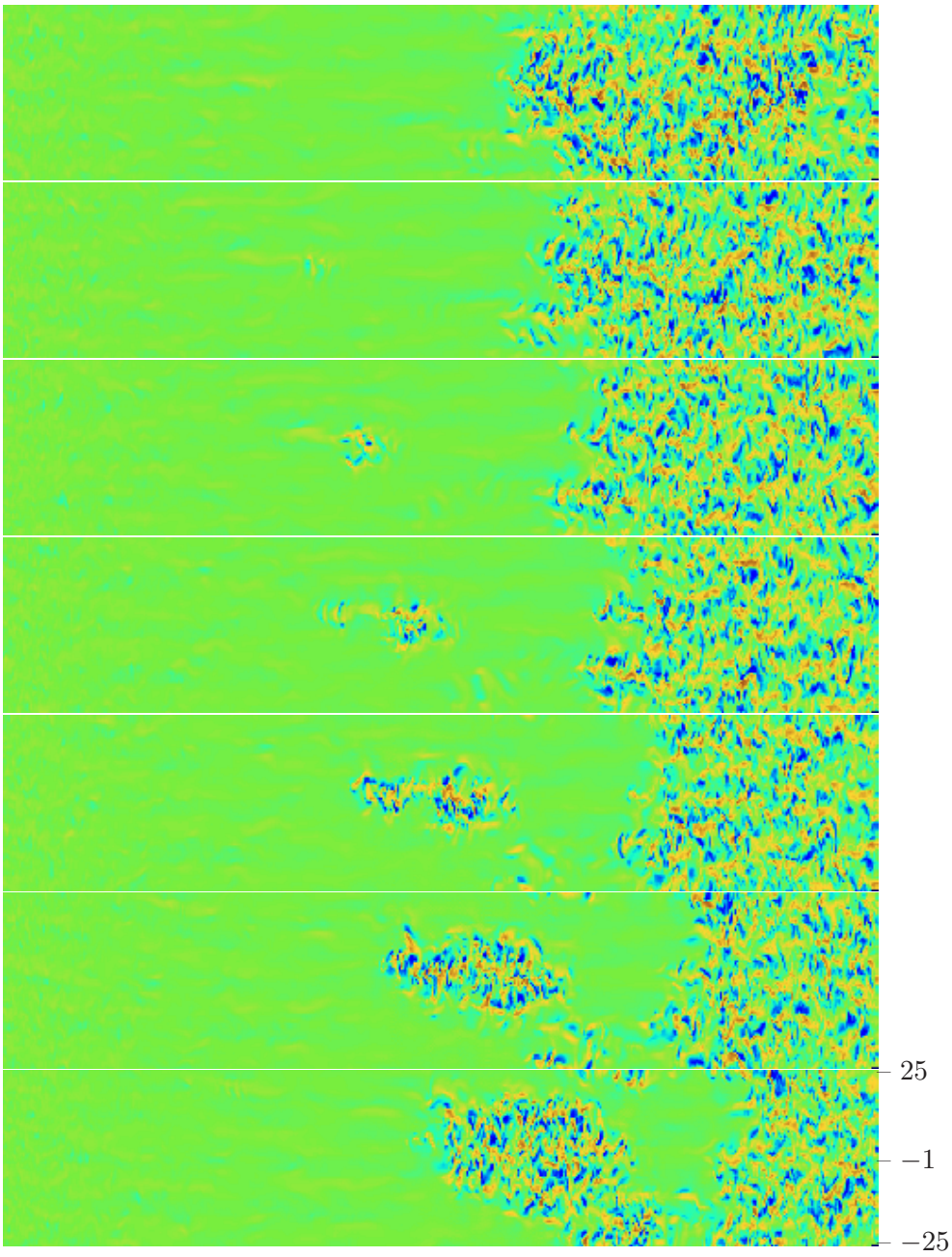

FIGURE 5.28: Visualization of a spot formation showing the amplitude of the normal velocity v with the same parameters as figure 5.27. Dark (blue) areas indicate lower and light (red) areas higher speed, whereas grey (green) indicates zero velocity. The velocity ranges from -30% to 30% of the freestream velocity.

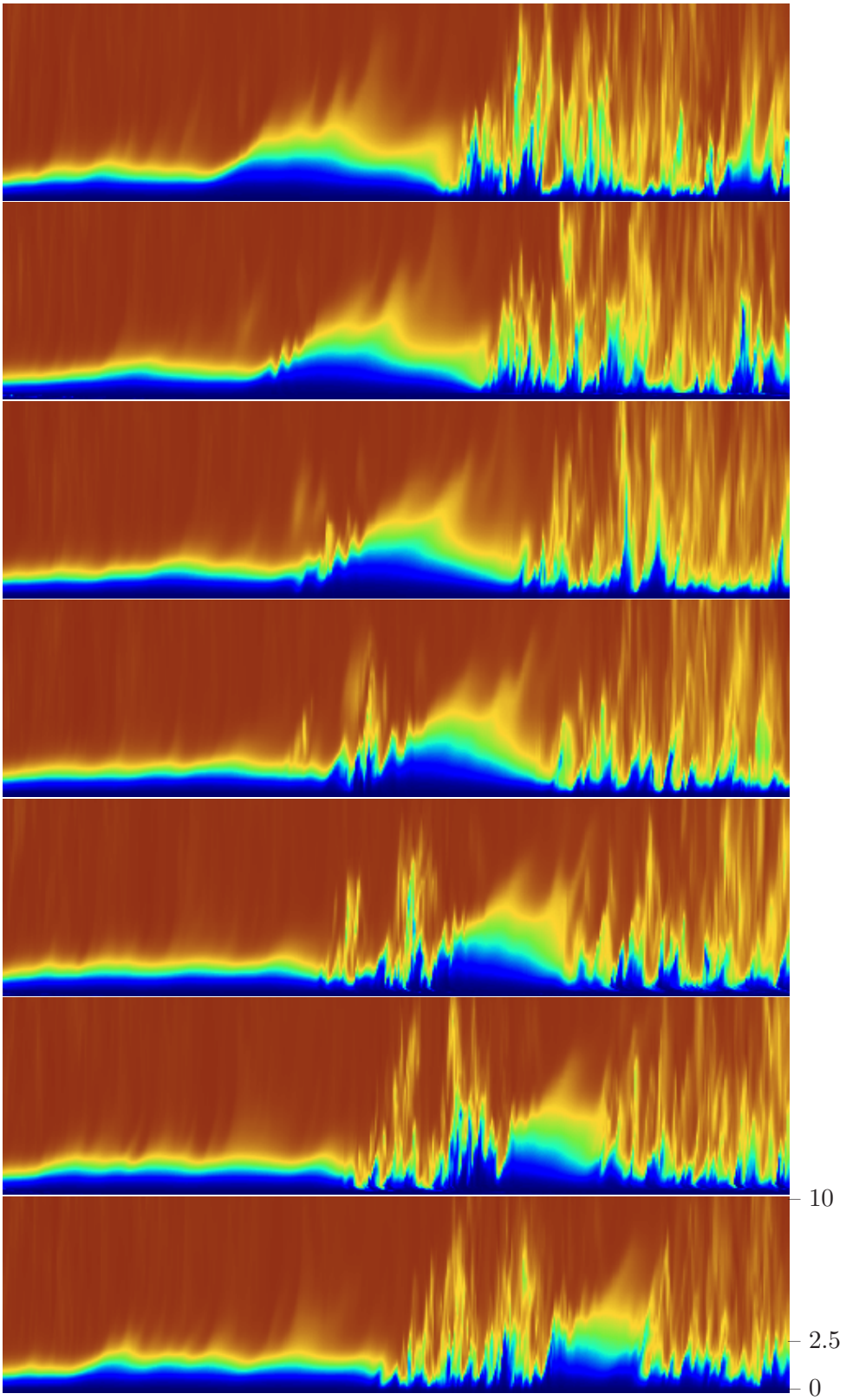

FIGURE 5.29: Visualization of a spot formation showing the amplitude of the streamwise velocity u in a vertical plane. $x = 0..900$ (without fringe region), $y = 0..10$, $z = -1$, the time is the same as in figure 5.27. Dark (blue) areas indicate low and light (red) areas high speed. The velocity ranges from zero to the freestream velocity U_∞.

been evaluated to allow a final decision on the question of the exact characterization of the turbulent breakdown. Nevertheless, the three spots shown in the velocity profiles 5.27, 5.28 and 5.29 have been looked at more closely. However, no direct determination of the energy growth during the breakdown has been performed. Calculations like this could eventually allow an exact characterization of a secondary instability. Furthermore, it must be noticed that only the three spots in the above figure were examined, therefore no statistical information over the whole amount of spots is available yet.

Figure 5.30 shows an enlarged view following the spot formation, depicting the streamwise velocity component u. For comparison, figures 5.31, 5.32 and 5.33 show some of the interesting plots of the other velocity components.

The spot formations can be followed by comparing the respective pictures in figure 5.30, 5.31 and 5.32. For all of the three spots, the formation sequence seems to be similar: At the same time as the low-speed streak begins to show regular oscillations in the x/z-plane, the velocity component w shows regularly distributed alternating high and low-speed 'points'. v seems to indicate a velocity distribution similar to a horseshoe cut at different heights. The oscillations of the streak in u and in v are likely to be symmetric with respect to the streamwise direction, whereas the oscillation in w is asymmetric. This would indicate, that the basic instability mode is that from a varicose instability, forcing a streak to wiggle up and down in a x/y-plane. The visualization in such a plane (given in figure 5.33) seems to support this statement, although calculations of [4] showed that for an isolated streak the sinuous instability is more likely to occur.

Some other important observation can be made looking at these visualizations. It has to be mentioned again, that these are only preliminary results, which must undergo further checking. From looking at the formation of the first spot in figure 5.30, it seems that the instability originates because of the encounter of two low-speed streaks, slightly displaced in z. Hereby, strong velocity gradients are generated, which could eventually lead to a breakdown.

A second important issue is that, although all three spots visible in the above figures seem to have the same characterization in all velocity components, their transition speed is completely different. The breakdown of the first spot is completed within 100 time units, whereas the third spot seems to need around 250 time steps. This could indicate, that different breakdown mechanism are present in a flow at the same time.

Further post-processing of the present data will hopefully lead to more conclusive statements concerning the breakdown of the streaks.

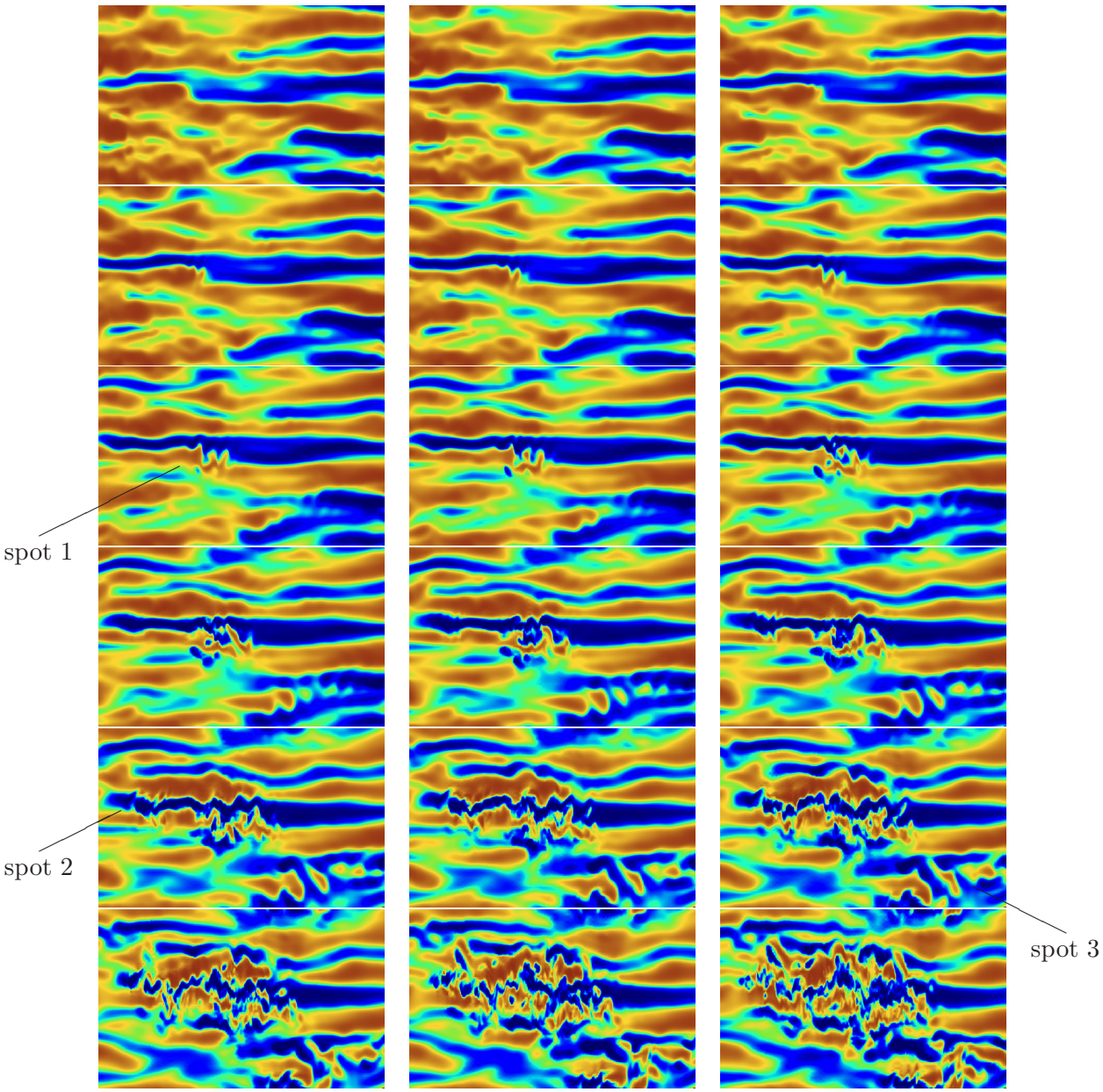

FIGURE 5.30: Enlarged visualization of spot formation depicting the amplitude of the streamwise velocity u (x/z-plane). Length in x direction 300 with panorating speed of $0.51 \cdot U_\infty$, $z = -25..25$, $y = 2.5$. Dark (blue) areas indicate lower and light (red) areas higher speed. The velocity ranges from -30% to $+30\%$ of the global mean velocity. The difference between two frames is 25 time units, starting at $t = 100$ compared to figure 5.27.

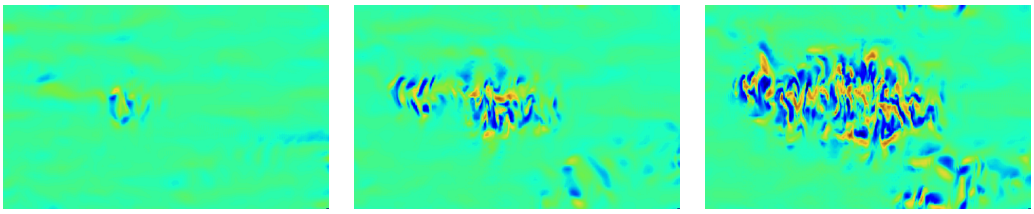

FIGURE 5.31: Enlarged visualization of spot formation depicting the amplitude of the normal velocity v for t=250, 400, 500, other parameters see figure 5.30.

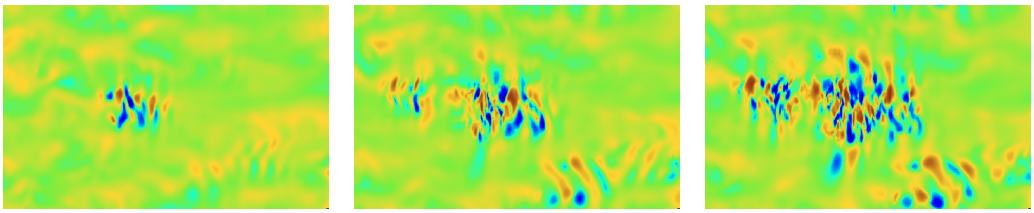

FIGURE 5.32: Enlarged visualization of spot formation depicting the amplitude of the spanwise velocity w for t=270, 375, 425, other parameters see figure 5.30.

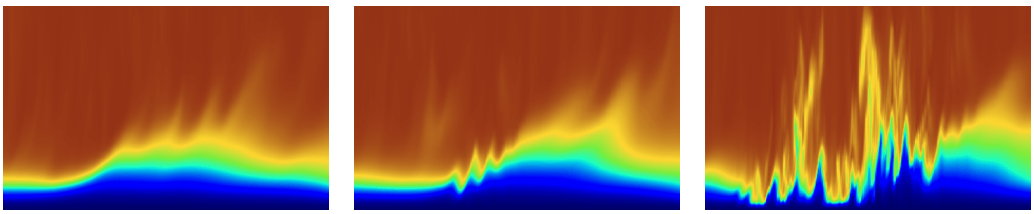

FIGURE 5.33: Enlarged visualization of spot formation depicting the amplitude of the normal velocity u for t=100, 250, 500 (x/y-plane). Panorating speed and extent in x similar to figure 5.30, $y = 0..10$, $z = -1$.

Chapter 6

Conclusions

6.1 Present Results

The DNS-code presented in this theses provides a robust method to perform simulations of transitional flat plate boundary layers subject to freestream turbulence. The code has been thoroughly tested and validated. The basic idea of superposing Orr-Sommerfeld and Squire modes from [12] and [16] was combined with a highly effective numerical code using Fourier and Chebyshev decomposition in all directions. The spectral composition of the imposed freestream turbulence is automatically computed to meet any given inlet spectrum, thereby providing a means to study the effect of different turbulence intensities, integral length scales and even shapes of spectra.

The results obtained by the present algorithm allow the conclusion that the main effects occurring in freestream turbulence and in a transitional boundary layer are well captured – the decay rate of the freestream turbulence matches the know decay law, the growth of streaky structures in the boundary layer could be observed and their characteristics compare well to experimental findings. Moreover, the averaged statistics like skin friction, u^+ and u_{rms} obtained from the simulation show qualitatively and quantitatively good agreement to experiments and other numerical simulations.

However, due to the tight schedule it was not yet possible to do a complete post-processing of the data generated by the simulation. Especially the interesting question of how exactly the laminar streaks break down into turbulent spots has not yet been conclusively answered, although it seems, that there are signs of regular instabilities before the turbulent breakdown.

6.2 Future Work

The present study was mainly thought of setting up a suitable numerical code to perform studies of transitional boundary layers. The code can therefore be used to help to find answers to some questions, which are even today quite uncertain.

- It was realized during the course of this work, that not only the turbulence intensity of the freestream turbulence is important to predict transition. On

the contrary, an exact characterization of the imposed freestream turbulence and their integral length scales are needed. Especially experimental studies often lack that information. The above algorithm could be used to perform systematic studies of the influence of types of freestream turbulence on the boundary layer.

- The prediction of the onset of transition in physical situations subject to freestream turbulence is still quite difficult. Although some methods exist (e.g. e^N-method [2]) their accuracy is not very good. Therefore, more accurate modeling of the transitional mechanism in the boundary layer must be devised together with identifying the important parameters. The present code could help as a way to validate the different models.

- Closely related to possible modeling of the transition onset, a better understanding of the exact way how laminar streaks break down into turbulence is indicated. The results of different experimental and numerical studies differ in the question, whether or not a distinct secondary instability with exponential energy growth does exist. Moreover, a characterization of such a instability (varicose, sinuous etc.) is still part of extensive research. The present simulation could play an important role thereby, since the physical situation of many streaks interacting with each other is simulated and not only the idealized behaviour of an isolated streak.

On the other hand, improvements in the code and its efficiency could be an important issue; in the present study, the number of eigenmodes of the continuous spectrum used to construct the freestream turbulence was fixed to a value of 200. It would be interesting to study the effect on the turbulence characteristics when using different numbers of eigenmodes.

Acknowledgement

This report is a Diploma Thesis for the masters degree of mechanical engineering at the Federal Institute of Technology in Zurich (Eidgenössische Technische Hochschule ETHZ). It was conducted at the Royal Institute of Technology in Stockholm (Kungliga Tekniska Högskolan KTH) via the ERASMUS student exchange programme.

My first thank goes to Prof. Dan Henningson at the Department of Mechanics, KTH Stockholm, for giving me the chance to stay in Sweden and providing me with all the support and equipment necessary for this thesis. When I first came to Sweden four months ago, I have barely heard the term Orr-Sommerfeld equation or Squire mode, it was therefore wonderful opportunity for me to be introduced into the very interesting and important topic of boundary layer instability; and being right at the source for this research.

I also want to thank PD Dr. Carlos Härtel and Prof. Leonhard Kleiser at the Institute of Fluid Mechanics, ETH Zürich, for helping me to get in contact with KTH and making it possible to write the diploma thesis abroad.

M.Sc. Luca Brandt at the Department of Mechanics, KTH, helped me very much with discussions, computers, implementing the continuous modes into the code and with choosing right parameters to finally get some turbulent spots. I really enjoyed that he always had time for my questions and to discuss problems and results. Furthermore I want to thank all the people from the Department of Mechanics in Stockholm for their hospitality.

And, last but not least, Mikaela, vielen Dank für alles!

Philipp Schlatter
Lidingö, March 17th 2001

Bibliography

[1] Alfredsson, P.H. & Matsubara, M.: *Free-stream Turbulence, Streaky Structures and Transition in Boundary Layer Flows*, AIAA 2000-2534 Fluids 2000, American Institute of Aeronautics and Astronautics (2000)

[2] Andersson, P.: *Modelling of Boundary Layer Stability*, Ph.D. Thesis, KTH Stockholm (1999)

[3] Andersson, P., Berggren, M. & Henningson, D.S.: *Optimal disturbances and bypass transition in boundary layers*, Phys. Fluids, vol.11, pp.134-150 (1999)

[4] Andersson, P., Brandt, L., Bottaro, A. & Henningson, D.S.: *On the breakdown of boundary layer streaks*, J.Fluid Mech., vol.428, pp.29-60 (2001)

[5] Berlin, S.: *Oblique Waves in Boundary Layer Transition*, Ph.D. Thesis, KTH Stockholm (1998)

[6] Berlin, S. & Henningson, D.S.: *A nonlinear mechanism for receptivity of freestream disturbances*, Phys. Fluid, vol.11, pp.3747-3760 (1999)

[7] Brandt, L., Henningson, D.S. & Ponziani, D.: *Weakly non-linear analysis of boundary layer receptivity to free-stream disturbances*, submitted to Phys. Fluids (2001)

[8] Brigham, E.O.: *FFT: Fast Fourier Transform*, Oldenbourg Verlag, München, 5. Auflage (1992)

[9] Bronstein, I.N. & Semendjajew, K.A.: *Taschenbuch der Mathematik*, Verlag Harry Deutsch, Frankfurt am Main, 2. Auflage (1995)

[10] Coupland, J.: *Flat Plate Transitional Boundary Layers*, Rolls-Royce Experimental Data (1992), ERCOFTAC, available from http://www.ercoftac.org.

[11] Gottwald, S. et al.: *Meyers Kleine Enzyklopädie Mathematik*, Meyers Lexikonverlag, Mannheim/Leipzig/Wien/Zürich, 14. Auflage (1995)

[12] Grosch, C.E. & Salwen, H.: *The continuous spectrum of the Orr-Sommerfeld equation. Part 1. The spectrum and the eigenfunctions*, J.Fluid Mech., vol.87, part 1, pp.33-54 (1978)

[13] Grosch, C.E. & Salwen, H.: *The continuous spectrum of the Orr-Sommerfeld equation. Part 2. Eigenfunction expansions*, J.Fluid Mech., vol.104, pp.445-465 (1981)

[14] Schmid, P.J. & Henningson, D.S.: *Stability and Transition in Shear Flows*, Springer (2001)

[15] Jacobs, R.G. & Durbin, P.A.: *Bypass transition phenomena studied by computer simulation*, Ph.D. Thesis, Stanford University, Report No. TF-77 (2000)

[16] Jacobs, R.G. & Durbin, P.A.: *Simulations of bypass transition*, J.Fluid Mech., vol. 428, pp.185-212 (2001)

[17] Landahl, M.T.: *Wave breakdown and turbulence*, SIAM Journal on Applied Mathematics, vol.28/735 (1975)

[18] Lundbladh, A., Berlin, S., Skote, M., Hildings, C., Choi, J., Kim, J. & Henningson, D.S.: *An Efficient Spectral Method for Simulation of Incompressible Flow over a Flat Plate*, Technical Report, KTH Stockholm (1999)

[19] Matsubara, M. & Alfredsson, P.H.: *Disturbance growth in boundary layers subjected to free stream turbulence*, accepted for publication in J. Fluid Mech. (2001)

[20] Pironneau, O. et al.: *Numerical Simulation of Unsteady Flows and Transition to Turbulence*, ERCOFTAC, Cambridge University Press (1992)

[21] Reddy, S.C. & Henningson, D.S.: *Energy growth in viscous channel flows*, J.Fluid Mech., vol. 252, pp.209-238 (1993)

[22] Roach, P.E. & Brierley, D.H.: *The influence of a turbulent free-stream on zero pressure gradient transitional boundary layer development. Part I: Test cases T3A and T3B*, in *Numerical Simulation of Unsteady Flows and Transition to Turbulence*, pp.319-347, ERCOFTAC, Cambridge University Press (1992)

[23] Rotta, J.C.: *Turbulente Strömungen*, B.G. Teubner, Stuttgart (1972)

[24] Schlichting, H.: *Grenzschicht-Theorie*, Verlag G. Braun, Karlsruhe, 8. Auflage (1982)

[25] Skote, M.: *Studies of turbulent boundary layer flow through direct numerical simulation*, Ph.D. Thesis, KTH Stockholm (2001)

[26] Spurk, J.H.: *Strömungslehre*, Springer Verlag, Berlin, 4. Auflage (1996)

[27] Tennekes, H. & Lumley, J.L.: *A First Course in Turbulence*, The MIT Press, Cambridge MA (1972)

[28] Westin, J.: *Laminar-Turbulent Boundary Layer Transition Influenced by Free Stream Turbulence*, Ph.D. Thesis, KTH Stockholm (1997)

Appendix A

Boundary Layers

A.1 Boundary Layer Equations

Consider a steady flow along a fixed wall. Such a flow is governed by the basic two-dimensional Navier Stokes equations (see chapter 2). Several order of magnitude estimates can be used to develop an approximate set of equations valid near the wall. Without going into the details of this derivation (for elaborate description see e.g. [24]), the boundary layer equations first derived by Prandtl 1904 read in non-dimensional form

$$u\frac{\partial u}{\partial x} + v\frac{\partial u}{\partial y} = -\frac{\partial p}{\partial x} + \frac{1}{\mathrm{Re}}\frac{\partial^2 u}{\partial y^2} \tag{A.1}$$

$$0 = \frac{\partial p}{\partial y} \tag{A.2}$$

$$\frac{\partial u}{\partial x} + \frac{\partial v}{\partial y} = 0. \tag{A.3}$$

The definition of the Reynolds number Re and the nondimensional variables is the same as in chapter 2. As an important result we notice that the pressure p is only a function of x and will thus not change over the vertical extent of the boundary layer.

A.2 Blasius Solution

In some cases it is possible to find relatively simple solutions for the boundary layer equations (A.1)-(A.3). Consider the case of a two-dimensional parallel flow over a flat plate with no pressure gradient. The velocity far from the plate is independent of x and y – it simply reads U_∞ in x direction. The solution to this basic boundary layer problem was presented first by Blasius (1906) (see e.g. [26] p.363).[1] Following his approach one introduces the similarity variable η and the

[1] Besides the Blasius boundary layer, other basic solutions to the boundary layer equations can be found for flows varying exponentially in U_∞ over x with base flow orthogonal (Falkner-Skan flows) or non-orthogonal to the leading edge (swept wedge, Falkner-Skan-Cooke flow).

stream function ψ ($u = \frac{\partial \psi}{\partial y}$, $v = -\frac{\partial \psi}{\partial x}$)

$$\eta = y\sqrt{\frac{U_\infty}{\nu x}} \tag{A.4}$$

$$\psi = \sqrt{\nu U_\infty x} f(\eta). \tag{A.5}$$

Combining these relations with the boundary layer equations yields a (ordinary) differential equation for $f(\eta)$. Together with boundary conditions for f it reads

$$2f'''(\eta) + f(\eta)f''(\eta) = 0 \tag{A.6}$$

$$f(0) = f'(0) = 0 \tag{A.7}$$

$$f'(\infty) = 1. \tag{A.8}$$

Solving this initial value problem by numerical integration, the function $f(\eta)$ and

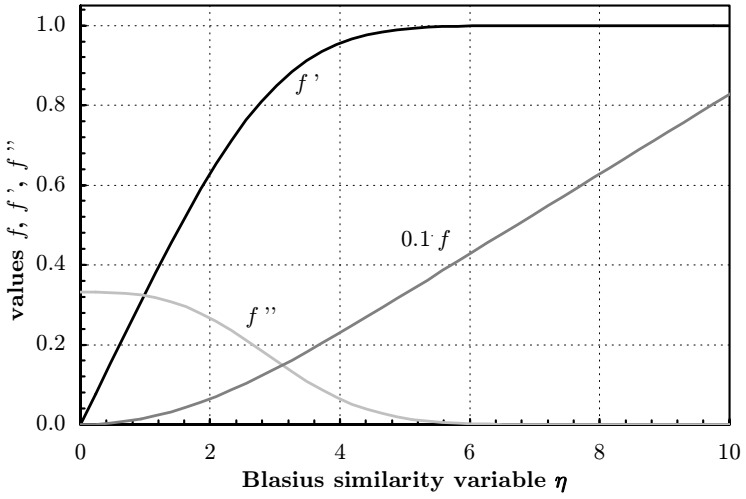

FIGURE A.1: Function f used for computation of the Blasius solution of the boundary layer equations

its derivatives can be evaluated as function of the similarity variable η, see figure A.1. Use of the constraints (A.4), (A.5) yields the velocity distribution over the boundary layer as

$$\frac{u}{U_\infty} = f'(\eta) \tag{A.9}$$

$$\frac{v}{U_\infty} = \frac{1}{2}\frac{y}{x}\left[f'(\eta) - \frac{1}{\eta}f(\eta)\right]. \tag{A.10}$$

It is worth mentioning that the velocity profile $u = u(\eta)$ is only dependent on the similarity variable η, whereas for $v = v(\eta, y/x)$ the relative position y/x is necessary to compensate the displacement effect of the growing boundary layer. Figure A.2 shows the typical behaviour of u and v throughout the boundary layer, figure A.3 shows the complete vector field (u, v).

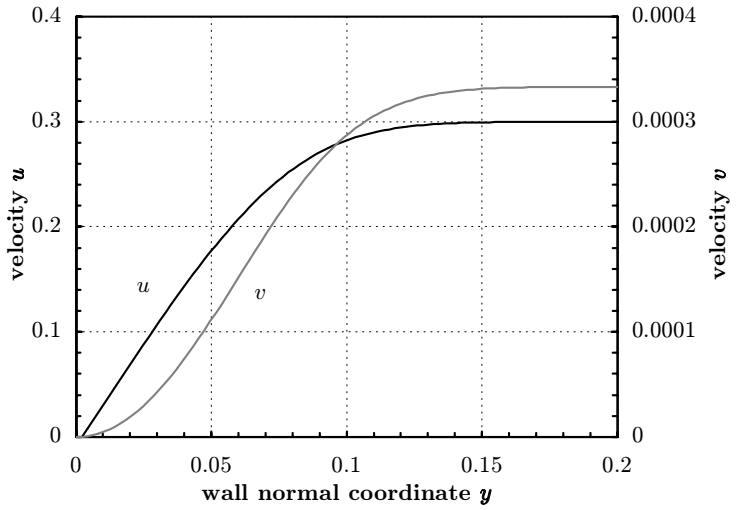

FIGURE A.2: Typical velocity distribution in a Blasius boundary layer with physical scaling. Parameters are $U_\infty = 0.3$, $\nu = 1 \cdot 10^{-5}$, $x = 20$ ($\eta = 38.7y$)

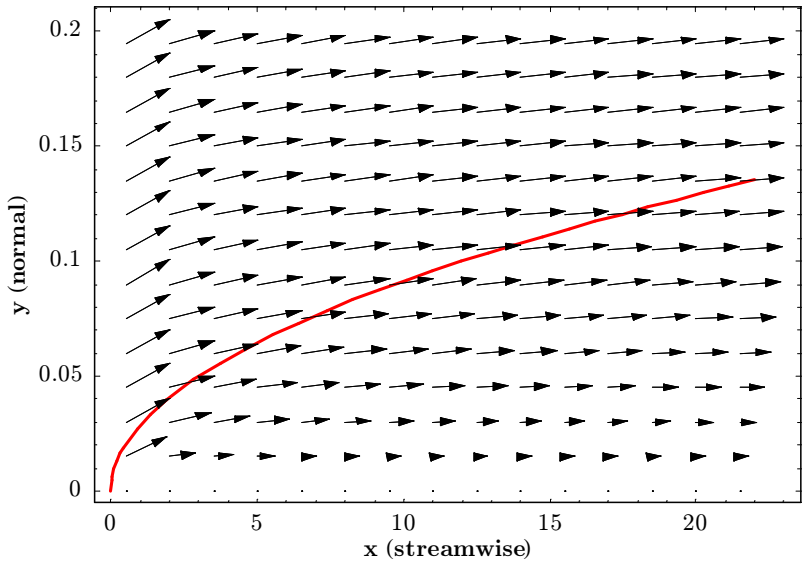

FIGURE A.3: Velocity profile of the 2-dimensional Blasius boundary layer with respect to the boundary layer thickness $\delta_{99\%}$ (physical units). Parameters are $U_\infty = 0.3$, $\nu = 1 \cdot 10^{-5}$

A.3 Integral Parameters

With a given velocity profile (u, v) in the boundary layer, several integral parameters of the boundary layer can be calculated.

For the description of the vertical extent of a boundary layer, various definitions of a boundary layer thickness are possible. A intuitive geometric definition is based on the shape of the velocity profile $u(y)$. The edge of the boundary layer is defined

as the vertical position where u is reaching 99% of the free stream velocity U_∞

$$u(y = \delta_{99\%}) = 0.99 U_\infty. \tag{A.11}$$

It is obvious that this definition of a boundary layer thickness cannot be very accurate. Therefore, a more unique definition can be calculated based on the displacement effect of the boundary layer (displacement thickness δ^*)

$$\delta^* = \int_0^\infty \left(1 - \frac{u}{U_\infty}\right) dy \tag{A.12}$$

Taking into account the loss of momentum in the boundary layer due to the skin friction one finds the momentum thickness θ

$$\theta = \int_0^\infty \left(1 - \frac{u}{U_\infty}\right) \frac{u}{U_\infty} dy. \tag{A.13}$$

The ratio of the displacement thickness and the momentum thickness is known as shape factor H

$$H = \frac{\delta^*}{\theta}. \tag{A.14}$$

Especially in technical applications, the (local) skin friction coefficient c_f is an important quantity. It is defined as

$$c_f = \frac{\tau_w}{\frac{\rho}{2} U_\infty^2} \qquad \text{with} \qquad \tau_w = \mu \frac{\partial u}{\partial y}\Big|_{y=0}, \tag{A.15}$$

with τ_w as the local shear force acting on the surface.

Table A.1 gives an overview of the above parameters for the laminar (Blasius) boundary layer and empirical formulas for fully developed turbulent boundary layer.

Property	Laminar Flow	Turbulent Flow
δ	$5.00 x \mathrm{Re}_x^{-1/2}$	$0.37 x \mathrm{Re}_x^{-1/5}$
δ^*	$1.721 x \mathrm{Re}_x^{-1/2}$	$0.046 x \mathrm{Re}_x^{-1/5}$
θ	$0.664 x \mathrm{Re}_x^{-1/2}$	$0.036 x \mathrm{Re}_x^{-1/5}$
H	2.59	1.28
c_f	$0.664 \mathrm{Re}_x^{-1/2}$	$0.0576 \mathrm{Re}_x^{-1/5}$

TABLE A.1: Integral parameters for fully developed laminar and turbulent flat-plate boundary layers.

Using the different boundary layer thicknesses, a set of different Reynolds numbers can be defined – all of them expressing the streamwise position

$$\mathrm{Re}_x = \frac{x U_\infty}{\nu} \qquad \mathrm{Re}_{\delta^*} = \frac{\delta^* U_\infty}{\nu} \qquad \mathrm{Re}_\theta = \frac{\theta U_\infty}{\nu} \tag{A.16}$$

with x as physical distance from the leading edge, U_∞ and ν as the freestream velocity and viscosity, respectively.

A.4 Wall-Scaling

Especially for turbulent boundary layers, the friction velocity can be defined using the shear force τ_w (A.15) and the density ρ

$$u_\tau = \sqrt{\frac{\tau_w}{\rho}}. \tag{A.17}$$

With this definition, the so-called wall-scaling (+-units) can be introduced for the mean velocity $\overline{u}$ and the wall-normal distance y

$$u^+ = \frac{\overline{u}}{u_\tau} \qquad y^+ = y\frac{u_\tau}{\nu}. \tag{A.18}$$

It is known, that a typical velocity profile for a turbulent boundary layer can be

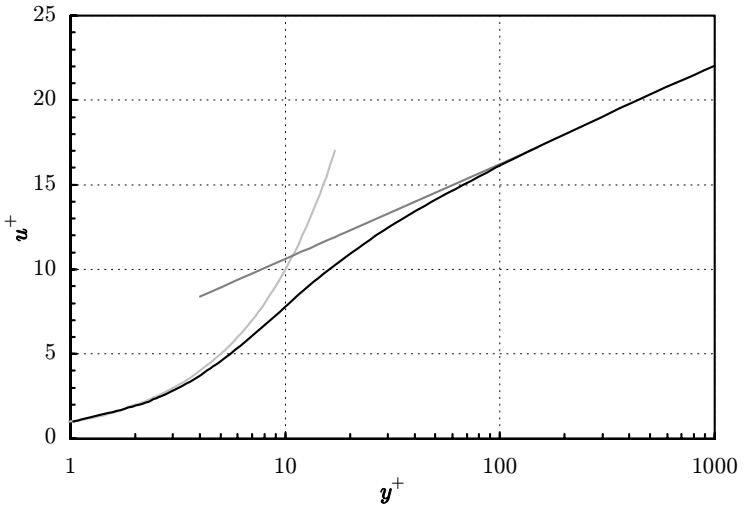

FIGURE A.4: Typical velocity profile for a turbulent boundary layer showing the viscous sublayer (A.19), the logarithmic layer (A.20) and the approximate function according to Spalding (A.21).

divided into different sublayers [27]. The viscous sublayer extends to about $y^+ < 7$ and the velocity is given by

$$u^+ = y^+. \tag{A.19}$$

The logarithmic layer typically lies between $y^+ = 30$ and $y = 0.1\delta_{99\%}$ and is governed by

$$u^+ = \frac{1}{\kappa}\ln y^+ + C \tag{A.20}$$

with $\kappa \approx 0.41$ as the von Kármán constant and $C \approx 5.0$ for a smooth wall. Above the logarithmic layer follows the defect layer whose structure makes a noticeable departure from logarithmic behaviour approaching the freestream.

An approximate function to describe the velocity throughout the viscous sublayer and the logarithmic layer is given by Spalding

$$y^+ = u^+ + \frac{1}{E}\left[e^{\kappa u^+} - 1 - \frac{1}{2}(\kappa u^+) - \frac{1}{6}(\kappa u^+)^2 - \frac{1}{24}(\kappa u^+)^3\right] \tag{A.21}$$

with $\kappa \approx 0.41$ as the von Kármán constant and $E \approx 8.6$.